Materials Science

Bulletin of Materials Science

Volume 21, No. 2, April 1998

CONTENTS

Cover: Typical LEED pattern of clean Si (7×7) reconstructed surface, obtained at 50 eV incident beam energy. For details, see p. 114.

Research Articles

Crystalline alumina films prepared by nebulized spray pyrolysis

P MURUGAVEL, BENEDICT ITA[†] and A R RAJU*

Chemistry and Physics of Materials Unit, Jawaharlal Nehru Centre for Advanced Scientific Research, Bangalore 560 064, India
[†] Chemistry Department, University of Calabar, Calabar, Nigeria

Abstract. Crystalline alumina films have been successfully deposited on Si(100) and amorphous silica substrates by the nebulized spray pyrolysis technique. The surface morphology of the films has been studied by various microscopic techniques. The films exhibit satisfactory microhardness and frequency independent capacitance.

Keywords. Crystalline alumina; nebulized spray pyrolysis; SEM; AFM; microhardness.

1. Introduction

Alumina films are of considerable interest because of their potential applications for wear resistant coatings and optical coatings. Amorphous alumina thin films have been prepared on glass as well as Si(100) by chemical vapour deposition from aluminum acetylacetonate (Maruyama and Arai 1992). Metal organic chemical vapour deposition by using precursors such as aluminium *tris*-dipivaloylmethanate (Kim *et al* 1993; Ciliberto *et al* 1995), also yields amorphous films on silicon and glass substrates. Single crystalline gamma alumina films have been grown on silicon substrates by metalorganic molecular beam epitaxy using aluminum alkoxide (Iizuka *et al* 1992), while heteroepitaxial gamma alumina films are obtained with trimethyl aluminum (Ishida *et al* 1988). CVD of alumina on silicon substrates by using aluminum trichloride gives films of κ-Al_2O_3 which transforms to α-Al_2O_3 on being heated to higher temperatures of 1200–1350 K (Fredriksson and Carlsson 1993). By ion–beam-induced chemical vapour deposition, trimethyl aluminum gives crystalline α-Al_2O_3 films at 1273 K (Caballero *et al* 1996). We were interested in exploring whether crystalline alumina films could be obtained by employing the simple technique of nebulized spray pyrolysis.

2. Experimental

The technique of nebulized spray pyrolysis for depositing thin films by employing a home built apparatus has been described elsewhere (Raju *et al* 1995; Aiyer *et al* 1997). The apparatus consists of two zones: (i) the atomization chamber and (ii) the pyrolysis reactor. The source liquid is kept in the atomization chamber which is attached with a PZT transducer at the bottom which oscillates at a frequency of 1·72 MHz. Aluminium acetylacetonate in a methanol solvent (0·05 M) was employed for all the depositions. When a high-frequency ultrasonic beam is directed at the liquid/gas interface, a geyser forms at the surface of the liquid and the height of the geyser is proportional to the acoustic intensity and the physical properties of the liquid (vapour pressure, viscosity and surface tension). When the amplitude of the acoustic vibrations exceeds a certain threshold value, atomization of the liquid occurs. Above this threshold, a continuous and regular mist is generated. The mist is carried by the carrier gas (dry air in the present case) to the pyrolysis reactor zone onto a pre-heated substrate leading to the mist decomposition and the film formation on the substrate. We have used single crystal Si(100) as well as polished amorphous silica as the substrates in the present study.

Alumina films were characterized by X-ray diffraction, scanning electron microscopy (SEM), electron diffraction, atomic force microscopy (AFM), capacitance measurements and dynamic hardness measurements. A Seifert 3000 X-ray powder diffractometer with Cu–Kα radiation (grazing incident geometry) was employed for X-ray diffraction studies. A Leica S440i SEM was used for microstructure studies. Nanoscope II fitted with AFM was used to study the surfaces of the films at high-resolution. Capacitance and tan δ were measured between 100 Hz and 10 MHz with HP4296 automatic impedance analyser. Shimadzu dynamic ultra micro-hardness instrument (DUH 200) was employed to study microhardness of the films. The method of measuring hardness using nano indentation involves making small indentation using Berkovich indentor, while continuously recording the indentation load, $P(gf)$ and

in accordance with the shape of the indentor (indentation factor).

3. Results and discussion

We have examined morphology of the Al_2O_3 films deposited at 673 K on Si(100) substrates by both SEM and AFM. We show the SEM image in figure 1a and a surface plot from AFM in figure 2a. The surface of the film is quite smooth, consisting of very small well-connected grains of less than 100 nm size, as seen from the AFM surface plot. The surface roughness measured from the AFM surface plot is around 5·75 nm. The thickness of Al_2O_3 film on the Si(100) substrate as obtained from the cross sectional SEM image shown in figure 1b is around 375 nm.

The SEM image of an alumina film deposited on amorphous silica at 673 K is shown in figure 3a. The high-resolution AFM surface plot, given in figure 2b shows the presence of smaller grains (< 50 nm). These grains are significantly smaller than those in case of Al_2O_3 films deposited on Si(100) substrates. The surface roughness measured from the AFM surface plot is around 7·13 nm. The thickness of alumina film on amorphous
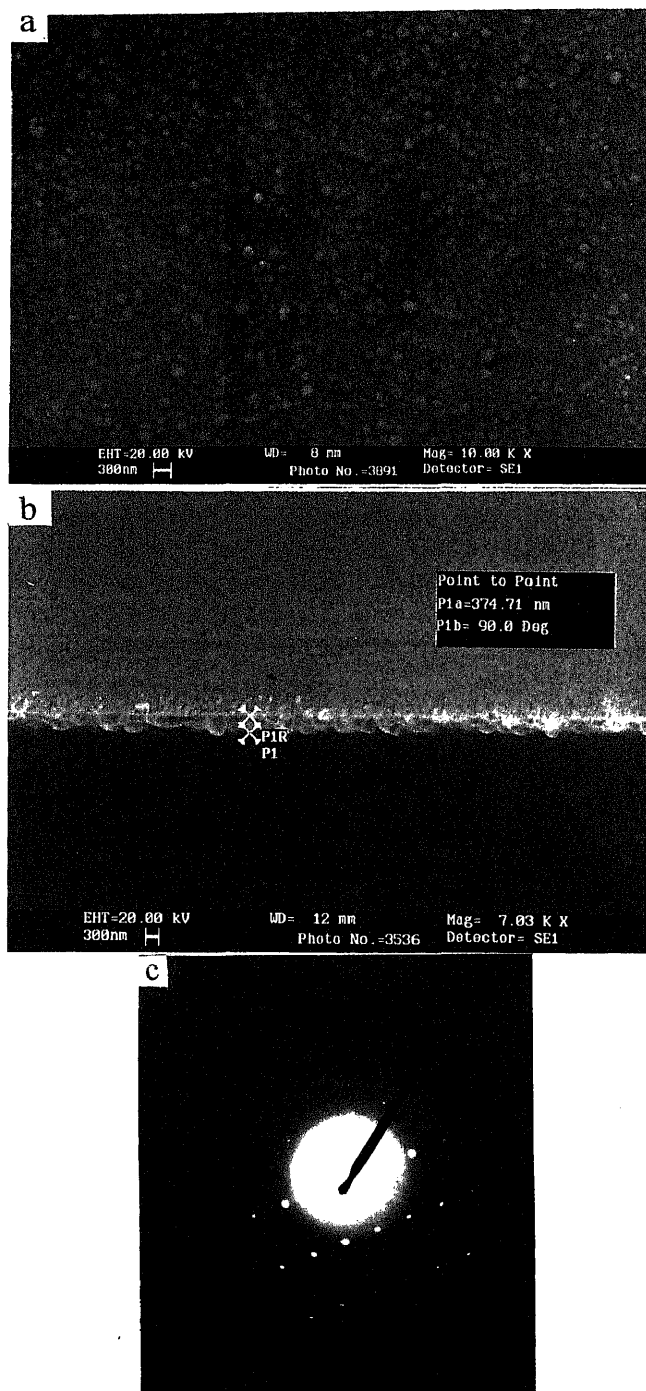
Figure 1. a. Scanning electron micrograph of an Al_2O_3 film deposited on Si(100), b. cross sectional SEM micrograph of the Al_2O_3 film deposited on Si(100) (film thickness is 350 nm)
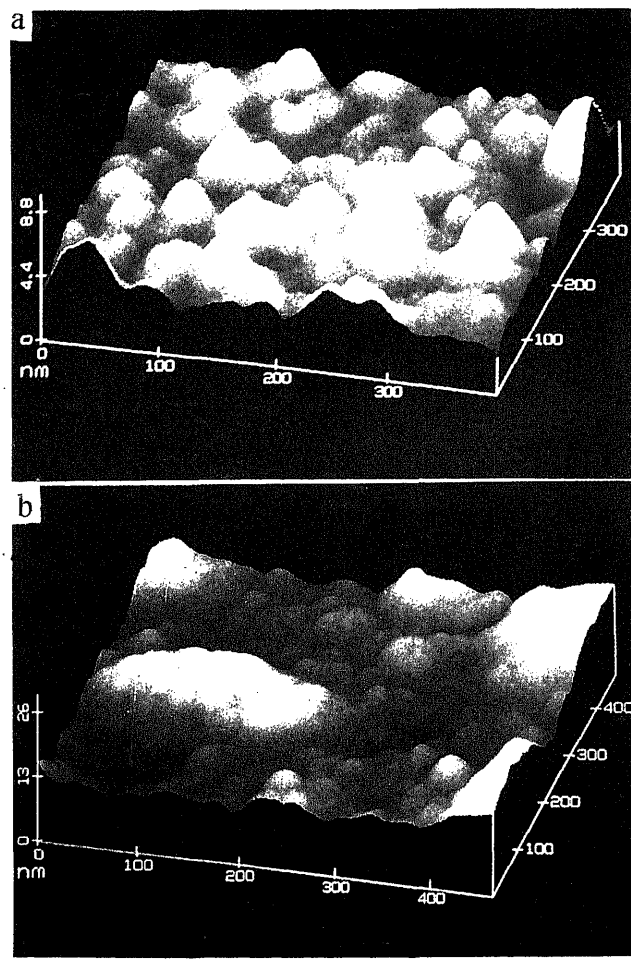
silica substrate is around 753 nm as delineated from the cross sectional SEM image in figure 3b.

The as-grown alumina films on both Si(100) and amorphous silica substrates were amorphous. After heating the film deposited on silica at 973 K for 12 h, we obtained the X-ray diffraction pattern shown in figure 4. The pattern corresponding to the κ-phase. We did not see any reflections in the X-ray diffraction pattern of the alumina films deposited on Si(100) substrates at 673 K since the films were very thin. The electron diffraction pattern (figure 1c) of a peeled portion of the annealed alumina film however revealed alumina was in the κ-phase.

In figure 5 we show the variation of dielectric properties with frequency (100 Hz–5 MHz) of Al_2O_3 films on Si(100) as well as SiO_2 substrates. There is only little variation in the capacitance with frequency, whereas the tan δ increase at higher frequency in the case of the film on Si and decreases with frequency in the film on SiO_2.

We have measured the dynamic microhardness of the alumina films deposited on Si(100) and amorphous silica substrate with a 50 mg load applied over 10 sec. We obtained a hardness value as high as 2010 in dynamic hardness unit (DHU) and an average of 1330 DHU from 10 measurements on different areas of the alumina film deposited on Si(100) substrate. However, the maximum hardness value of the film deposited on amorphous silica substrate was 2610 DHU with an average value of 1655 DHU from 10 measurements.

4. Conclusions

We have deposited alumina films on Si(100) as well as
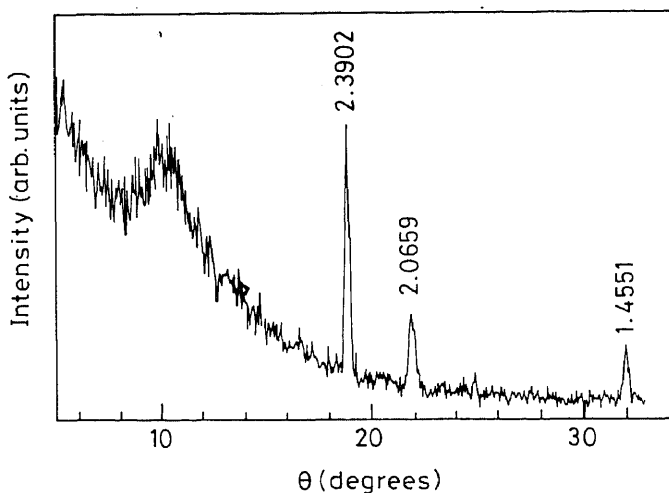
Figure 4. X-ray diffraction pattern (θ–θ scan) of an Al_2O_3 film deposited at 673 K on amorphous silica substrate and annealed at 973 K for 12 h.

Figure 3. a. Scanning electron micrograph of an Al_2O_3 film
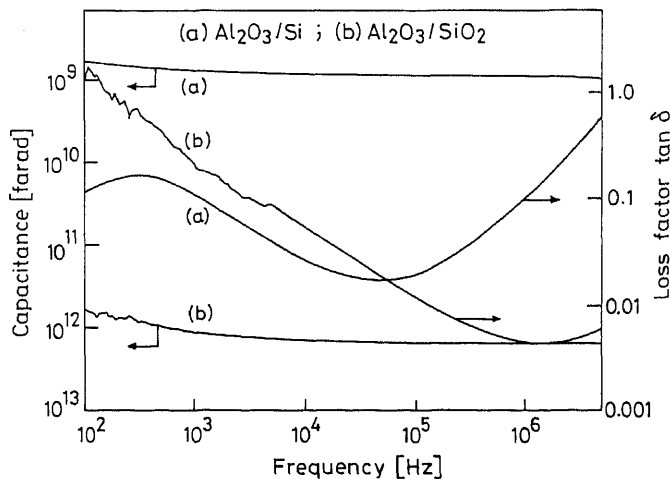
SiO$_2$ substrates by nebulized spray pyrolysis using aluminium acetylacetonate as the precursor. The as-deposited films are amorphous and crystallize to κ-alumina after annealing the films at 973 K for 12 h. Dielectric measurements show variation of the capacitance with frequency in the films to be small, suggesting that they may be useful for high frequency capacitor applications. The average dynamic microhardness of the films deposited on Si(100) and SiO$_2$ is substantial.

Acknowledgement

References

Aiyer H N, Raju A R and Rao C N R 1997 *Chem. Mat.* **9** 755

Caballero A, Leninen D, Fernandez A and Gonzalez-Elipe A R 1996 *Surf. & Coat. Technol.* **80** 23

Ciliberto E, Fragala I, Rizza R and Spoto G 1995 *Appl. Phys. Lett.* **67** 1624

Fredriksson E and Carlsson J O 1993 *Surf. & Coat. Technol.* **56** 165

Iizuka H, Yokoo K and Ono S 1992 *Appl. Phys. Lett.* **61** 2978

Ishida M, Katakabe I, Nakamura T and Ohtake N 1988 *Appl. Phys. Lett.* **52** 1326

Kim J S, Marzouk H A, Reucroft P J, Robertson J D and Hamrin C E 1993 *Appl. Phys. Lett.* **62** 681

Maruyama T and Arai S 1992 *Appl. Phys. Lett.* **60** 322

Raju A R, Aiyer H N and Rao C N R 1995 *Chem. Mat.* **7** 225

The epitaxial growth of Ag on Si(111)–(7 × 7) surface and its (√3 × √3)–R30 surface phase transformation

S M SHIVAPRASAD*, SANTANU BERA[†] and Y APARNA

Surface Physics Group, National Physical Laboratory, Dr K S Krishnan Marg, New Delhi 110 012, India
[†]Present address: Applied Chemistry Division, Bhabha Atomic Research Centre, Kalpakkam 603 102, India

Abstract. Ag is adsorbed in ultra-high vacuum on to the (7×7) reconstructed Si(111) surface with submonolayer coverage control with a deposition rate of 3.3×10^{12} atoms/cm^2/sec. The initial stages of growth and intermediate equilibrium phase formation are determined by using low energy electron diffraction (LEED) and X-ray photoelectron diffraction (XPD) for structural information, and auger electron spectroscopy (AES) and electron energy loss spectroscopy (EELS) for composition and interaction analyses. Room temperature (RT) adsorption results in the nearly epitaxial (1×1) surface phase growth in the simultaneous multi-layer growth mode. The quenching of the dangling bond states during adsorption is observed by monitoring the p-character of the Si LVV auger peak. For depositions carried out at high temperatures (HT), several plateaus in the auger uptake curve with the (√3 × √3)–R30° LEED structures are formed. It is observed that a minimum coverage of 0·33 monolayer (ML) is required for the formation of the (√3 × √3) phase and this phase causes the reappearance of the p-electron-related states that were quenched by 1·0 ML adsorption at RT. However the (√3 × √3) is observed for higher coverages (0·66 and 1·0 ML) also. The polar angle anisotropy of Si($2p$) emission in XPD indicates the rearrangement of substrate Si atoms for the formation of the (√3 × √3) phase. The EELS data also shows relevant changes due to adsorption of Ag at RT and upon annealing. The results suggest the importance of controlled deposition parameters, the lack of which may have kept the determination of the nature and coverage of the (√3 × √3) surface phase unresolved in literature.

Keywords. Solid phase epitaxy; metal–semiconductor interfaces; surface phase transitions; Auger electron spectroscopy; low energy electron diffraction; X-ray photoelectron diffraction.

1. Introduction

Motivated by the need to produce high performance and reliable devices of diminishing size, the VLSI/ULSI R&D has encouraged the studies of extremely low-dimensional structures. Modern growth techniques with submonolayer control of structure, composition and doping, enable the synthesis of new materials with novel properties (Gossmann and Schubert 1993). Of the many issues under this broad scheme, the semiconductor to metal contact remains one of the principal priorities for metallization (Ohmic contacts, Schottky barrier control) or delta-doped and buried layer structures. The precise relationship between the crystallographic structure, the chemical composition and the electrical properties at the boundary between metal and semiconductors are of critical technological and fundamental interest (Monch 1990). Most of the conventional theoretical treatments of metal/semiconductor interfaces have made the key assumption that the interface is well ordered and perfectly

abrupt on an atomic scale. But in reality, strong chemical interactions, intermixing and diffusion occur at surfaces which necessitate a re-evaluation of conventional ideas, both theoretically and experimentally. Due to the stringent experimental requirements for the formation and accurate characterization of the interfaces, precise control of the very initial stages of growth are observed to determine the nature of growth (Shivaprasad *et al* 1995, 1997).

Of the several metals on Si systems studied in the last two decades, Ag/Si the prototype system, has been the most intensively studied mainly due to minimal chemical interaction between the two elements on both Si(111) and (100) surfaces. The Si(111) surface attracted more attention (Le Lay 1983; Lifshits *et al* 1994), initially due to the early observation of the (√3 × √3) superstructure, while the Si (100) was said to be without any new superstructure. However, with improvements in experimental techniques and control of deposition parameters, the interest in these systems has been renewed and has led to the observation of new superstructural equilibrium states in the Ag/Si (100) (Shivaprasad *et al* 1995). Differences still exist in the details of the Ag/Si(111)

---

*Author for correspondence

at RT and also form many equilibrium surface phases for the Mn/Si(111) system (Shivaprasad *et al* 1997).

1.1 *The* $(\sqrt{3} \times \sqrt{3})$ *structure*

Several results (Wan *et al* 1993) indicate that Ag grows at RT on Si(111) (7×7) surface in the Stranski–Krastanov (S–K) mode. The nature and coverage of this intermediate 2-D has no consensus and is controversial in literature, with the (7×7) reconstruction observed to be vanishing in the formation process. At higher temperatures the S–K mode displays an intermediate layer of $(\sqrt{3} \times \sqrt{3})$–R30 surface phase reconstruction. This reconstruction is the second smallest of the Si(111) surface and occurs frequently in metal/Si interface systems (Kono 1988). It has been established that the $(\sqrt{3} \times \sqrt{3})$ symmetry appears due to various atomic arrangements, depending on the energetics of the overlayer coverage (Northup 1984; Kono 1994). In case of Gr. III and Gr. IV metals the atoms are recognized to be adsorbed at the two kinds of three-fold hollow sites T_4 and H_3 on Si(111) (see figure 1) and require a coverage of 0·33 ML. However, for Gr. V metals, the $(\sqrt{3} \times \sqrt{3})$ was observed for a coverage of 1 ML which has been attributed to the presence of metal trimers centred above the T_4 and H_3 three-fold hollow sites, referred to as the milk-stool model. In the Ag on Si(111) case, the coverage of this structure has remained controversial and has reported values between 0·33 to 1·0 ML and is recently said to be preparation history dependent (Raynerd *et al* 1992). A modified honeycomb-chained trimer (HCT) model (Katayama *et al* 1991) with a Ag coverage of 0·66 ML has found wide acceptance (also shown in figure 1). In the present work, the Ag/Si(111) system is studied with a view of addressing some of the unresolved issues.

In this study it is observed that Ag grows epitaxially in the simultaneous multilayer mode at RT and assumes the S–K mode upon post-annealing or upon deposition at higher substrate temperatures with the intermediate layer having a $(\sqrt{3} \times \sqrt{3})$ structure. The molecular-beam evaporation is probed *in situ* with a multi-technique approach using auger electron spectroscopy (AES), low energy electron diffraction (LEED), X-ray photoelectron spectroscopy (XPS), electron energy loss spectroscopy (EELS) and X-ray photoelectron diffraction (XPD). The epitaxial (1×1) and the $(\sqrt{3} \times \sqrt{3})$ structural phases observed are discussed in terms of the dangling bond manifestation and the coverages involved.

2. Experimental

The experiments were performed in two UHV systems: (i) a Varian VT-112 equipped with a single-pass *in situ* Ag adsorption, operating at a base pressure of 3×10^{-11} mbar, and (ii) a Perkin Elmer (PHI) system with a 280 mm HSA and a dual Anode (Mg/Al) K_{α} X-ray source and a 0–4 keV electron gun. Ag was evaporated from a water-cooled W-filament at a base pressure of 3×10^{-10} mbar.

The Si substrates were suitably cut from Si(111) *p*-type, 5–10 $\Omega \cdot$ cm wafers and chemically cleaned by the modified Shiraki Process (Enta *et al* 1989) before being introduced in the UHV chambers. These samples were mounted on high-precision manipulators (with four degrees of freedom x, y, z, θ), designed to accurately place the sample in front of the sources, analyzer and LEED optics etc. The samples were heated *in situ* in the two UHV systems resistively and by electron bombardment respectively, to 1200°C for a few min and then annealed at 900°C for 20 min, to obtain a sharp (7×7) LEED and a characteristic XPD of Si($2p$), respectively. The impurities like C and O were below the detection limits of AES and XPS. The cleanliness of the Si(111) surface is also evident by the observation of at least seven multiple plasmon losses of 17 eV each in the EELS spectrum. The temperatures were measured by a thermocouple (for $T < 500°C$) and an optical pyrometer (for $T > 600°C$). The Ag films were deposited on to the substrates with a slow deposition rate of typically 0·2 ML/min, where 1 ML corresponds to $7·83 \times 10^{14}$ atoms/cm^2, the atomic density of a bulk-terminated Si(111) (1×1) surface.

AES was measured by a single-pass CMA, with 0·18% energy resolution, using a primary beam energy E_p of 3 keV by lock-in techniques in the dN/dE mode, with peak-to-peak voltage of 10 V. EELS was measured by the same system in the second derivative mode for E_p of 250 eV with a peak-to-peak voltage of 2 V for improved resolution. The LEED patterns were observed in a 4-grid optics with electron beam energy varying from 20 eV to 500 eV. XPS data was acquired in the pulse counting mode by a computer interfaced to the 280 mm hemispherical analyzer with a typical pass-energy of 50 eV, using Mg K_{α} X-ray source at 1443·3 eV, while the valence band features were observed with a pass energy of 10 eV for better resolution. Polar Angle-XPD was performed by manually rotating the sample to change the angle about an axis passing through it and parallel to the surface by 2° steps. The flat response of the analyzer in the angular range studied and the acceptance angle of $< 2°$ were ascertained beforehand. Though the experiments were performed in two different systems and probed by different techniques, identical preparation conditions were adopted and monitored for stoichiometry and coverage by AES in both cases.

3. Results and discussion

The results obtained for RT deposition and those for higher temperatures are presented under two sub-sections (3.1 and 3.2) for clarity of presentation. The results are discussed in light of the various models shown in figure 1 for the $(\sqrt{3} \times \sqrt{3})$ surface structural phase.

3.1 *Room temperature*

Figure 2 shows the Ag-uptake curve on the Si(111) surface. The curve is obtained by rotating the samples to face the K-cell for Ag adsorption and then to the CMA to obtain the AES spectrum after each deposition.
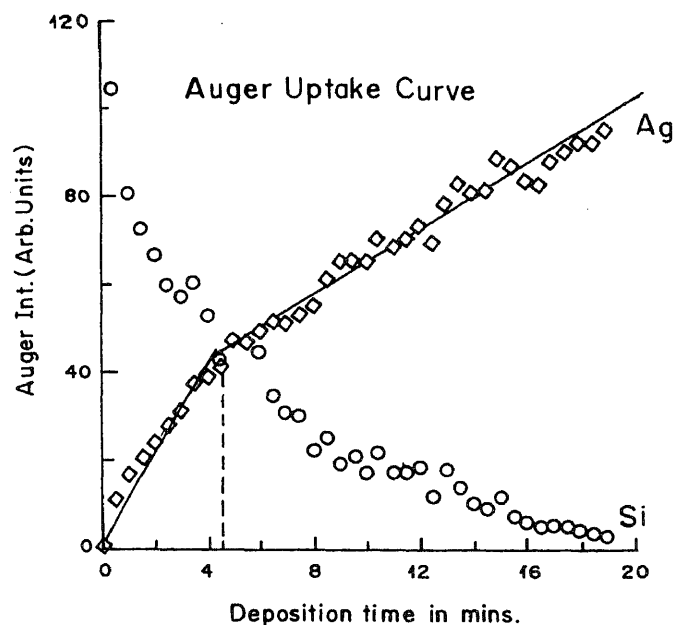
The X-axis shows the time of deposition while the Y-axis is the Auger amplitude of the 92 eV LVV peak for Si and the 356 eV MNN transition for Ag. As more Ag is deposited, the Ag signal increases while the Si signal is reduced. The initial segment of the Ag amplitude, which is close to being linear, shows a change in slope at about a deposition time of ≈ 5 min. This change in slope indicates the completion of the first adsorbed layer, after which the signal from the first layer is attenuated by the presence of the second layer atoms (Argile and Rhead 1989). The break in the linearity is clearer in the Ag signal than in the Si signal due to the varying depth of information in the two species. This not only provides a calibration for the first monolayer and deposition rate, but also clearly indicates that the first layer is flat and that the growth is not in the Volmer–Weber (Island) growth mode. The latter part of this curve appears to be linear as in the case of a simultaneous multilayer growth mode which will be discussed later.

Figure 3a shows the LEED image at 50 eV of a clean Si(111)–(7 × 7) reconstructed surface while figure 3b shows the characteristic polar angle (PA-)XPD pattern of Si(111) along (1T0) direction (Bishoff *et al* 1992). The LEED pattern taken at 50 eV incident beam energy shows clear six-fold symmetry in the (1 × 1) spots, between which are the six less intense spots manifesting the (7 × 7) reconstruction in reciprocal space. Figure 3b is the polar angle plot of the XPD signal, clearly showing the anisotropy in the Si(2*p*) emission, due to the predominant forward scattering of electrons, of these ener-

Figure 1. Shows schematically the models for the adsorption sites of Ag (open circles) on the (1 × 1) Si (filled circles)

Figure 2. Adsorption of Ag on Si(111) plotted as the auger

gies, originating from one atom by the neighbouring atoms (Egelhoff 1990; Chambers 1991). Since the information depth of the Si(2p) (≈ 1340 eV) electrons in XPS is quite large, the pattern is not expected to manifest the reconstruction of the first few layers of the substrate.

Figures 4a and b are respectively the LEED and XPD (polar angle) pattern modified after deposition of 1 ML of Ag. Though the experiments have been performed for several coverages, the 1 ML LEED and XPD patterns are presented as being representative. The LEED pattern shows clearly that now the (7×7) spots have disappeared while the (1×1) six-fold spots are weak but sharp (Kohomoto and Ichimiya 1987). However the dominant spots are the slightly elongated spots radially above each of the (1×1) spots. These spots are attributed to the Ag(111) reflexes, which are commensurate with the Si(111) (1×1) spots. This indicates that Ag is growing epitaxially on Si(111) at these slow rates at RT (Bera and Shivaprasad 1995). This was also manifested in the AES uptake curve as a linearity of the later segment of the plot. However the Ag(111) (1×1) reflexes are not sharp, and even show a weak full circle, indicating that
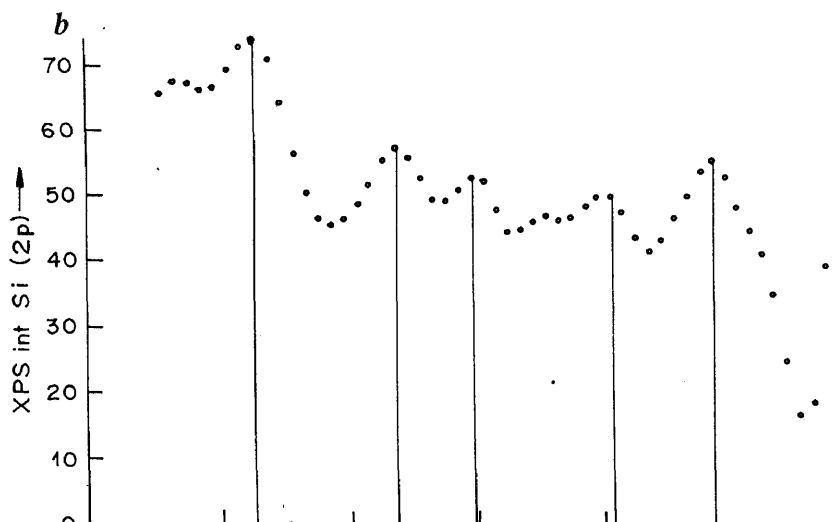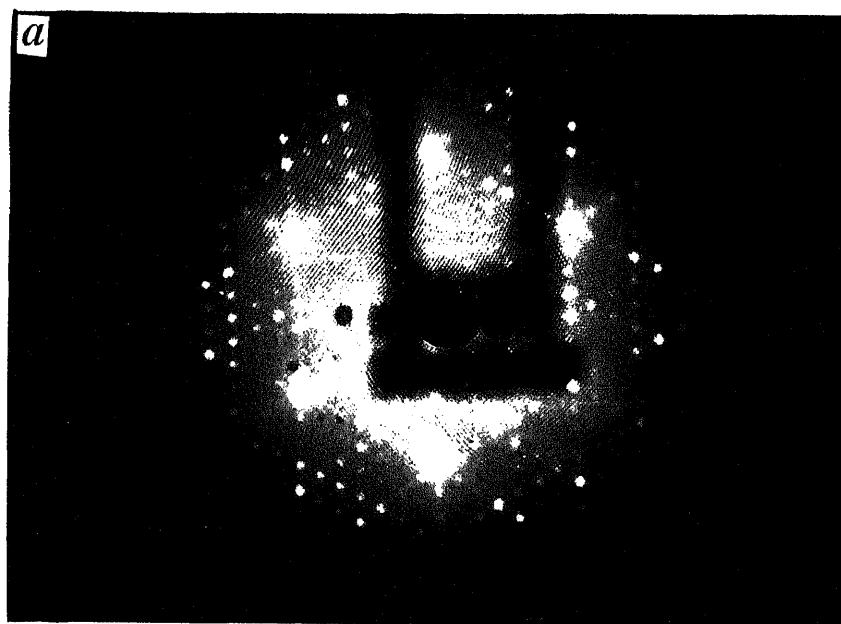
the Ag has adsorbed probably in the simultaneous multilayer growth mode, with several two-dimensional flat islands, with some misorientation between them (Bauer 1982). The (1×1) spots indicate that the Ag(111) grows parallel to the Si(111), with little chemical inter-action between the two elements at the interface. The corresponding PA–XPD in figure 4b, also shows signifi-cant changes in its features. Note that the XPD obtained in one quadrant experimentally has been presented by laterally inverting it in the other quadrant. This change in pattern can be attributed to the scattering of Si(2p) electrons by the presence of Ag adatoms. The presence

of the Si(1×1) pattern in LEED dissuades us from interpreting the XPD results as due to the rearrangement of Si atoms in the first few layers.

Figure 5 represents the Si LVV auger peak finger-printing results for both room temperature and higher temperature deposition. The deconvolution of the Si(LVV) auger peak in the $N(E)$ mode, enables the extraction of the contribution of the p-electron states to the Auger transition (Ramaker *et al* 1986). The density of the dangling bonds (valence band states), which are pre-dominantly p- in character, can thus be monitored by observing changes in the intensity of the corresponding
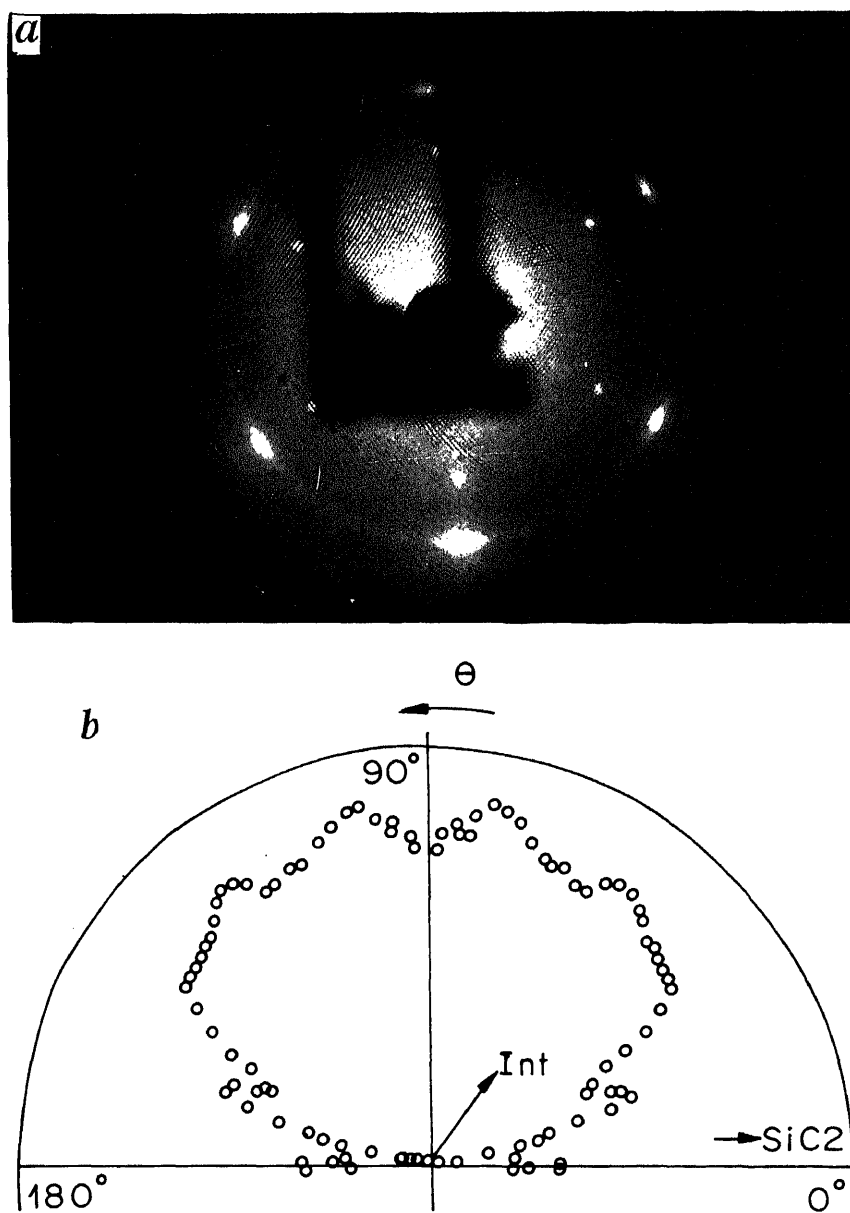

Figure 4. a, LEED pattern obtained with energy of 50 eV after adsorbing 1 ML of

components. This becomes easily accessible in the Auger spectra acquired in the first derivative mode, since the upper excursion of the peak corresponds directly to the *p–p* electron state contribution (L_{pp}), and the lower excursion is due to the *s–s* and *s–p* states (L_{ss}). Thus in figure 5 the plot of the ratio of the positive to the negative excursion (L_{pp}/L_{ss}) of the Si (LVV) 92 eV peak as a function of Ag deposition, manifests the change in the valence band due to the changing dangling bond density. The figure shows clearly that the dangling bonds are quenched monotonically with increased Ag deposition, and reduce to zero intensity at 1 ML. This confirms the observations by LEED during deposition, where the 1/7th order spots also diminish at 1 ML, removing the (7×7) reconstruction.

Figure 6 shows some EELS spectra obtained with primary energy of 650 eV, both during the Ag uptake sequence (a–d) and annealing (e–f) of a 5 ML Ag deposited system at different temperatures. The origins of all the loss peaks observed for clean Si(111) have been assigned previously (Ibach and Rowe 1974; Sharma *et al* 1988a). The clean Si(111) (7×7) surface shows the characteristic loss to the 17 eV ($\hbar\omega_p$) bulk plasmon and the 11 eV ($\hbar\omega_s$) surface plasmon, and an intraband transition at about 5·5 eV (E_2). The loss of peaks at 7·5 eV (S_2) and 14·5 eV (S_3) are attributed to transitions involving surface states. As the deposition of Ag at RT proceeds, the Si surface-related peaks disappear quickly, while the bulk features decrease gradually. At the com-

pletion of 1 ML of Ag deposition, the Ag-related peak excitations (Jaspard *et al* 1980) become prominent. At a coverage of 5·0 ML, the EELS pattern resembles that of bulk Ag with features at 4·5 eV and 7·5 eV. This has been explained to be due to strong transitions from the Ag d-band to states in the *sp* conduction band just above the Fermi level. The absence of the formation of any interfacial peak shows lack of interaction between the two species. The changes due to annealing of the system (e,f) will be discussed in the next section.

3.2 *High temperature*

In this section we discuss the effects of temperature on the structure of the Ag/Si(111) system. As seen in figure 4, the Si (1×1) and the disordered Ag (1×1) reflexes are clearly observed in the LEED pattern. After annealing to about 150°C, the rearrangement of the Ag and Si atoms are manifested in LEED and PA–XPD as shown in figures 7a and b, respectively. The LEED pattern shows that the Ag spots get sharper and the Si (1×1) spots also intensify, suggesting the enhancement of long range order of the surface structure. Though there are some new and sharp spots, the transition in this intermediate state is clearly not complete. The changes are
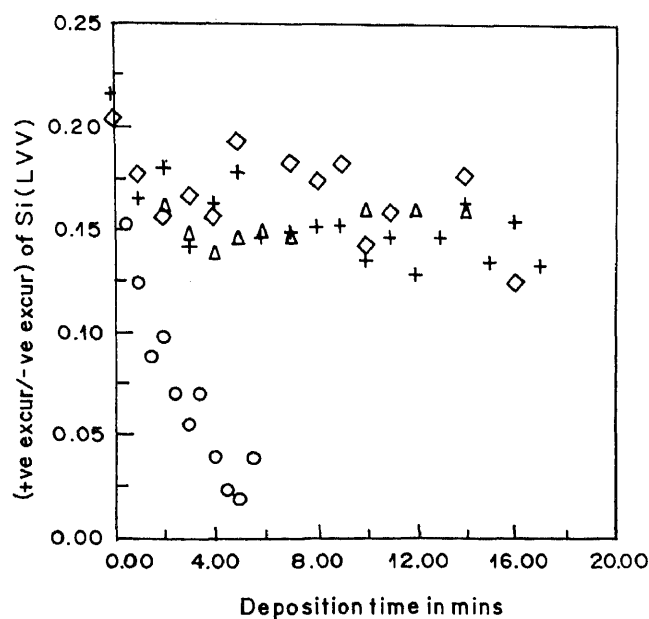
Figure 5. The ratio of the upper excursion (L_{pp}) to the lower excursion (L_{ss}) of the 92 eV Si LVV peak obtained in the
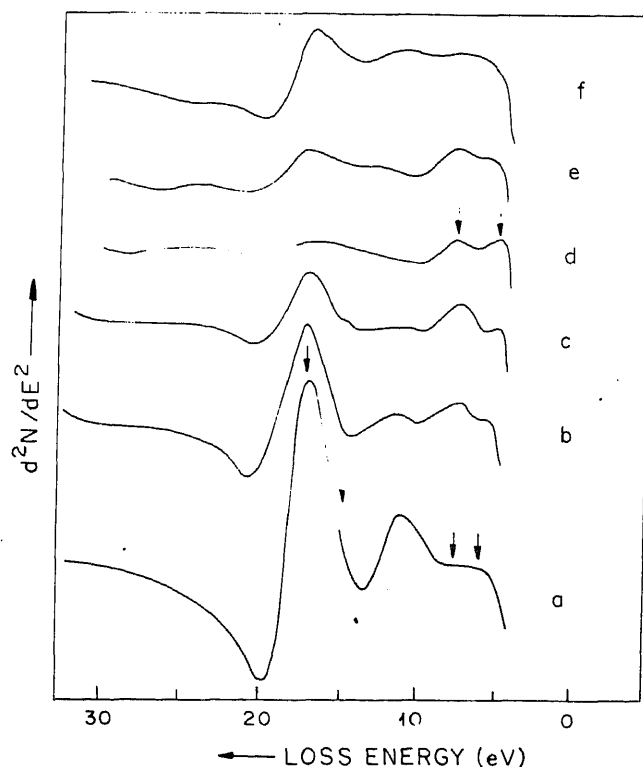
Figure 6. The EELS spectra obtained with an incident beam

suggesting a better ordering of the atoms in the overlayer and the substrate selvedge.

Further annealing to about 250°C, completes the phase transition as seen in figure 8. Figure 8a shows a different, yet very sharp LEED pattern and the background is also considerably reduced, showing a homogeneity in this surface phase. The inner hexagon is clearly rotated by 30° with respect to the outer hexagon whose side is $\sqrt{3}$ times the side of the inner hexagon and is termed as the $(\sqrt{3} \times \sqrt{3})$–R30°C–Ag pattern. The corresponding XPD pattern again changes in figure 8b which can either be due to scattering of the Si($2p$) electrons by the

substrate held at different substrate temperatures is presented in figure 9. The curves clearly show that at higher temperatures, the Ag/Si auger ratio behaves differently, showing a sudden flattening at about 0·33 ML (1·0 ML coverage is attained by deposition time of 5 min), characteristic of the Stranski–Krastanov growth mode. In this flat region corresponding to a surface structural phase, the LEED is observed to be (7×7), but with some modifications in intensity, suggesting possibly the $\delta(7 \times 7)$ surface phase as reported earlier (Kohomoto and Ichimiya 1987; Shivaprasad et al 1997). For substrate temperature of 100°C, after 1 ML, the Ag again begins
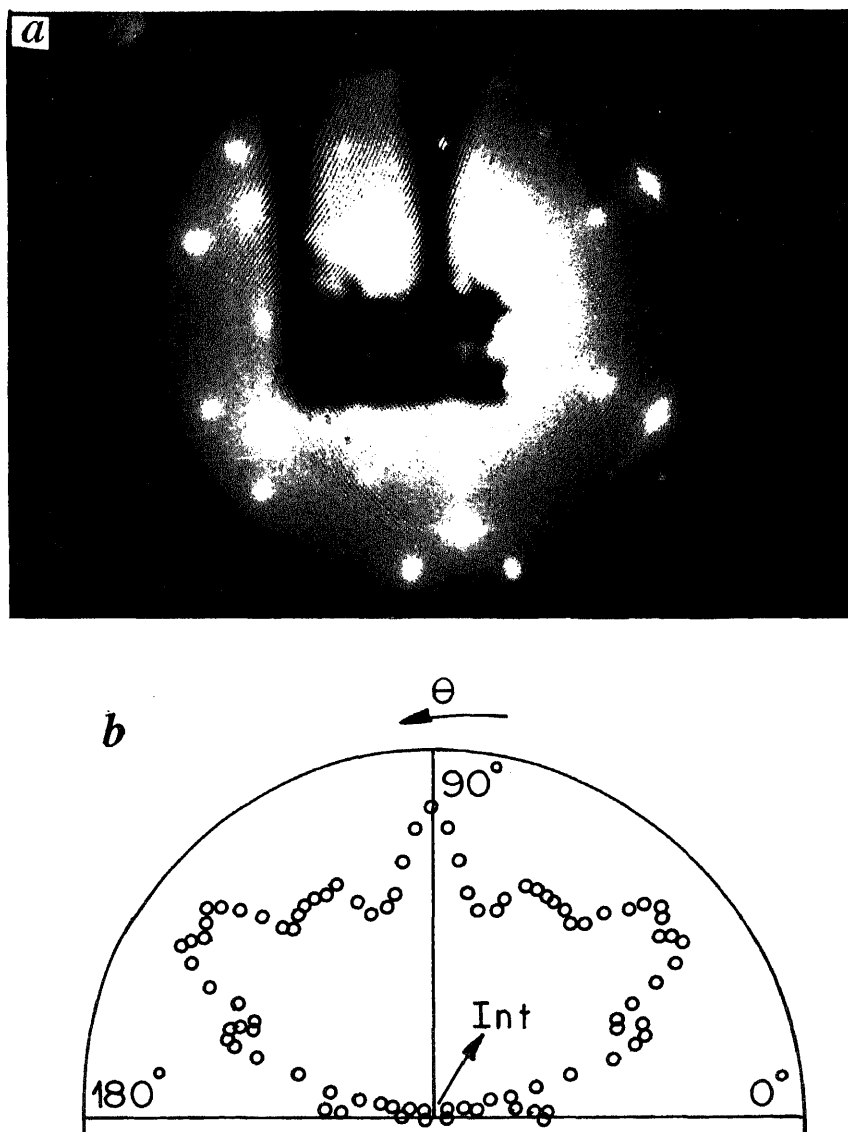
Figure 7. a. The LEED pattern of the 1 ML Ag/Si(111) surface annealed to 150°C showing an intermediate surface phase between the (1×1) and (3×3) and b. the corresponding XPD-PA pattern along $(1\bar{1}0)$.

the next surface phase. Again for both the 100°C and 150°C curves, it is clear that they show two more plateaus which also correspond to structural surface phases with $(\sqrt{3} \times \sqrt{3})$ symmetry as observed by LEED.

Figure 5 which consolidates the fingerprinting (p-component study) results of the auger studies for the Ag deposition at room and higher temperatures shows the dangling bond intensity versus the deposition time. It is very clear from this figure that the +ve to −ve excursion ratio (L_{pp}/L_{ss}) of the Si LVV 92 eV peak almost remains constant (with some scatter) around a ratio of 0·15 for all temperatures and coverages. However for RT deposition this ratio has clearly decreased to 0 for 1 ML deposition indicating the complete quenching of

partially and the surface phase that gives the $(\sqrt{3} \times \sqrt{3})$ LEED pattern, actually causes the re-formation of the dangling bonds. The small amount of quenching also indicates a small coverage of Ag necessary to form the ordered surface phase, as seen in the plateau formation in figure 9. Annealing at 250°C shows that the plateau is for a coverage of 0·33 ML, on which excess Ag atoms agglomerate to form islands, thus occupying only a small fraction of the Si surface.

The EELS spectra in figure 6 also shows the annealing sequence of the 5 ML Ag coverage deposited system at higher temperatures (curves e, f). The features show the re-occurrence of the Si bulk and surface plasmon-related features (Sharma *et al* 1988b). The dip before the 17
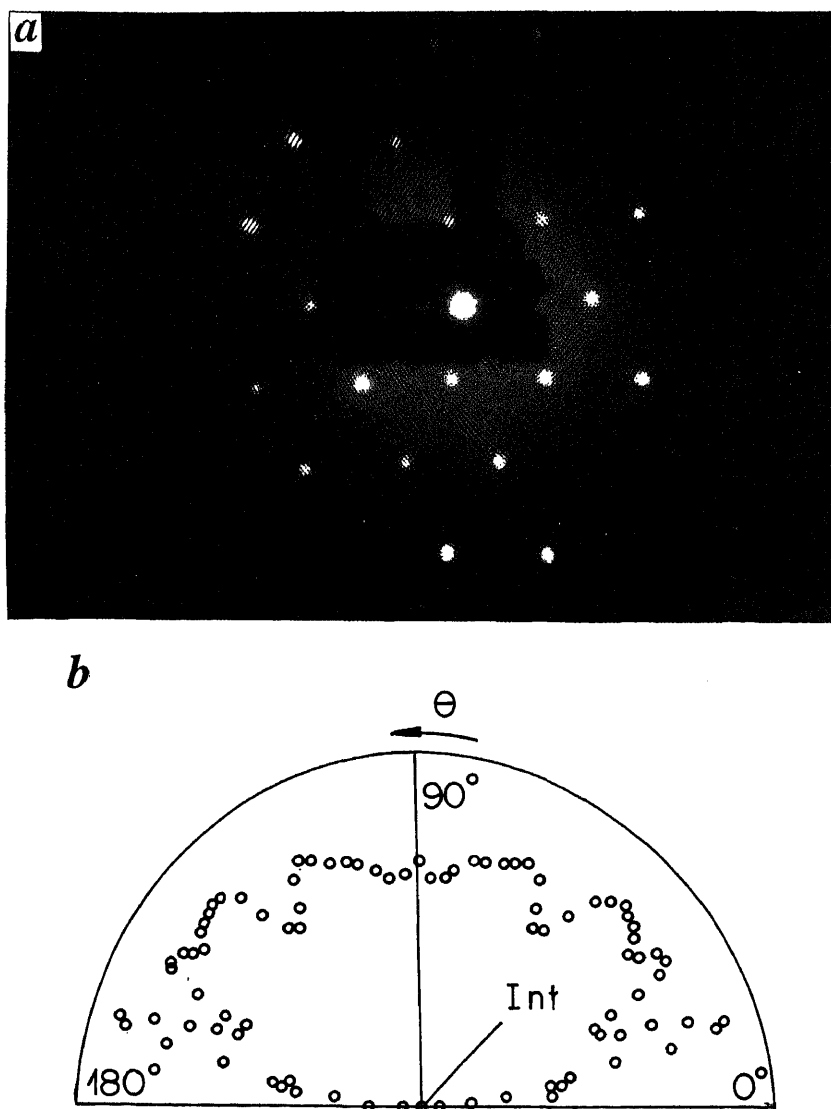
Figure 8. a. The LEED pattern of the $(\sqrt{3} \times \sqrt{3})$ R–30 structural surface phase obtained by annealing 1 ML Ag/Si(111) system annealed to 250°C and **b**. the corresponding XPD pattern along $(1\bar{1}0)$ direction.
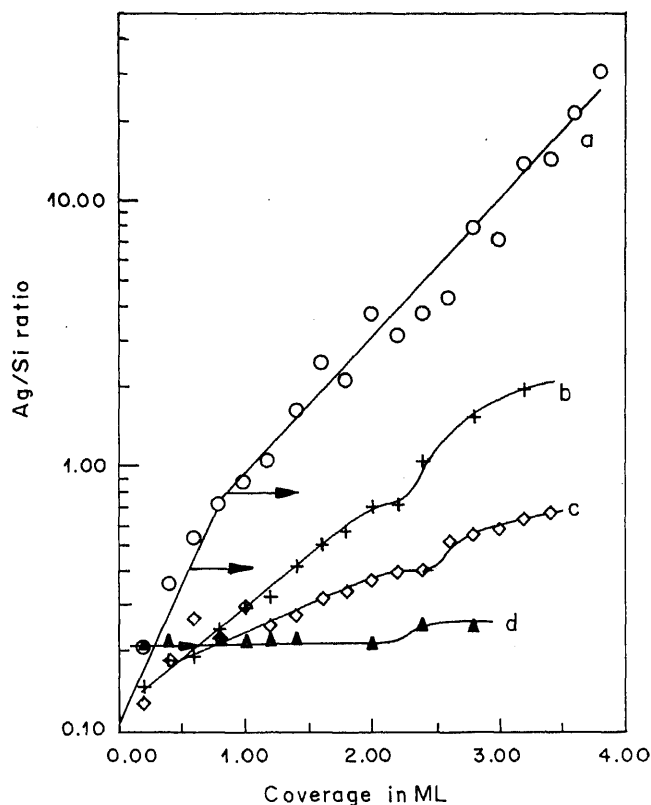
Figure 9. The Ag uptake curve shown by plotting the Ag(LMM)/Si(LVV) peak intensity ratio, obtained for different substrate temperatures: (a) **O**, room temperature, (b) +, 100°C, (c) ◊, 150°C and (d) ▲, 250°C.

eV peak also deepens as in the clean Si case. However the features now appear slightly broadened. The widths of the observed peaks and shifts of the 12 eV peak to 11 eV and the peak at 8 eV to 7 eV in the case of curves e and f with different Ag coverages, may indicate the differences in the two ($\sqrt{3} \times \sqrt{3}$) structural phases.

4. Conclusion

The adsorption of sub-monolayer coverages of Ag onto Si(111) surface is studied *in situ* by AES, LEED, XPD and EELS techniques. It is observed that Ag grows epitaxially on Si(111) with the Ag(111) parallel to Si(111) at RT. The p-character of the Si auger emission (dangling bond states) are sharply quenched at 1·0 ML coverage. At higher substrate temperatures (or with post annealing), a $\delta(7 \times 7)$ surface phase is observed for coverages lesser than that required for the onset of the ($\sqrt{3} \times \sqrt{3}$)–R30° phase. The dangling bond states reappear in the ($\sqrt{3} \times \sqrt{3}$) phase, and the EELS also assumes the clean Si features. The sharp ($\sqrt{3} \times \sqrt{3}$) phase is seen at a minimum of 0·33 ML coverage. The auger uptake curve

of different atomic structures with characteristic densities, leading to the ($\sqrt{3} \times \sqrt{3}$) phase.

The presence of many models (Lifshits *et al* 1994) for the ($\sqrt{3} \times \sqrt{3}$) phase of Ag/Si(111) (7 × 7) shows that the problem of determining the exact structure of a stable surface phase is still unresolved. Our experiments using a multi-technique approach and a careful observation of temperature dependence, suggest that the minimum coverage necessary to form the ($\sqrt{3} \times \sqrt{3}$) phase is 0·33 ML, while other subtle phases with different Ag density (coverages of 0·66 and 1 ML), but the same LEED pattern, are also observed. However, the new approach of looking at the p-electron contribution shows that though the dangling bonds are quenched by adsorption of Ag at RT epitaxially, the ($\sqrt{3} \times \sqrt{3}$) phase shows the re-appearance of the p-electron character. This is observed by our EELS measurements also. Our PA–XPD has evidence for the rearrangement of Si substrate. It has been shown recently for the Ag/Si(100) system, that a massive reconstruction of the Si substrate is observed by scanning tunneling microscopy (Wan *et al* 1993). Thus, further experiments are necessary to determine the atomic structural model for each of the coverage dependent stable surface phases that have the same ($\sqrt{3} \times \sqrt{3}$) LEED symmetry. Thus Ag of 0·33 ML probably results in the adsorption of adsorbates at the T_4 and H_3 sites, while the 1 ML may be because of the Ag trimer adsorption at the above sites. There is also a stable ($\sqrt{3} \times \sqrt{3}$) phase at 0·66 ML, which has been explained by the HCT model. The XPD patterns with adsorption and annealing show significant changes and since the scattering of Si(2p) electrons from several layers by even 0·33 ML Ag atoms may be small, the results suggest a restructuring of several layers of the substrate Si atoms also.

A more complete polar and azimuthal angle XPD experiments with single/multiple scattering calculations and simultaneous probe with other complementary techniques are necessary to reveal the details of the surface phases. Detailed EELS experiments are underway to obtain further information on the electronic structures of the various phases. Observation of an epitaxial growth of Ag on Si(111) at RT and the recent works on Ag/Si(100) (Shivaprasad *et al* 1995) and Mn/Si(111) (Shivaprasad *et al* 1997) clearly indicate that a proper control of the deposition rate and temperature determine the formation of various surface phases, suggesting the need to re-examine many metal/semiconductor systems in general and metal/Si in particular.

References

Argile C and Rhead G E 1989 *Surf. Sci. Rep.* **10** 277

Bauer E 1982 *Appl. Surf. Sci.* **11/12** 479

Bera S and Shivaprasad S M 1995 *Bull. IVS* **26** 45

Bishoff J L, Kerbler L, Lutz F, Diane M and Bolomont D 1992 *Solid State Commun.* **83** 823

Chambers S A 1991 *Adv. Phys.* **40** 357

Egelhoff Jr W F 1990 *Crit. Rev. Solid State & Mater. Sci.* **16** 1

Enta Y, Suzuki S, Kono S and Sakamoto T 1989 *Phys. Rev.* **B39** 56

Fadley C S 1984 *Prog. Surf. Sci.* **16** 275

Gewinner G, Kafder U, Wetzel P and Pirri C 1994 *J. Elect. Spec. & Rel. Phenom.* **67** 387

Gossmann H J and Schubert E F 1993 *Crit. Rev. Solid State & Mater. Sci.* **18** 1

Ibach H and Rowe J E 1974 *Phys. Rev.* **B10** 710

Jaspard J P, Derrien J, Cros A and Salvan F 1980 *Surf. Sci.* **99** 183

Katayama M, Williams R S, Kato M, Nomura E and Anno M 1991 *Phys. Rev. Lett.* **66** 2762

Kohomoto S and Ichimiya A 1987 *Appl. Surf. Sci.* **33–34** L765

Kono S 1988 *Core-level spectroscopy in condensed systems* (eds) J Kanamori and A Kotani (Berlin: Springer) p. 253

Kono S 1994 *Surf. Rev. & Lett.* **1** 359

Le Lay G 1983 *Surf. Sci.* **132** 169

Lifshits V G, Saranin A A and Zotov A V 1994 *Surface phases on silicon* (New York: Wiley) p. 52

Monch W 1990 *Rep. Prog. Phys.* **53** 221

Northup J E 1984 *Phys. Rev. Lett.* **53** 683

Ramaker D E, Hutson F L, Jurler N H and Mei W N 1986 *Phys. Rev.* **B33** 2547

Raynerd G, Doust T N and Venables J A 1992 *Surf. Sci.* **261** 251

Saitoh M, Shoji F, Oura K and Hanawa T 1981 *Surf. Sci.* **112** 306

Sharma J K N, Chakraborty B R, Shivaprasad S M and Cazaux J 1988a *Surf. Sci.* **93** L58

Sharma J K N, Chakraborty B R and Shivaprasad S M 1988b *J. Vac. Sci. & Technol.* **A6** 3120

Shivaprasad S M *et al* 1995 *Surf. Sci.* **344** L1245

Shivaprasad S M, Anandan C, Ayatzan S G, Gavriljuk Y L and Lifshits V G 1997 *Surf. Sci.* **382** 258

Wan K J, Lin X F and Nogami J 1993 *Phys. Rev.* **B47** 13700

Growth of anthraquinone crystals by gel aided solution technique and their characterization

K RAJENDRA BABU, M DEEPA, C M K NAIR[†] and V K VAIDYAN*

Department of Physics, University of Kerala, Kariavattom, Thiruvananthapuram 695 581, India
[†]Department of Physics, M.G. College, Thiruvananthapuram 695 004, India

Abstract. Anthraquinone, an oxidation product of anthracene, has been grown by gel aided solution technique employing sodium metasilicate. Needle shaped crystals were obtained in 0·5% (w/v) solution of anthraquinone for pH 5·5. The grown crystals were characterized by optical microscopy, SEM, IR, UV and XRD.

Keywords. Gel; solution; anthraquinone; crystal growth; oxidation; photoreaction.

1. Introduction

Derivatives of anthracene are convertible to other compounds by direct oxidation. Anthraquinone comes under this class of compounds. Considerable work has been reported on the synthesis of anthraquinone by catalytic oxidation of anthraquinone (Ivan and William 1949; Owens 1958; Noboru *et al* 1969; Grozev *et al* 1976; Chung 1978; Das and Nikhilendu 1982; Malik and Dohnal 1990; Pielichiouski *et al* 1992). The mesopositions in anthracene acquire the numbers 9 and 10, respectively. The successful outcome of the reaction is due to the special reactivity of the mesopositions and the greater stability of anthraquinone. The double bonds in the central ring are rendered inert by incorporation of oxygen in the terminal benzene rings (Louis and Mary 1960). Anthraquinone exhibits optical and photosemiconducting properties in addition to third harmonic generation (Yao 1962; Grozev *et al* 1976; Mizoguchi and Venishi 1991). Anthraquinone crystallizes in the monoclinic system with space group $P2_1/a$ ($a = 1·581$, $b = 0·3942$ and $c = 0·7865$ nm) with two molecules per unit cell. Here, we report the growth of anthraquinone observed during the growth of anthracene by the gel aided solution technique (Rajendra Babu *et al* 1998). The grown crystals are characterized by optical microscopy, SEM, IR, UV and XRD.

2. Experimental

The chemicals used in this study were of BDH/AR grade. Sodium metasilicate of gel density 1·05 g cm^{-3} was prepared, treated with glacial acetic acid in the pH range 5–7·5 and mixed with acetone for different gel acetone ratios (2 : 1, 3 : 1, 4 : 1). The mixture was allowed to set. The mixtures with higher pH (> 6·5) were set within 48 h, whereas those with lower pH (5) took nearly one week. Over the set gels, 0·5% (w/v) solution of anthracene in acetone was incorporated as top solution. The samples were kept open to diffuse sunlight. Few samples were kept in a dark room.

3. Results and discussion

It was observed that the level of top solution decreased slightly during the first week due to slow evaporation and diffusion into the gel. Tiny transparent crystals were observed floating on the surface of the top solution. Within two weeks, yellow needles were found growing from the tiny transparent crystals. Formation of yellow needles of anthraquinone is found to depend on several factors. An important parameter which determined the yield of anthraquinone was the concentration of anthracene solution kept over the gel. Higher concentration (1%) of anthracene solution produces a large number of anthracene crystals on the gel surface and tiny needles of anthraquinone were formed after a long period (~ two months). A better yield of anthraquinone resulted in a solution of concentration 0·5% (w/v) within two weeks.

A typical sample of gel, adjusted for pH 5, over which a few yellow needles of anthraquinone were formed is shown in figure 1A. In this case, tiny crystals formed on the surface of the top solution moved down to gel surface and yellow needles of anthraquinone were grown from them. In certain other gel samples when the illumination was high, large number of yellow needles were obtained.

Organic crystals can be grown from a wide variety
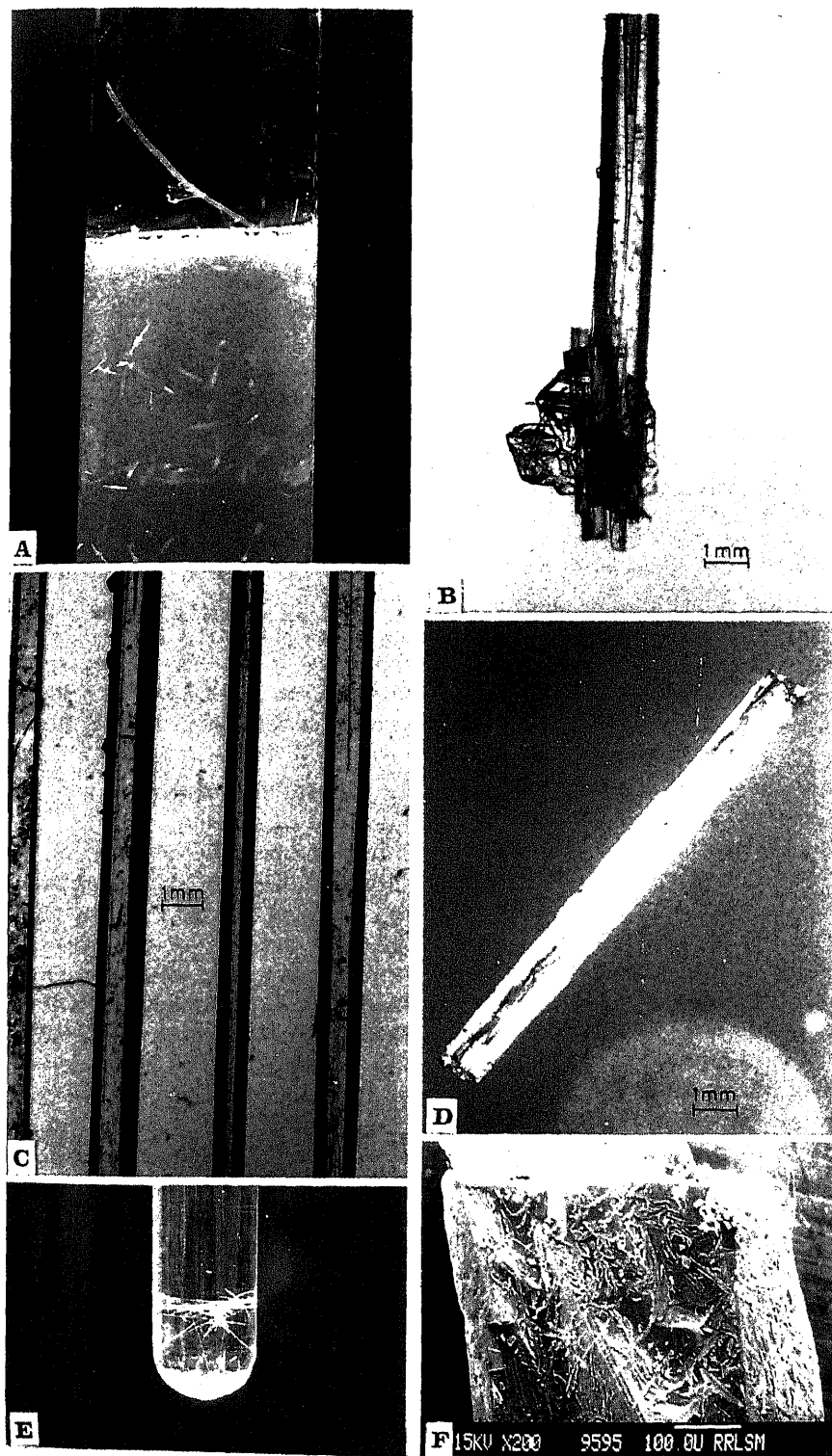
Figure 1. (A) Needles of anthraquinone seen growing in the supernatant solution kept over the gel, (B) a needle of anthraquinone grown from a cluster of anthracene crystals, (C) micrograph of needles obtained under crossed nicol prism, (D) a single crystal of anthraquinone photographed in straight extinction position with nicol in

et al 1986). However, in the present study, crystals were formed only in the top solution of particular pH (~ 6), irrespective of the gel pH. Hence, pH of top solution and in turn pH of the gel should have some effect on the nucleation of anthraquinone. Crystals of anthraquinone were found to grow in all pH values tried (5, 5·5, 6, 6·5, 7 and 7·5). But, better yield was obtained in 5–6 range. Most favourable pH was 5·5 in which yellow needles were found to grow into the gel medium in addition to that in the top solution. The rate of growth of these needles were studied. A uniform increase in the growth rate of needles into the gel medium was observed up to six days. After one week, the crystals attained maximum size, with a lower growth rate. This was followed by dissolution of crystals and the size of crystals fluctuates as shown in figure 2.

The samples kept in darkness did not yield yellow crystals of anthraquinone, but only platy crystals of anthracene. This confirms that the yellow needles of anthraquinone were produced by the photoreaction of anthracene as reported earlier (Corey and Taylor 1964).

By the irradiation of anthracene in acetone, anthraquinone is obtained as a final product as represented by the following conversion (figure 3).

Investigation on the solvent (acetone) incorporated over the gel in this experiment revealed that there was a gradual increase in the density, surface tension and conductance of the solvent. Hence, it can be presumed that such changes might have modified the anthracene solution favourably for being converted into anthraquinone by photoreaction. Density measurement of solvent and solution (table 1) showed that the supernatant solution of anthracene undergoes a change similar to the behaviour of acetone–water mixture. Thus the supernatant solution might have been tuned for the growth of yellow needles. The differences in growth of anthraquinone in pure gel and acetone mixed gel is also noted. When the solution was kept over pure gel, the changes in supernatant solution was fast and resulted in the nucleation and growth of large number of anthracene crystals. Solution over the acetone-mixed gel was found to undergo a slow change in parameters and few anthracene crystals were
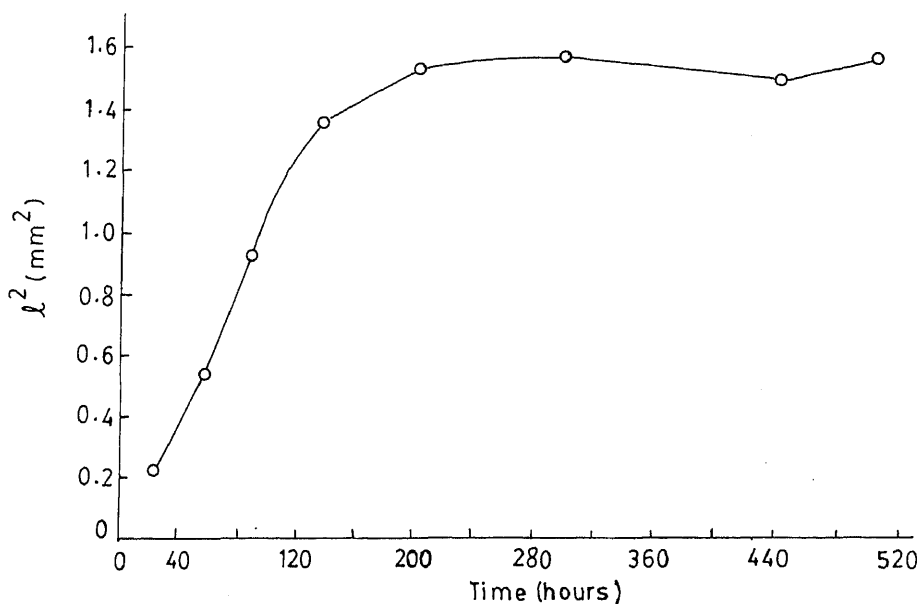

Figure 2. Growth kinetics of anthraquinone crystal.

Anthracene   Anthracene peroxide   Anthraquinone
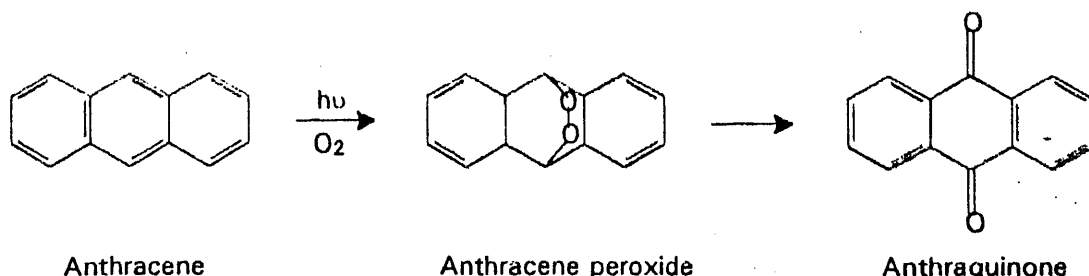
photoreaction and growth of anthraquinone.

In order to have better understanding of the role played by water–acetone system, water was mixed with acetone in different proportions. This mixture was used to prepare anthracene solution so as to grow crystals by slow evaporation without the aid of gel. A notable observation was that yellow needles of anthraquinone were formed in acetone–water system only if a seed was added. Good yield (figure 1E) was obtained when the mixture containing 5–30% of water was kept in an illuminated room. The crystals were separated, washed, dried and characterized with X-ray powder diffraction, IR, UV-visible spectroscopy, optical and scanning electron microscopy.

Table 1. Density of solvent/solution at 30°C.

Solvent/solution	Density (g cm^{-3})
Pure acetone	0·753
Acetone kept over the gel for one week	0·895
Saturated solution of anthracene in acetone	0·764
Top solution in which anthraquinone is formed	0·847

Yellow needles grown in acetone solution kept over the acetone mixed gel (cm^{-1})	Yellow needles grown in acetone–water mixture by solution growth (cm^{-1})	Assignments
937	935	CH out of plane bending
810	810	
621		Skeletal deform
694	690	Ring breathing
1170	1160	CH in plane bending
1284	1280	
1304	1330	Ring stretching
1332	1470	
1473	1560	
1522	1620	
1635		
1591	1580	Aromatic vibrations of quinones
1653	1678	C=O stretch of quinones
1676		
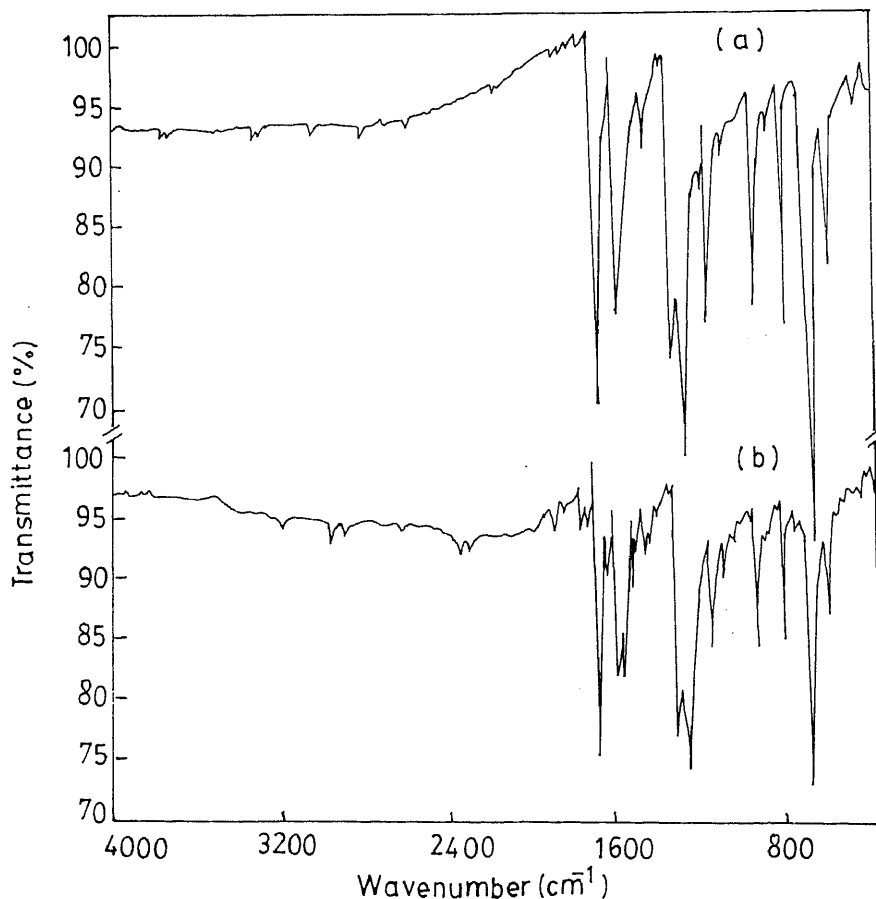
Figure 4. Infrared spectrum of anthraquinone needles grown (a) in acetone solution incorporated over acetone mixed gel and (b) in acetone–water solution.

Characterization

.1 *Optical and scanning electron microscopy*

Optical micrographs of the single crystals of anthraquinone were taken using 'LEITZ ORTHLUX II POL BK' petrological microscope. Figure 1B shows a needle of anthraqui-none nucleated from anthracene crystal substrate. Hollow cavity of the anthraquinone is also seen in the crystal. Figure 1C gives the micrograph of certain needles of anthraquinone obtained under crossed nicol position. A single crystal of anthraquinone photographed in straight extinction position with nicol in 45° for maximum illu-
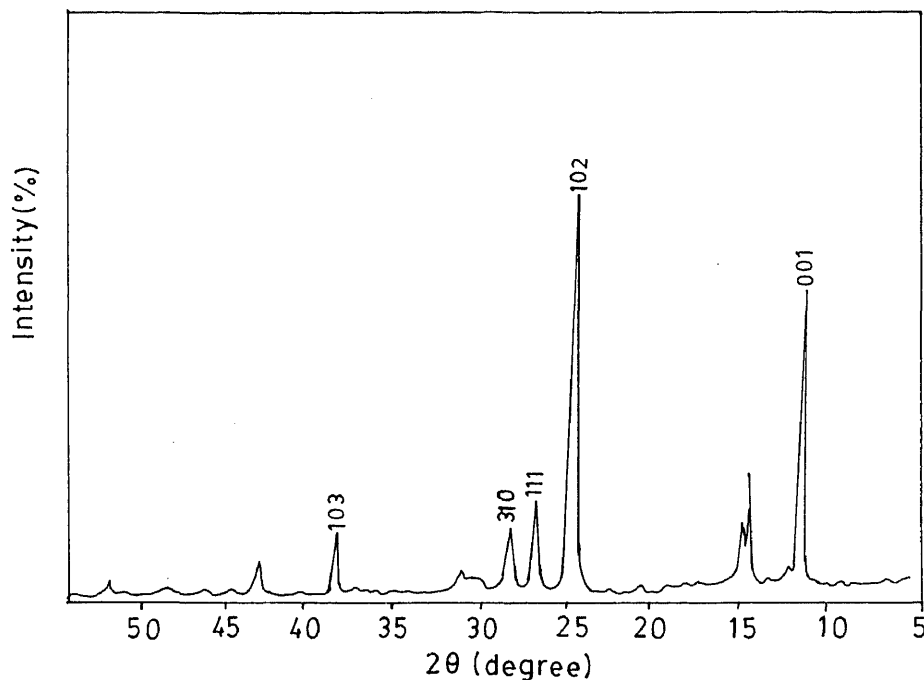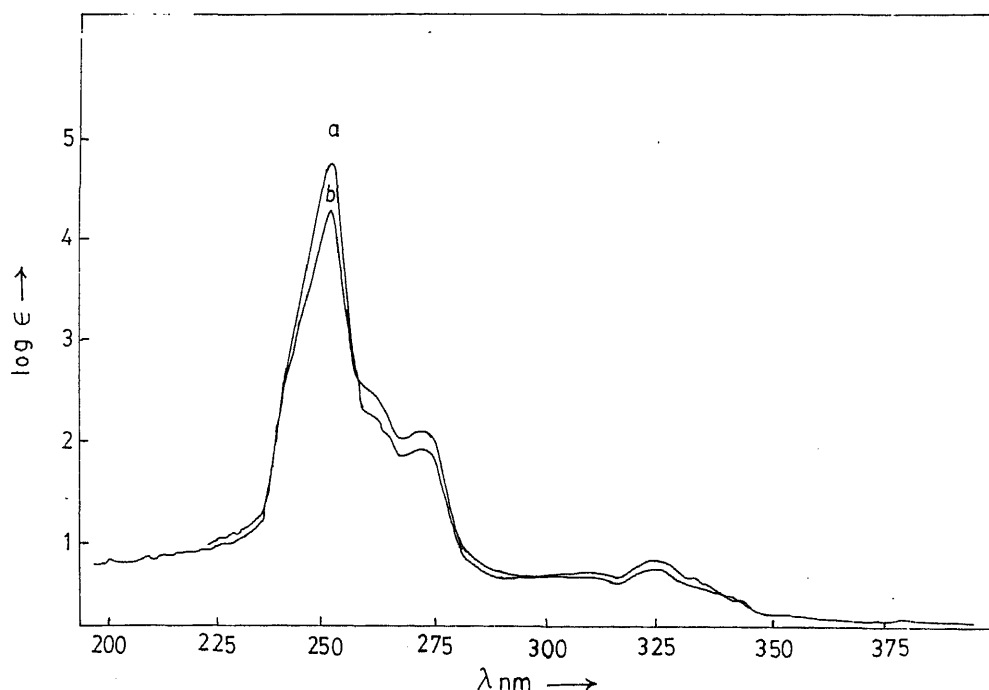

Figure 5. XRD pattern of anthraquinone crystals.

mination is given in figure 1D. Yellow needles of anthraquinone crystals grown in the supernatant solution kept over the gel is shown in figure 1A. Figure 1E shows the growth of large number of yellow needles in acetone–water solution of anthracene. The transparent tiny crystals at the bottom of the test tube are anthracene. Figure 1F gives the SEM picture of an anthraquinone needle.

4.2 *Infrared analysis*

The infrared spectra of the crystals were recorded in the range 4000–400 cm^{-1} by KBr pellet method. Preliminary analysis of the transparent crystals formed on the top solution by IR spectroscopy has confirmed that the crystals are anthracene. The IR spectrum of yellow needles grown in acetone solution and those grown in acetone–water mixture are given in figures 4A and B, respectively. The vibrational frequencies and their assignments are given in table 2. The intense bands at 1676 and 1653 cm^{-1} can be assigned to the carbonyl grouping not present in anthracene but seen in the case of anthraquinone (Singh and Singh 1968). The intense band at 694 cm^{-1} is identical to the ring breathing frequency reported for anthraquinone (Singh 1991).

4.3 *X-ray diffraction analysis*

The XRD scan of the crystals with CuK$_\alpha$ radiation in the 2θ range 0–50° is shown in figure 5. The calculated '*d*' values (0·360, 0·762 and 0·314 nm) are found to be in close agreement with the ASTM '*d*' values (0·352, 0·769 and 0·314 nm) of anthraquinone.

4.4 *Ultraviolet and visible spectroscopy*

UV-visible spectra of the anthraquinone crystals grown in this study were recorded using a SHIMADZU UV-2100S, UV-visible recording spectrometer. The UV-spectrum of the anthraquinone crystals dissolved in chloroform is displayed in figure 6. Very strong band at 253 nm and the medium intense band at 273 nm are in agreement with reported values (Morton and Earlam 1941).

5. Conclusion

Formation of anthraquinone crystals was observed during the growth studies of anthracene. For all the pH values (5–7·5) tried, crystals of anthraquinone were obtained with varying nucleation time and quality. Better crystals of anthraquinone were obtained in 0·5% (w/v) solution of anthracene kept over acetone-mixed gels of pH 5, 5·5 and 6. Growth of needles into the gel medium was observed for pH 5·5. At higher concentration (1% w/v), nucleation and growth of anthracene occurred hindering photoreactive conversion to anthraquinone. Acetone mixed gel was found to be a better medium in aiding the growth of anthraquinone rather than the pure gel. Solution studies have revealed that acetone–water mixture can also be used as a solvent for growing anthraquinone crystals by photo reaction.

References

Chung R H 1978 *Encyl. Chem. Technol.* **2** 700
Corey E J and Taylor W C 1964 *J. Chem. Soc.* **86** 3881
Das C K and Nikhilendu S 1982 *J. Chem. Technol. Biotech.* **32** 643
Grozev G, Anastasov A, Peshev K and Elenkov D 1976 *Insv. Khim.* **9** 681
Ivan M R and William A W 1949 *J. Chem. Soc.* **30** 602
Louis F F and Mary F 1960 *Organic chemistry* (New York: Reinhold Publishing Company) p. 760
Malik M and Dohnal J 1990 *Czech Cs* 241
Margaret C E, Donald A J and Brain S D 1986 *J. Cryst. Growth* **76** 645
Mizoguchi A and Venishi N 1991 *Jpn. Kokai Tokyo Koho* 5
Morton R A and Earlam W T 1941 *J. Chem. Soc. Part I* 159
Noboru S *et al* 1969 *J. Chem. Soc. Jap.* **42** 1377
Owens H W 1958 *Can. J. Chem.* **36** 949
Pielichiouski J, Gurlat P and Polaczck J 1992 *Fridges Kohle Togunsber* 155
Rajendra Babu K, Deepa M, Nair C M K and Vaidyan V K 1998 *Cryst. Res. Technol.* (in press)
Singh S N 1991 *Indian J. Pure & Appl. Phys.* **28** 211
Singh S N and Singh R S 1968 *Spectrochim Acta* **A&B24** 1591
Yao O D 1962 *UKR Fiz. Zh.* **7** 315

Growth of undoped and Te doped InSb crystals by vertical directional solidification technique

D B GADKARI*, K B LAL[+] and B M ARORA[‡]

Department of Physics, Mithibai College, Mumbai 400 056, India
[+]Department of Physics, University of Bombay, Mumbai 400 098, India
[‡]SSE Group, Tata Institute of Fundamental Research, Mumbai 400 005, India

Abstract. We have successfully grown high mobility undoped and Te doped InSb crystals of size 10–12 mm dia. and 60 mm length under inert argon atmosphere in closed quartz ampoules, by vertical directional solidification (VDS) technique. The crystals showed predominantly (220) orientation along the growth axis. The surface defects, such as voids were reduced drastically by selecting proper lowering rate, rotational speed and cone angle of the ampoule. The high mobility and quality crystals were obtained with the ampoule conical angle less than 20°, lowering rate 5 mm/h, and rotational speed 10 rpm.

Keywords. InSb crystals; directional solidification; quartz ampoule; cone angle; Hall measurement; inert atmosphere.

1. Introduction

InSb crystals are useful for infrared detectors in 3–5 μm wavelength range (Chen *et al* 1992). This material is also of increasing interest for large area detector arrays (Rayners *et al* 1993), high speed devices (Asauskas 1980) and optoelectronics devices (Baranski 1990). For epitaxial growth of InAsSb on InSb (Eagen *et al* 1994), substrates of high quality are required (Ohaski 1986; Lee *et al* 1993; Michel *et al* 1994). There have been reports of InSb bulk crystal growth using methods such as Czochralski (Witt *et al* 1968; Lin and Kou 1995), Bridgman (Kim 1978; Mulski and Neumann 1982), zone refining (Garanuet *et al* 1995), vertical gradient (Strauss 1959; Potard 1981; Jung *et al* 1991) and centrifuge (Weber *et al* 1990; Derabail and Wilcox 1992; Zhou *et al* 1993). We have undertaken the growth of undoped and doped bulk InSb crystals by vertical directional solidification (VDS) technique in conical quartz ampoule without using any seed. The VDS is a simple and suitable method for obtaining good quality InSb single crystals. To reduce the Sb loss related problem, the growth is done in closed ampoule and under optimization of inert atmosphere of argon. This paper reports the details of experiments carried out under various growth conditions such as cone angle of ampoule, lowering rate, rotation speed and inert gas for high quality single crystal growth without seed. As grown crystals are *p*-type while Te has been used for growing *n*-type doped crystals.

2. Experimental

2.1 *Crystal growth*

We performed the growth of InSb crystals in a vertical growth system by directional solidification (VDS) (Gadkari *et al* 1994). The system consists (see figure 1) of a vertical single zone resistance furnace. Quartz tube of 10 cm dia. and 100 cm length was used as the growth chamber. The tube was closed at both ends by end caps with Wilson seal arrangements for gas inlet and outlet. Water circulation was used for cooling the seals. Thermocouple (Cr–Al) was inserted from the bottom end of quartz tube for measurement of temperature inside the growth chamber. High purity In (6 N), Sb (6 N) and Te (6 N) were used as source materials. 9·7 g In and 10·3 g Sb in stoichiometric composition were filled in quartz ampoule of 10–12 mm in dia. and 100 mm in length with conical end on one side. Ampoules of various cone angles ranging from 15–70° were used in the growth experiments. Initially, growth was tried in open ampoule with flowing N_2 atmosphere. However, the resulting crystal was of poor quality. Subsequently growth was done in sealed ampoule and two variations of the procedure were used. In one case, the ampoule was sealed in vacuum and in the second case the ampoule was backfilled with argon before sealing. Growth of doped crystals was done by mixing Te dopant in the charge before sealing the ampoule for the directional

perature to 800°C. This temperature was maintained for 10 h for synthesis and homogeneous mixing of the source materials. For the growth, the ampoule was lowered to the gradient zone of the furnace where the temperature was in the range 575–650°C and kept in this zone for 10 h for prolonged heating for thermal stabilization in the melt prior to starting the growth. The growth was done by further lowering the ampoule in the gradient zone. Different lowering rates in the range 5–10 mm/h were used. Further the rotation speed was varied in the range 10–30 rpm. After completion of the growth, the InSb ingot was annealed at a constant temperature of 200°C for about 18–24 h prior to its removal from the growth chamber. The typical growth profile is shown in figure 2. In good quality growth, the ingot can be removed from the quartz ampoule easily showing that the melt does not stick to the wall of the ampoule. As such the diameter of the grown ingot is slightly smaller than the internal diameter of the ampoule.

2.2 Sample characterization

Substrates of thickness about 500 μm were cut perpendicular to the growth axis. These wafers were cleaned and lapped by 5 μm carborundum powder. Further polishing of the wafers was done mechanically by using 0·3 and 0·05 μm alumina abrasive to mirror finish. We tried also chemi-mechanical polishing using 5% bromine–methanol solution and similar results were observed. Wafers were cleaned in warm TCE, acetone and methanol of electronic grade. These wafers were then used for various characterizations e.g. (i) the X-ray diffraction

recorded with step angle 0·02° and 0·5 s step time on JEOL JDX-8030 for 35 KV and 25 mA, (ii) growth morphology, and (iii) electrical transport properties by Hall measurements (Van der Pauw 1958; Look 1990). The EDAX measurements were used to identify the composition in the defect regions.

3. Results and discussion

3.1 Unsealed ampoule

Early growth experiments were performed in unsealed ampoules in flowing N_2. Ingots were grown by using ampoules with 4 different cone angles from 50°–70°. In all cases, growth showed severe distribution of voids on the surfaces. The XRD pattern of the InSb substrates cut from these ingots showed large FWHM for XRD peaks (see table 1), indicating large heterogeneities and grain boundaries which may be due to polycrystalline growth.

3.2 Sealed ampoule

Since the open ampoule growth was of poor quality, the growths were carried out in ampoule with cone angle less than 30°. The source materials In and Sb inside ampoules were alternately evacuated and flushed with argon 10 times prior to vacuum sealing (10^{-5} torr), and growth was carried out at lowering rate 10 mm/h and rotation speed 30 rpm. Ingots were void free, 10 mm dia. and 60 mm length (figure 3). XRD measurements
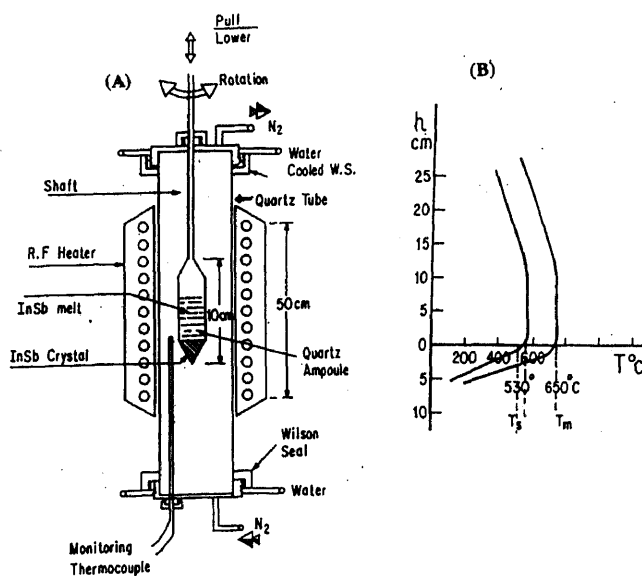
Figure 1. A. Schematic diagram of the growth system and B. temperature profile of the furnace.
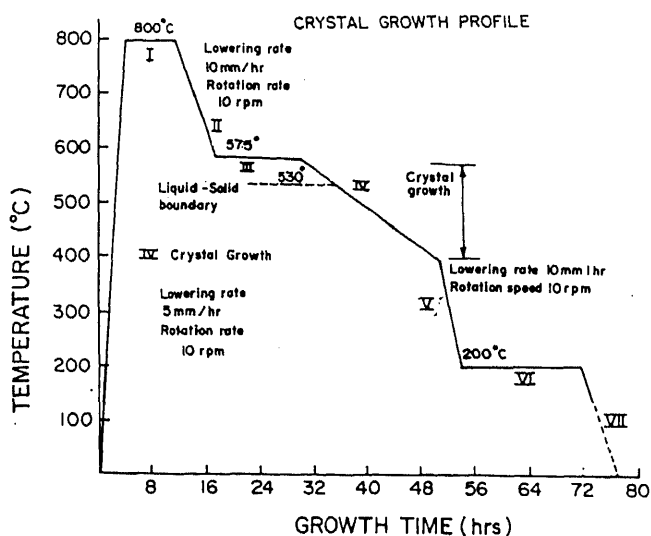
Figure 2. The crystal growth temperature versus time graph after optimizing growth conditions. The temperature is specified at the conical tip of the ampoule.

Table 1. Cone angles of ampoules and Hall measurements at 300 K.

| Growth no.	Crystal	Ampoule ambient	Cone angle	Semicond. type	Mobility $(cm^2/V.sec)$	RH $(cm^3/coulomb)$	FWHM (220) (arcsec)
3	InSb p3	A	64	p	–	–	1140
4	InSb p4	A	60	p	–	–	1290
5	InSb p5	A	50	p	–	–	1780
6	InSb p6	A	54	p	–	–	1740
7	InSb p7	B	30	p	–	–	1680
8	InSb p-1	C	25	p	3900	−39·6	580
9	InSb p-R	C	22	p	3500	−41·5	560
10	InSb n-1	C	25	n	3400	−0·35	482
11	InSb n-R	C	25	n	3145	−0·49	455
12	InSb p2-4	D	18	p	42000	−143·0	285
13	InSb n2-4	D	16	n	27000	−10·6	260
12	InSb p2-12	D	18	p	55000	−165	255
13	InSb n2-12	D	16	n	25600	−11·5	235

A, Open ampoule flowing N_2 ; B, ampoule closed in vacuum (10^{-5} torr) without argon flushing; C, ampoule prior to vacuum sealing (10^{-5} torr) was flushed by argon; D, ampoule closed under argon pressure (100 torr). Measurements were taken on two samples of growth nos 12 and 13 from different places.
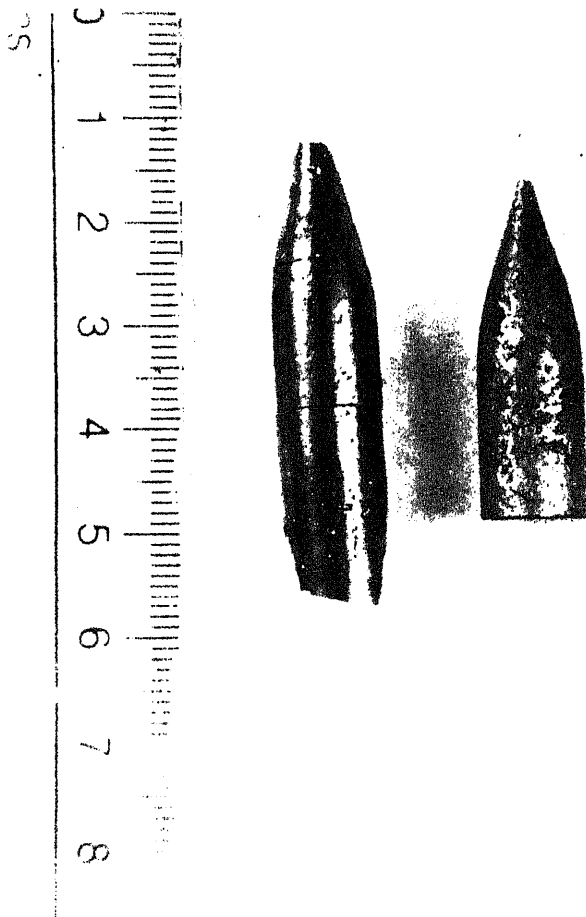
Figure 3. The growth of undoped ingots performed by sealing the ampoules in vacuum (growth nos 8–9).
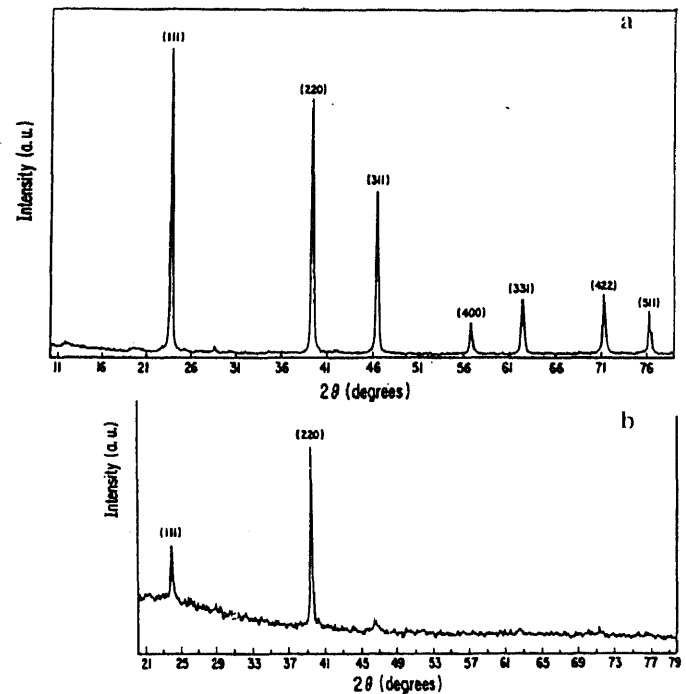
Figure 4. **a**. XRD pattern of the powder crushed from grown InSb ingots and **b**. XRD pattern of a substrate cut perpendicular to the growth axis.

data 1994) (see figure 4a). Wafers prepared from the ingots showed prominent reflection for (220) orientation (see figure 4b). Sharp peaks of the XRD (table 1) showed improved crystallinity of the InSb ingots. Etching of polished wafers revealed regions rich in Sb as probed by EDAX. The etching of the undoped InSb substrate

the walls of the ampoules. Ingots surface were observed to be more shiny in conical region than the cylindrical regions as seen in figure 5.

X-ray diffraction measurements on the wafers cut from these ingots showed prominent (220) reflection and excellent agreement with the ASM data mentioned earlier. Further as seen from table 1, the FWHM had improved further as compared to the growth done in the evacuated ampoule. Improvement in the quality of the crystal grown under argon atmosphere was also seen from the Hall measurements. Undoped crystals were p-type with mobility reaching a value 55000 cm^2/V.sec at room temperature. The low (20 K) temperature Hall measurement on this sample showed doping concentration ($\sim 1 \times 10^{16}$ cm^{-3}) which shows reduction in the background defects by using this procedure. The Te doped materials are also of better quality and show significant increase in mobility from 26000 cm^2/V.sec at room temperature to 29000 cm^2/V.sec at 40 K with the donor concentration of 6×10^{17} cm^{-3}.

4. Conclusions

Nearly perfect single bulk crystal of InSb of high quality and degree of crystallinity have been grown from the melt by the VDS technique. Our experiments show the following.

(I) The wafers cut from the ingots show prominent (220) reflection indicating growth of nearly single crystal without seed.

(II) Maintaining inert argon atmosphere in the closed quartz ampoule is very crucial for growing high mobility InSb crystals. Other optimized growth parameters are (i) ampoule lowering rate 5 mm/h, (ii) rotation speed 10 rpm and (iii) conical angle less than 20°. Good quality ingots of 10–12 mm dia., 60 mm in length and 20 g weight have been grown by VDS technique in closed quartz ampoule.

(III) Undoped InSb is p-type. A very high Hall mobility ~ 55000 cm^2/V.sec has been achieved in the optimized growth.

(IV) Te doped n-type material with doping concentration 6×10^{17} cm^{-3} and Hall mobility 26000 cm^2/V.sec at 300 K have been grown.

These results indicate the effectiveness of vertical directional solidification method for the growth of high quality, uniform internal structure and high mobility InSb bulk crystals.

Figure 5. Magnified photograph of Te doped ingots with substrates (growth no. 13).

substrates (Gadkari *et al* 1995) showed absence of eutectic features but defects like striations, band formation, microcracks and precipitate were observed.

Hall–Van der Pauw measurements, the undoped and Te doped samples at 300 K showed low mobility of 3900 cm^2/V.sec and 3400 cm^2/V.sec respectively. From these observations we concluded that the crystals contained excessive defects. In order to overcome this problem, we did next series of experiments in ampoules closed under Ar pressure.

3.3 *Sealed ampoules with inert atmosphere*

In this modified procedure, the source materials were at first evacuated and flushed with argon 10 times. Finally, the ampoule was backfilled with argon at 100 torr and sealed. All the ampoules used in the experiments had cone angle less than 20°, and growth was done at lowering rate of 5 mm/h and rotational speed 10 rpm. As grown ingots were free from voids (figure 5) with

Acknowledgements

References

Asauskas R, Dobro Volskis and Krotkus A 1980 *Sov. Phys. Semicond.* **14** 1377

Baranski P I, Gorodnichi O P and Shevchenko V V 1990 *Infrared Phys.* **30** 59

Byueng-Su Yoo, Mark A McKec, Sang -Gi Kim and El-Hang Lee 1993 *Solid State Commun.* **88** 447

Chen L P, Lou J J, Liu T H, Pang Y M and Yang S J 1992 *Solid State Electron.* **35** 1081

Derabail R and Wilcox W R 1992 *J. Cryst. Growth* **119** 98

Eagen R J *et al* 1994 *Semicond. Sci. Technol.* **9** 1591

Gadkari D B, Lal K B and Arora B M 1994 *Solid State Phys. (India)* **C37** 198; *DAE Symp.* (Jaipur: Rajasthan Univ)

Gadkari D B, Lal K B, Singh A J and Arora B M 1995 *Proc. VI national seminar on crystal growth* (Madras: Anna Univ.) p. 34

Gadkari D B, Lal K B, Shah A P and Arora B M 1995 *Solid State Phys. (India)* **C38** 148; *DAE Symp.* (Calcutta: ACS)

Garanuet J P, Differ T and Favier J J 1990 *J. Cryst. Growth* **106** 426

International Centre for Diffraction Data 1994 Card No. 6-208, p. 327; NBS circular 539 (1955) p. 73

Jung Y J, Park M K, Tae S I, Lee K H and Lee H J 1991 *J. Appl. Phys.* **69** 3109

Kim K M 1978 *J. Cryst. Growth* **44** 413

Lee G S, Thomson P E, Davis J L, Omaggio M K and Schidtt W A 1993 *Solid State Electron.* **36** 387

Lin M H and Kou S 1995 *J. Cryst. Growth* **152** 256

Look D C 1990 *J. Electrochem. Soc.* **137** 260

Michel E, Singh G, Slivkeen S, Besikci C and Bove P 1994 *Appl. Phys. Lett.* **65** 3338

Moorwood A F 1993 *SPIE Int. Soc. Opt. Eng.* **1946** 461

Mulski G and Neumann G 1982 *J. Cryst. Growth* **59** 548

Ohaski T 1986 *J. Vac. Sci. Technol.* **B4** 622

Potard C 1981 *J. Cryst. Growth* **54** 558

Rayners J *et al* 1993 *SPIE Int. Soc. Opt. Eng.* **1946** 490

Straus A J 1959 *J. Appl. Phys.* **30** 559

Van der Pauw L J 1958 Philips Res. Report 13, pp 1–9

Witt A F and Gatos H C 1968 *J. Electrochem. Soc.* **115** 70

Weber W, Neumann G and Muller G 1990 *J. Cryst. Growth* **100** 145

Zhou J L, Wilcox W R and Regel L L 1993 *J. Cryst. Growth* **128** 173

Studies on synthesis of calcium ferrite-based bio glass ceramics

B R JAGADISH, N PRABHU and D BAHADUR*

Department of Metallurgical Engineering and Materials Science, Indian Institute of Technology, Mumbai 400 076, India

Abstract. The possibility of synthesizing a Ca-ferrite based biocompatible glass ceramic has been explored in the following two glass compositions: (i) $28Na_2O$–$8CaO$–$3P_2O_5$–$11Fe_2O_3$–$50SiO_2$, and (ii) $25Na_2O$–$8CaO$–$3P_2O_5$–$20Fe_2O_3$–$41SiO_2$–$3B_2O_3$ (in weight ratio). The effect of simulated body fluid on the different glasses and glass ceramics was also investigated. While there is no direct evidence for apatite formation, the weight losses recorded and formation of a Si-rich layer at the surface appears to be an indication of onset of apatite formation. The rate of apatite formation is presumably retarded due to the presence of Al^{3+} (picked up from Al_2O_3 crucible). Ferromagnetic resonance experiments at 9·03 GHz demonstrate that these glass ceramics can possibly be used for microwave hyperthermia.

Keywords. Bio glass ceramics; calcium ferrite; hyperthermia; apatite.

1. Introduction

It has been shown that bioactive glasses and glass ceramics bond to bone (tissue) by the formation of an apatite layer on the surface (Anderson *et al* 1990; Hench 1991; Ochura *et al* 1994). The apatite phase is equivalent chemically and structurally to the mineral phase of the bone and it is this equivalence which is thought to be responsible for the interfacial bonding (Hench 1991). The formation of surface apatite layer has been investigated by dipping the bioactive glasses and glass ceramics in a simulated body fluid (SBF) (with ion concentrations similar to those in human blood plasma) or in a Tris buffer solution (TBS) (Anderson *et al* 1990; Ebisawa *et al* 1990, 1992a; Kokubo *et al* 1992; Li *et al* 1992; Ohtsuki *et al* 1992).

A promising application of bioactive ferrite-based glass ceramics is in the hyperthermia treatment of cancer. On application of either an alternating magnetic field or microwaves, the bioactive magnetic glass ceramic acts as a localized heating target which leads to selective dissipation of heat to the cancerous tissues. Ebisawa *et al* (1992b) have successfully demonstrated the use of a bioactive ferrimagnetic glass ceramic (in Fe_2O_3–SiO_2–CaO–B_2O_3–P_2O_5 system) as a thermoseed for hyperthermia of cancer using an alternating magnetic field (the soft heating method). Ferromagnetic resonance (FMR) has been used by Nikawa and Okada (1987) for deep heating of the cancerous tissue for microwave hyperthermia. It was found that the energy dissipation rate at the target during FMR was 40% higher than that of nonresonance

microwave heating. Also, the depth of heating increased by nearly 50% at resonance.

In the present study our objective was to synthesize Ca–ferrite-based glass ceramics through nucleation and growth in CaO–Na_2O–P_2O_5–P_2O_5–Fe_2O_3–SiO_2-based glass. We have further evaluated the bioactivity of the different glass ceramics *in vitro* (using a TBS or a SBF solution). The different glass ceramics have been characterized in detail before and after treating them in SBF/TBS solution. The suitability for use as thermoseeds in microwave hyperthermia has been demonstrated by FMR studies.

2. Experimental

Two glasses G1 and G2 (compositions given in table 1), were prepared using reagent grade chemicals Na_2CO_3, $CaCO_3$, $CaHPO_4 \cdot 2H_2O$, Fe_2O_3, SiO_2 and H_3BO_3. Melting was done in an alumina crucible and pouring of melts done at 1150°C and 1130°C respectively. The melt was splat quenched using two steel plates to obtain glass. XRD studies of powder samples were carried out on a Phillips PW480 diffractometer using CuK_α radiation in the scan range 20°–100°.

Differential thermal analysis (DTA) was performed on the powder samples using a Dupont model 9900 system, with heating rate of 10°C/min in the temperature range

Table 1. Glass composite in weight percentage.

	Na_2O	CaO	P_2O_5	Fe_2O_3	SiO_2	B_2O_3

20°C–1000°C. A typical DTA plot for glass (G1) is given in figure 1. The nucleation and growth temperatures were estimated from the DTA results and the glasses were accordingly subjected to different heat treatment schedules. The X-ray diffraction technique was used to determine the different phases that formed after heat treatment. Table 2 provides a list of various phases formed after different heat treatments.

TBS containing 50 mM Tris (hydroxymethyl) methyl-amine and 45 mM HCl was prepared as suggested by Anderson *et al* (1990) and Li *et al* (1992). Samples were dipped in 25 ml of TBS for a period of 30 days. SBF was prepared by dissolving reagent grade chemicals NaCl, NaHCO$_3$, KCl, MgCl$_2 \cdot$6H$_2$O, CaCl$_2 \cdot$2H$_2$O and CaHPO$_4 \cdot$2H$_2$O in distilled water. The solution was buff-ered by 50 mM Tris (hydroxymethyl) methylamine and 45 mM HCl (Ebisawa *et al* 1990, 1992a; Kokubo *et al* 1992; Ohtsuki *et al* 1992). Ion concentrations in SBF have been reported by Ohtsuki *et al* (1992). Samples were dipped in 50 ml of SBF each in stoppered standard flasks. In order to study modifications occurring at the surface, XRD studies were carried out on samples dipped in TBS and SBF. To study compositional changes occurring at the surface, energy dispersive X-ray (EDX) analysis was carried out on a few dipped and undipped

samples. Cambridge Stereoscan 90B system was used for scanning electron microscopy (SEM). Ferromagnetic resonance studies of samples were done on a system using microwave frequency 9·07 GHz in scan range 0–4000 Oe magnetic field.

3. Results and discussion

The as-quenched glasses G1 and G2 are amorphous. Figure 2 gives the X-ray diffraction patterns of the glass G1 and the glass ceramics GC11 and GC14. While the

Figure 1. A typical DTA plot for glass G1.
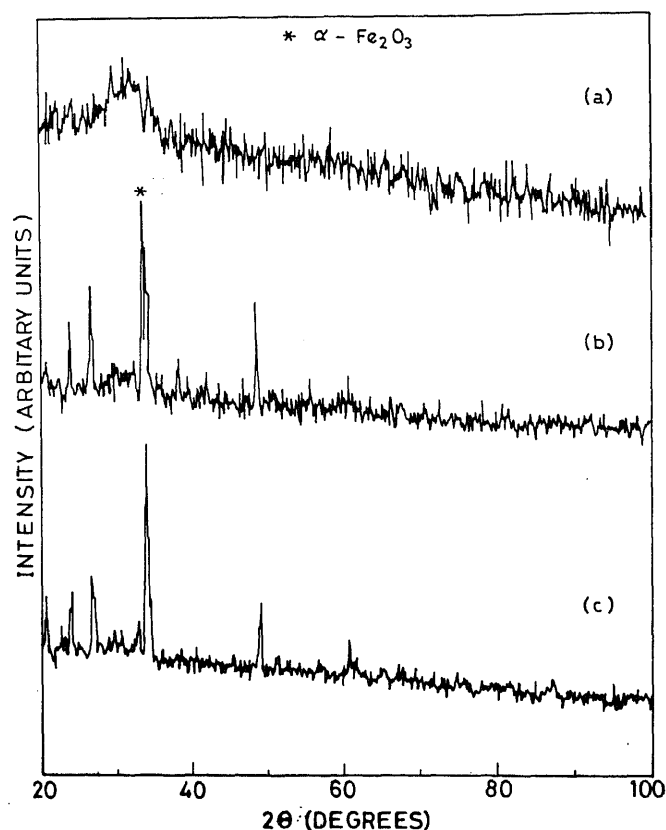
Figure 2. X-ray diffraction patterns of (a) glass G1, (b) GC11 and (c) GC14.

Table 2. Heat treatment, label and crystalline phases observed.

| Glass ceramic | Starting glass | Heat treatment | | Crystalline phases present |
		Nucleation	Growth	
GC11	G1	430°C/1 h	780°C/24 h	CaFe$_4$O$_7$, α-Fe$_2$O$_3$ (MR)
GC12	G1	730°C/1 h	780°C/24 h	CaFe$_4$O$_7$, α-Fe$_2$O$_3$ (MJ)
GC13	G1	430°C/1 h	740°C/24 h	CaFe$_4$O$_7$
GC14	G1	430°C/1 h	780°C/48 h	CaFe$_4$O$_7$
GC21	G2	475°C/1 h	690°C/24 h	CaFe$_4$O$_7$, α-Fe$_2$O$_3$ (MJ)
GC22	G2	570°C/1 h	883°C/24 h	CaFe$_4$O$_7$, α-Fe$_2$O$_3$ (MR)

phase. But, when the growth time is increased from 24 h to 48 h, as in the sample GC 14, a single $CaFe_4O_7$ ferrite phase is obtained. It is possible that with increase in growth time α-Fe_2O_3 reacts with CaO in matrix phase by the following reaction:

$$CaO + 2Fe_2O_3 \rightarrow CaFe_4O_7 .$$
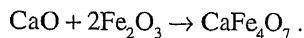
Based on the results shown in table 2 we have observed that when the nucleation temperature is increased from 430°C to 730°C as in GC12 sample, a higher relative amount of α-Fe_2O_3 is obtained. This suggests that 430°C is the right nucleation temperature for Ca-ferrite phase,
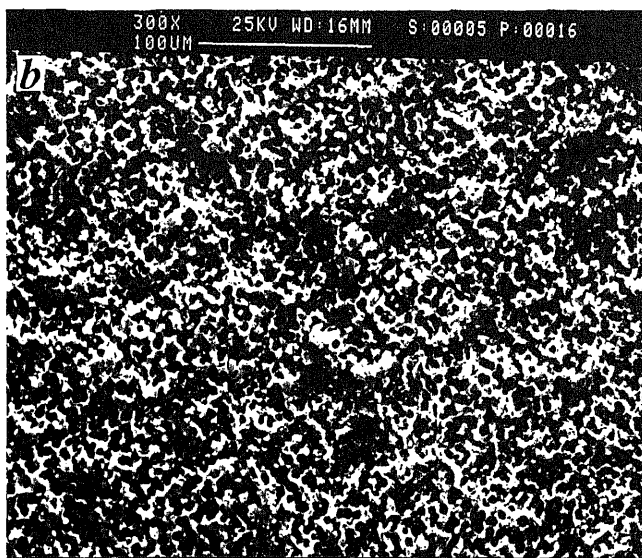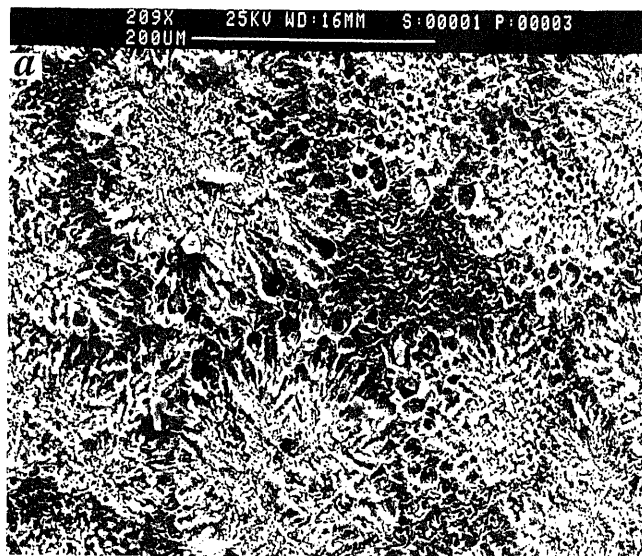
was decreased to 740°C from 780°C as in GC13 sample, a single $CaFe_4O_7$ phase was obtained with low glassy background. This indicates that 740°C is an optimum growth temperature for $CaFe_4O_7$ phase. The GC21 and GC22 samples show both the crystalline phases i.e. $CaFe_4O_7$ and α-Fe_2O_3. The relative amount of α-Fe_2O_3 phase is greater in GC21 than in GC22 sample.

These results from X-ray diffraction studies are supported by scanning electron micrographs. It can be seen for sample GC12 in figure 3a, that there is a distinct tendency for the second phase to separate as non spherical structure with high connectivity and dendritic growth. There is also a clear evidence for the existence of two phases in the sample GC21 as seen from figure 3b. The heat treatment process presumably allows enough time for glass in glass phase separation followed by crystallization of $CaFe_4O_7$ and α-Fe_2O_3.

Weight losses were recorded after dipping the glass and glass ceramic samples either in TBS or SBF solution for varying duration. Table 3 gives the weight losses in mg/g for the different samples. From this table it can be seen that glass suffers a weight loss of 1–2 orders of magnitude less than that suffered by the glass ceramics. This is in accordance with the results published in literature which suggest that presence of Fe_2O_3 in a glass improves its stability (Ochura *et al* 1994). On heat treatment, Fe_2O_3 presumably enters the crystalline phase, and the residual glassy phase becomes less stable.

For GC11, GC12 and GC13, the weight loss increases with increasing degree of crystallinity (weight loss by GC13 > GC11 > GC12). This indicates that greater the extent to which crystallization occurs, the better is the removal of Fe_2O_3 from glassy phase and hence more unstable is the glassy phase.

Figure 4 gives the X-ray diffraction patterns of some typical samples GC21, GC21D, GC11D and GC13D. The dipped samples are represented by adding letter D in their label. XRD patterns of samples dipped in TBS/SBF reveal formation of an amorphous surface layer

Figure 3. Scanning electron micrographs of glass ceramic samples **a**. GC12 and **b**. GC21.

Table 3. The weight losses for different samples.

Sample	Weight loss (mg/g)	
	In TBS after 30 days	In SBF after 8 days
G1	0·344	–
G2	–	1·04
GC11	26·42	–
GC12	19·84	24·86
GC13	30·19	12·92
GC14	16·19	–
GC21	–	15·49
GC22	–	25·97
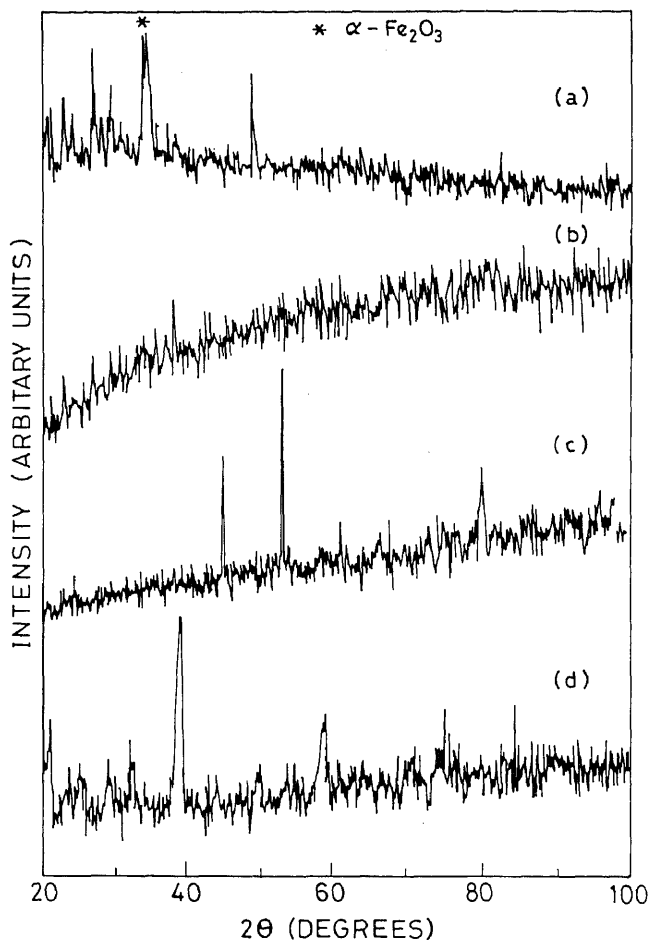
Figure 4. Typical X-ray diffraction patterns of samples (a) GC21, (b) GC21D, (c) GC11D and (d) GC13D. D refers to samples dipped in TBS/SBF.

in some cases (i.e. GC12D, GC14D, GC21D, GC22D). On the other hand, there is formation of a crystalline surface layer as in the sample GC11D. The sample GC13D, however remains essentially unmodified except small shift in d values. The crystalline surface layer on GC11D could not be identified.

Modification of the surface is observed only in cases where an appreciable amount of glassy phase is present (as in GC11, GC12 and GC14). When crystallization has proceeded to a large extent as in GC13, we see no surface modification. This seems to be in agreement with Li *et al* (1992), who showed that residual glassy phase in a glass ceramic is responsible for the surface
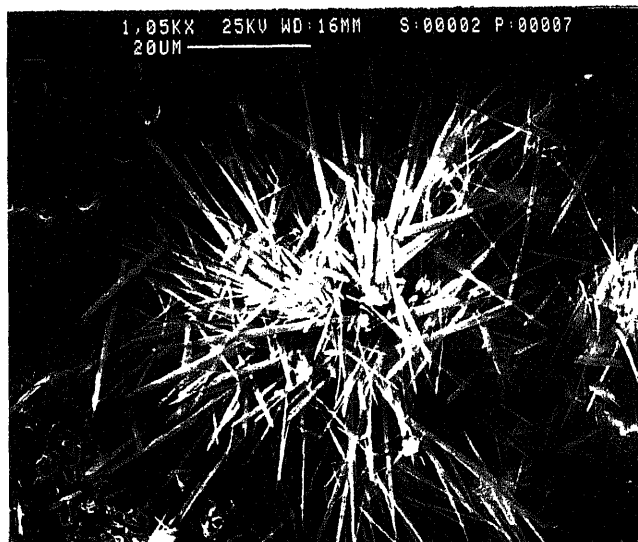
Figure 5. Scanning electron micrograph of sample GC11D.
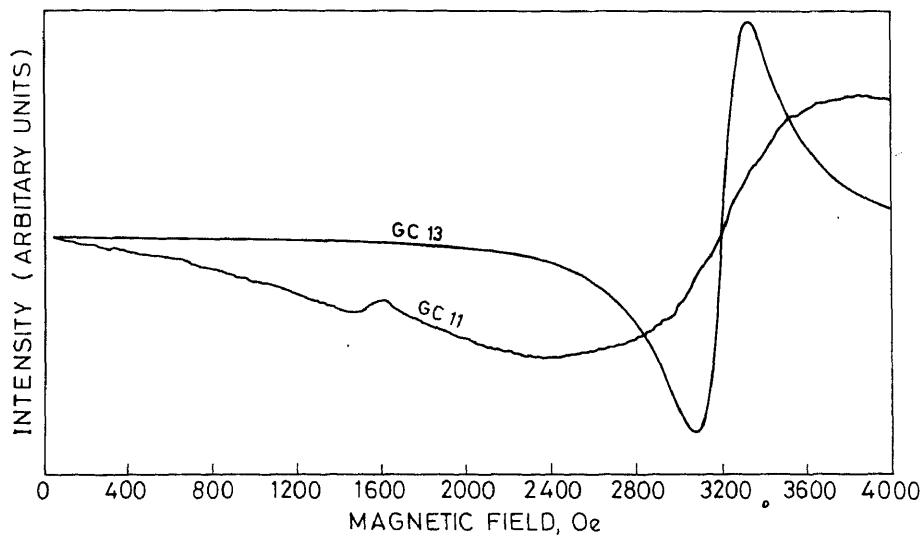
modification and an apatite layer formation. Their results show that bioactivity is lost when residual glassy phase is less than 5 wt%. Glass G1 which showed negligible weight loss, shows no surface modification.

Since we could not identify the crystalline phase developed at the surface of GC11D, we attempted to probe the composition of the surface of dipped and undipped samples of GC11 by EDX. These results indicated that the concentration of sodium on the surface decreases from 22·3% to 1·43% on dipping, while the concentration of Si in the surface increases from 48·5% to 66·3% on dipping. According to Hench (1991), Na depletion at the surface along with the formation of a Si-rich layer, is the first step in the formation of an apatite layer on the surface of bioactive glasses and glass ceramics. EDX analysis shows the presence of aluminium picked up from the alumina crucible. It seems to have occurred during preparation of the glass. Earlier work (Anderson *et al* 1990; Kokubo *et al* 1992; Ohtsuki *et al* 1992; Ochura *et al* 1994), have shown that presence of Al retards bioactivity. Anderson *et al* (1990) suggest that presence of Al in the silica-rich layer retards the formation rate of apatite layer and also stabilizes the glass, thus preventing formation of a $CaO-P_2O_5$-rich film on top of the Si-rich layer. This could be the reason why only a Si-rich or an amorphous layer is observed in our case without formation of an apatite layer. SEM micrographs of the sample GC11D shown in figure 5, exhibits fibrous crystals which appear oriented perpendicular to outer surface. Presumably, the apatite starts nucleating and growing from these silica-rich fibrous grains (Ebisawa *et al* 1992b).

A ferromagnetic resonance experiment at 9·07 GHz and magnetic field up to 4000 Oe was done on a few samples just to demonstrate absorption of microwave power by the sample. We get broad resonance for GC13 as shown in figure 6. GC11 shows much broader and two resonances at fields of 1540 and 3100 Oe. The evidence of absorption of microwave power and the resonance indicates that these glass ceramics can possibly be exploited for microwave hyperthermia using ferromagnetic resonance.

We have explored the formation of bioactive ferrite-based glass ceramics in $Na_2O-CaO-P_2O_5-SiO_2-Fe_2O_3$-based system and examined the possibility of apatite formation on the surfaces of glass ceramics in SBF/TBS solution. Further, absorption of microwave power has been demonstrated through ferromagnetic resonance.

Acknowledgement

References

Anderson O H, Liu G, Karlsson K H, Niemi L N, Miettinen J and Juhanoja J 1990 *J. Mater. Sci.: Mater. Med.* **1** 219

Ebisawa Y, Kokubo T, Ohura K and Yamamuro T 1990 *J. Mater. Sci.: Mater. Med.* **1** 239

Ebisawa Y, Kokubo T, Ohura K and Yamamuro T 1992a *J. Mater. Sci.: Mater. Med.* **4** 225

Ebisawa Y, Murashita T, Kokubo T, Ohura K, Ikenaga M, Yamamuro T, Hiraoka M and Abe M 1992b *Proc. of the sixth int. conf. on ferrites (ICF6), Japan* (Japan: Society for Powder and Powder Metallurgy) p. 287

Hench L L 1991 *J. Am. Ceram. Soc.* **74** 1487

Kokubo T, Kishitani H, Ohtsuki C, Sakka S and Yamamuro T 1992 *J. Mater. Sci.: Mater. Med.* **3** 79

Li P, Yang Q, Zhang F and Kokubo T 1992 *J. Mater. Sci.: Mater. Med.* **3** 452

Nikawa Y N and Okada F 1987 *IEEE Trans. Magn.* **23** 2431

Ochura K, Nakamura T, Yamamuro T, Ebisawa Y, Kokubo T and Oka M 1994 *J. Mater. Sci. Mater. Med.* **3** 95

Ohtsuki C, Kokubo T and Yamamuro T 1992 *J. Mater. Sci.: Mater. Med.* **3** 119

Electrical conduction mechanism in solution grown doped polyvinyl pyrrolidone films

P K KHARE*, S K PALIWAL, R KURARIA, H L VISHWAKARMA, ASHISH VERMA[†] and S K JAIN[‡]

Department of Postgraduate Studies and Research in Physics, Rani Durgavati Vishwavidyalaya, Jabalpur 482001, India
[†]Department of Physics, Dr H S Gour University, Sagar 470003, India
[‡]Central Instrumentation Lab, Dr H S Gour University, Sagar 470003, India

Abstract. A detailed study of electrical conduction mechanism in bimetallized ferrocene-doped polyvinyl pyrrolidone films was carried out. The measurements were carried out on films of about $20\,\mu m$ thick, in the field range of $(2.0-8.0)\times 10^4$ V/cm at temperatures ranging from 363 to 423 K. An investigation of the effect of impurity such as ferrocene in the polymer matrix was undertaken. Lowering of activation energy and increase in current due to doping were observed. The results showed that the charge carriers were generated by field-assisted lowering of coulombic barriers at the traps and were conducted through the bulk of the material by a hopping process between the localized states by a Jonscher–Ansari modified Poole–Frenkel mechanism. The dependence of current and activation energy on the ferrocene concentration is explained on the basis of charge transfer type of interaction between dopant and polymeric material.

Keywords. Electrical conduction; polyvinyl pyrrolidone; ferrocene; Poole–Frenkel; hopping; charge transfer complex.

1. Introduction

Polymers with controlled conductivity and thermal sensitivity are very much desirable in various applications (Cassiers 1960; Dresner and Comizzoli 1972; Pillai *et al* 1980). Studies of the transport mechanisms in polymer films have gained importance in recent years owing to the potential applications of films in various device technologies (Seanor 1982). Based on current–voltage characteristics, the deduction of the responsible conduction mechanism amongst various possibilities is seldom simple. Different workers have given different interpretations of their results but it seems no ultimate view has yet been reached. The elucidation of the underlying charge injection and carrier migration process is vital to the future utility of these materials. It has been shown that charge storage property and carrier mobility can be greatly affected by impregnating the polymers with suitable dopant (Sinha and Srivastava 1979; Mizutani *et al* 1984; Narsimha Rao *et al* 1986; Mohana Raju *et al* 1990; Vinod Dubey *et al* 1990). Depending on their chemical structure and the way in which they react with the macromolecular matrix, doping decreases the resistivity of the polymer to different degrees. The structural

changes affect the conductivity by changing the number of charge carriers and/or their mobility.

Polyvinyl pyrrolidone (PVP) is known to have a growing pharmaceutical importance and possesses good electrical properties (Prescatt 1965; Narsimha Rao and Kalpalatha 1987; Khare *et al* 1994a; Khare and Chandok 1995b), which are greatly modified by impregnating it with suitable dopant. The effect of impurity like ferrocene on electrical conduction, which can give a better understanding regarding the motion of molecules and the migration of charge carriers involved in the relaxation mechanism has not been studied before. Ferrocene, a nonpolar inorganic substance, was selected in the present case as a doping substance for two reasons: (i) it is a π-bonded cyclopentadiene complex and due to the active π-bond it allows nuclear substitutional reactions (Woodward 1952), which means the chances of its linking with polymer matrix are increased, and (ii) it is a monomer (Phadke *et al* 1978) i.e. a polymer making substance and hence its chances of changing the properties of polymer seem to be greater (Khare *et al* 1994b).

In this paper, the experimental results on electrical conduction of ferrocene-doped PVP with different combinations of vacuum coated electrodes are discussed to elucidate the mechanism of nature of electrical conduction

aimed at finding the possibility of the existence and nature of distribution of traps and the role played by the carriers injected from the electrodes and volume-generated carriers.

2. Materials

Polyvinyl pyrrolidone (PVP) and ferrocene used in the present study were procured from M/s Glaxo Laboratory, Bombay. PVP is a polar polymer due to its carbonyl group of double bond in pyrrolidone ring (Tan and Challa 1976). The network structure of PVP has different lengths of π and σ bonds in between nitrogen, oxygen, carbon and hydrogen atoms (Kasha and Pullenan 1962; Palaska 1970; Standen and Scool 1970). The asymmetric distribution of electronic charges near different atoms (N, O, C and H) may be possible in PVP; hence it is a disordered material. Ferrocene is a π-bonded, orange, nonpolar crystalline solid. It is a cyclopentadiene complex having molecular formula $C_{10}H_{10}Fe$ in which an iron atom is sandwiched (Dunitz and Orgel 1953) between two cyclopentadiene anions. There are eighteen valence electrons (in addition to single C–H bonds and C–C bonds of the two rings), i.e. a pair for each of the nine orbitals of iron atoms. These nine pairs of electrons may be distributed on ten C–C and ten Fe–C bond positions using only stable orbitals of atoms. The Fe–C bonds have a small amount (12%) of ionic character.

3. Experimental

The isothermal immersion technique was utilized for preparing films of ferrocene-doped polyvinyl pyrrolidone (PVP). The solution was prepared in a glass beaker by first dissolving 2·4 g PVP in 30 ml of chemically pure chloroform at room temperature. The doping concentration was changed by varying the amount of ferrocene (i.e. 50, 100, 150 and 200 mg) added to the polymer matrix by weight quantities. A change of colour of doped films from white to yellow was noticed. A dopant concentration of 50 mg was used unless specified otherwise. The upper metal electrode was also vacuum deposited. The following electrode combinations were used—Al–Al, Al–Ag, Al–Cu and Al–Sn. The thickness of the samples was of the order of 20 μm and estimated by measuring the capacitance of the fabricated sandwiches taking the value of dielectric constant, ε, of PVP as 2·5. Samples of different thicknesses were obtained by changing the concentration of polymer solution. The geometry of the sandwich configuration of the electrode and the variation of current in these structures as a function of the applied field, temperature and thickness was the same as reported previously (Khare and Srivastava 1992a, 1994; Khare *et*

avoid ground loops or extraneous electrical noise. The voltage was applied from a stabilized high voltage unit EC (HV 4800 D).

The measurements were carried out with the polarizing fields ranging from $(2–8) \times 10^4$ V/cm at temperatures 363–423 K. The temperature and field range were limited, because, beyond these films showed breakdown.

4. Results and discussion

The current–voltage (*I–V*) characteristics of ferrocene-doped (50 mg) polyvinyl pyrrolidone (PVP) on a semilog scale are shown in figure 1, for various fixed temperatures (363, 373, 393, 403, 408, 413, 418 and 423 K). The effects of higher concentrations of ferrocene (i.e. 100, 150 and 200 mg) on *I–V* characteristics of polymer matrix (at a fixed temperature 373 K) have also been placed in the same figure. The *I–V* curves show two distinct regions corresponding to two different types of conduction. At lower fields (region I) the slope of the *I–V* curve lies between 0·92 and 1·13, suggesting ohmic behaviour in this region. At moderate fields (region II), the slope of the *I–V* curve ranges from 1·4–1·68, indicating
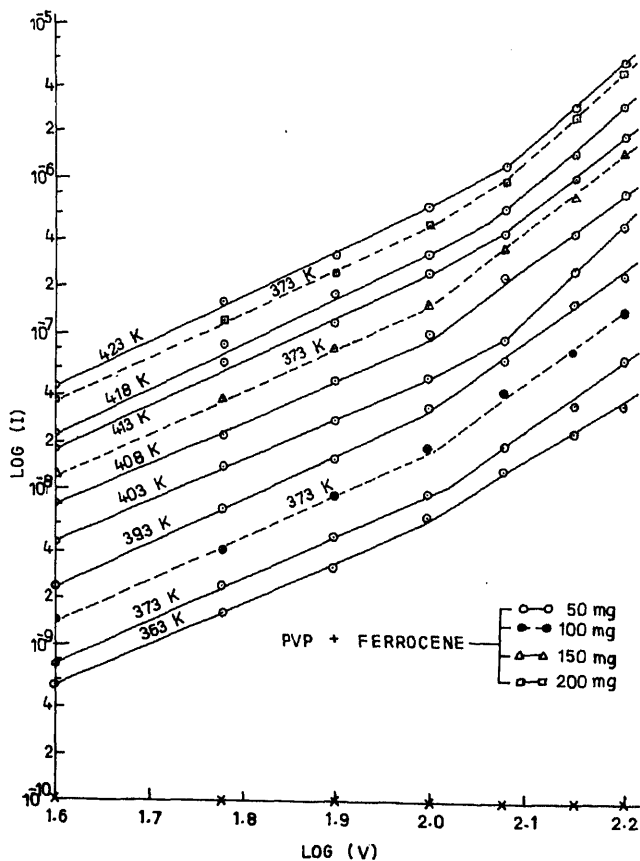
non-ohmic behaviour. The transition voltage which separates the two regions was found to be independent of temperature. The above results indicate that with the increase of temperature the probability of thermal ionization of the trapping centres increases, thus causing a shift in the quasi-Fermi level, which gives rise to a lowering of the barrier across which electrons have to be transported and the conduction becomes more or less ohmic. The increase in current at high temperatures can be due to softening of the substance and because of this the injected charge carriers can drift more easily to the dielectric volume. This gives rise to a large current at high temperatures. At lower fields, the injection of carriers from the contact is less and the initial current is governed by the intrinsic free carriers in the materials. The current will be ohmic until the injected free carrier density becomes comparable with the thermal carrier density.

In materials having low conductivity such as polymers, electric currents induced by carriers injected from the electrodes are generally bulk limited. This bulk-limited current requires that a sufficient carrier reservoir, available for injection, is maintained at the contact. The steady state current in such a case varies as the square of the applied field. The current–voltage relationship, $I \propto E^2$, does not fit well with the experimental data. Hence the possibility of space charge limited current can be excluded.

In general, the polymers are homogeneous mixtures of polycrystalline and amorphous regions. Hence, there have been controversies over transport theories in the literature and no single mechanism was able to explain the entire conduction in these materials. However, the theories proposed for amorphous and polycrystalline inorganic solids are normally applied to describe the conduction behaviour of these materials with few limitations (Dasaradhudu and Narsimha Rao 1994). The other likely processes are tunneling (Emtage and Tantraporn 1962), ionic conduction (Mott and Gurney 1948), field-enhancement thermionic emission either over an interfacial barrier (Schottky emission) (Langyel 1966) or from localized coulombic traps in the dielectric material (Poole–Frenkel (P–F) mechanism) (Frenkel 1938).

The results based on the isothermal I–V characteristic indicate thermally activated conduction over the entire temperature range (figure 1). Hence, the possibility of a tunneling mechanism being operative in the present case can be ruled out. The Richardson–Schottky (R–S) plots between $\log I$ and $\sqrt{E}$ at different temperatures are shown in figure 2. The nature of these plots indicates that the conduction process is governed by a mechanism in which the charge carriers are released by thermal activation over a coulombic potential barrier that is

charge carriers (electrons) can cross over the barrier between cathode and dielectric, as is the case with Schottky emission, taking the image force into consideration. Alternatively, carriers can be released due to ionization of impurity centres in the dielectrics (Poole–Frenkel effect). In both the above processes there is the current–field relationship of the form

$$I \propto \exp \beta E^{1/2}.$$

The restoring force in R–S and P–F effects is the Coulomb interaction between the escaping electron and positive charge. They differ in that the positive image charge is fixed for P–F barriers but mobile for Schottky emission. This results in a barrier lowering twice as much for the P–F effect.

To determine the actual conduction mechanism, the value of the β-factor at different temperatures calculated from the slope of $\log I$ vs $\sqrt{E}$ are compared with the
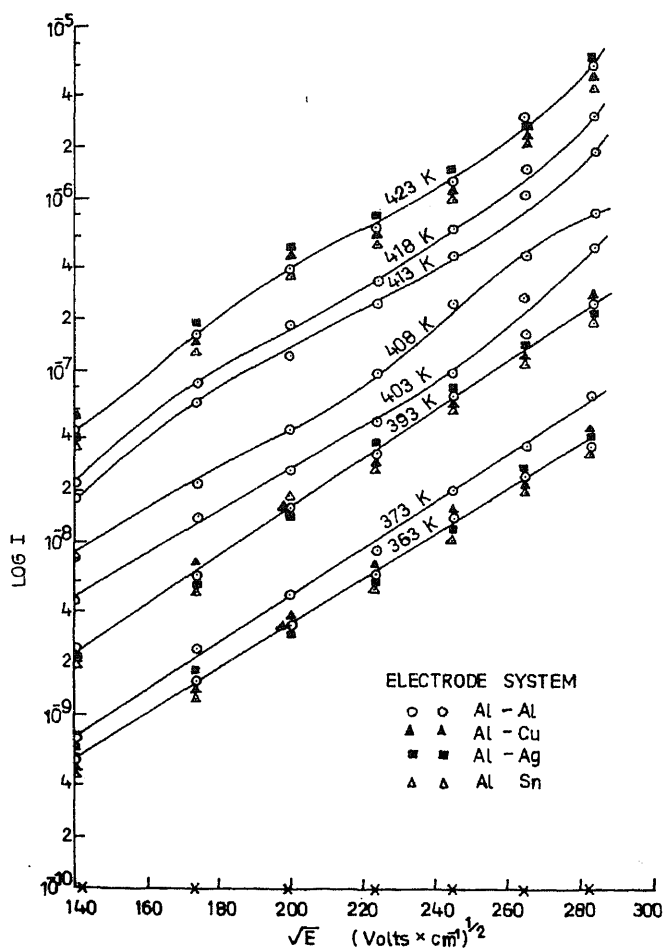

Figure 2. Log I vs $\sqrt{E}$ plots (Schottky plots—similar (Al–Al)

theoretically calculated value of β assuming a particular mechanism to be operative. The theoretical values of β_{PF} may be obtained from the relationship

$$\beta_{PF} = 2\beta_{RS} = 2 \left[\frac{e^3}{4\pi \varepsilon \varepsilon_0} \right]^{1/2}, \qquad (1)$$

where ε_0 is the permittivity of free space, ε the high frequency dielectric constant and e the electronic charge.

The experimental and theoretical values of β for Richardson–Schottky and Poole–Frenkel mechanisms are shown in table 1. The experimental values of β are in close agreement with the theoretically calculated values of β_{PF}. Hence, the P–F mechanism seems to be the governing mechanism in the present case.

The variation of current with thickness of ferrocene-doped PVP films was also studied to predict the conduction mechanism (figure 3). With the decrease in the thickness of the films the value of currents increases. The charge release is determined by the thickness of the charge layer relative to that of the sample. Thin samples will release more charges than thick ones because the charge carriers responsible for electret effect do not penetrate to a depth of more than few microns. The shallow traps are filled first and the charges move to the deeper traps afterwards. If the sample is thin, all the charges trapped in shallower traps is released immediately, however, the charge carriers that have moved to the deeper traps are not released immediately, consequently, charge released in case of thin samples is greater than the thicker ones. The nature of the plot is such that the space charge conduction (SCLC) mechanism in these films can be ruled out because SCLC predict a linear variation of current with thickness.

However, mere compatibility between β_{exp} and β_{theor} values cannot be taken as evidence for deciding the actual conduction mechanism (Simmons 1967), since β values depend on a number of experimental conditions. Further, there are a number of shortcomings in Schottky emission theory as it suffers from large deviations in its constants, which may not correlate with theoretical and experimental results (Lamb 1967). Similarly, the

Poole–Frenkel mechanism maintains Richardson–Schottky formalism, taking into consideration the barriers due to traps. Several workers have tried to distinguish between the two mechanisms by a comparison of β values but point out that values of β may vary with condition of traps in the bulk of the polymer (Mark and Hartman 1967; Yeargan and Taylor 1968; Rehnebaker 1969). The P–F mechanism assumes that once the carriers are thermally activated from their trapping sites with the assistance of the field, they are free to move unobstructed within the conduction band of the insulator. However, the concept of unobstructed motion of charge carriers is incompatible owing to the low mobility of the charge carriers observed in polymers ($\mu < 10^{-7}$ cm^2 V^{-1} s^{-1}) (Cresswell *et al* 1972). According to Jonscher and Ansari (1971), conduction in polymeric dielectrics with low mobility charge carriers should be interpreted as conduction by localized charge carriers performing hopping.

In order to decide the type of conduction mechanism operating in the polymer films, the effect of the nature of the electrodes of different work functions on the *I–V* characteristic was studied, since electrodes of different work functions induce different amounts of charge carriers into the bulk of the dielectric in the case of R–S mechanism, whereas the current flowing through the bulk of the film will be independent of the electrode materials in the case of the P–F mechanism. Therefore, if one takes an asymmetric metal–insulator–metal structure with two electrodes of different work functions, the current in the case of the Schottky effect will be asymmetrical when polarities are reversed (Khare *et al* 1994a) but will remain practically unchanged in the case of the Poole–Frenkel effect, since it does not depend on potential barriers of the interfaces. This is the proper way of distinguishing between the Poole–Frenkel and Schottky mechanisms as suggested by Jonscher and Ansari (1971) and Carchano and Vanentin (1975). Figure 2 shows Richardson–Schottky plots with aluminium electrodes along with corresponding curves for silver, copper and tin electrodes. It may be observed from these curves that the effect of different electrode materials on the

Table 1. Theoretical and experimental values of β and activation energies for ferrocene (50 mg)-doped polyvinyl pyrrolidone films.

Temperature (K)	Dielectric constant (ε)	β_{RS} ($.. \times 10^{-2}$)	β_{PF} ($.. \times 10^{-2}$)	β_{exp} ($.. \times 10^{-2}$)	Field ($.. \times 10^4$) (V/cm)	Activation energy (eV)
363	2·70	2·897	5·694	4·982		
373	2·64	2·613	5·226	4·766	2·0	0·97
393	2·62	2·591	5·182	4·529	3·0	0·91
403	2·63	2·522	5·044	4·769	4·0	0·84
408	2·60	2·397	4·794	4·139	5·0	0·772
413	2·57	2·422	4·844	3·989	6·0	0·720

I–V characteristics is negligible within the experimental error. Hence conduction is not electrode limited, and therefore the P–F conduction mechanism seems to be a more appropriate mechanism.

The electrical conduction, in general, may be attributed to ions, impurity incorporations and electrons which migrate along the polymer chains and also to the charges released by electrolytic dissociation under thermal activation. The distinction between electronic and ionic conduction is difficult but it is suggested that ionic conduction is characterized by low mobilities and high activation energies, while electronic conduction is associated with relatively higher mobilities and lower activation energies. It is not possible to give definite limits for activation energy, but Jonscher and Ansari (1971) suggest that values less than 0·8 eV would normally be considered as the electronic conduction mechanism, while values around and excess of 0·8 eV would normally be attributed to ionic support. The modified P–F model (Jonscher and Ansari 1971) assumes that the electrons produced as a

result of the field-assisted thermal ionization of donor-like centres perform thermally activated hopping between localized states. The effect of an external field is to lower the potential barrier between the hopping states from the initial value W_0 to a value $W_0 - \nu E^{1/2}$ where $\nu = (e^3/\pi\varepsilon\varepsilon_0)^{1/2}$ and has the same value as in the classical P–F mechanism. The modified P–F mechanism predicts an activation energy which is decreasing with the square root of the applied field.

The conductivity was evaluated from the measured values of current from the plots of figure 1 at different temperatures, the characteristics of which are shown in figure 4. Two distinct regions are seen and these indicate different slopes at lower and higher temperature regions. Two cases are readily distinguishable experimentally simply by comparing the activation energies at lower and higher temperatures in different regions. In case of many polymers, glass transition temperature T_g can be measured from the change in slope of σ vs $10^3/T$ plots. A change in slope in σ vs $10^3/T$ plot of figure 4 is also observed in the present case and indicates a transition temperature of doped PVP ~ 393 K. The T_g of pure PVP (Palaska 1970; Standen and Scool 1970) is 413–433 K, but in the present case, it is found to be 393 K, indicating that dopant reduces T_g of the polymer matrix. The dependence of conductivity on temperature for doped samples shows two distinct regions (figure 4) i.e. one below T_g and the other beyond T_g.
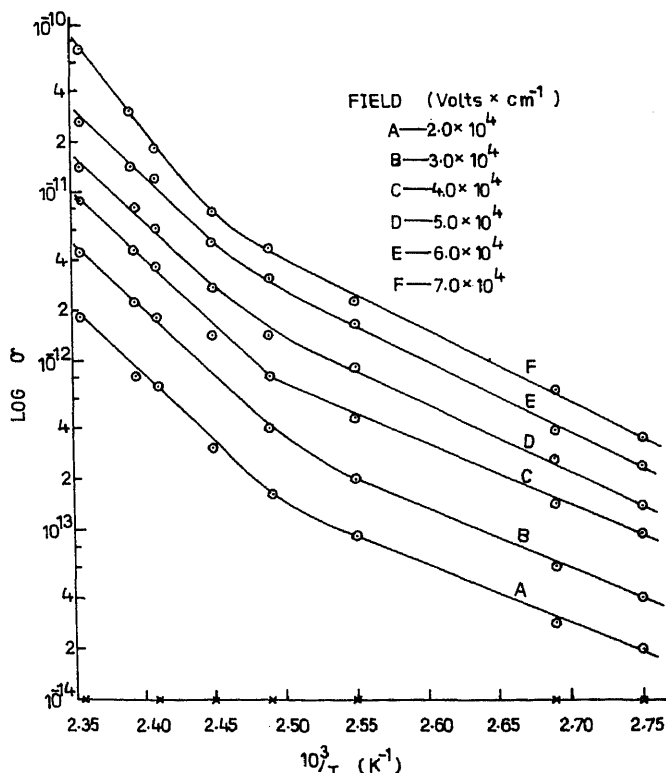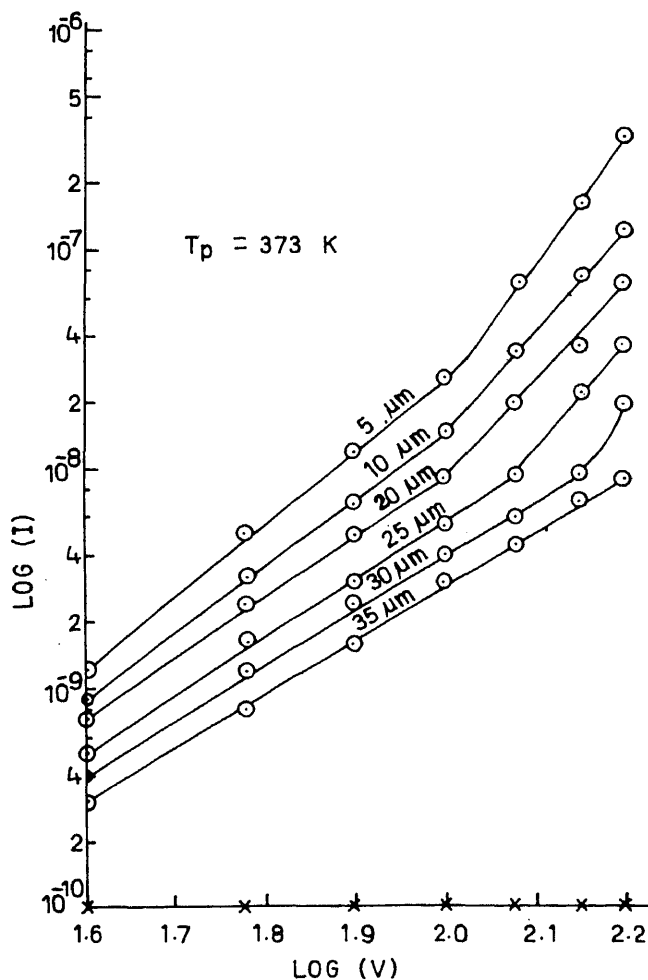
The low-temperature slope is an arbitrary one and depicts the complex temperature dependence of distributed relaxation processes (Vanderschuren and Linkens 1978). The high-temperature slope $(T > T_g)$ is generally related to an ionic conduction process. According to Van Turnhout (1975), conductivity in polymers shows a sharp increase near T_g. At T_g, molecular motion of the chain segments lowers the trap depth considerably and trapped charges are released by thermal excitation. Above T_g, life time of carriers in the conduction band is more which increases the conductivity rapidly. At low temperatures, conductivity is low. The small conductivity is due to trapping of injected charge carriers from electrode at different levels (Perlman 1972). Detrapping from these levels requires increased molecular motion of polymer chains. When thermal energy is supplied to a polymer its temperature increases which induces various transition in them. Increased molecular motion due to increase of temperature causes thermal excitation of charge carrier from the traps, either directly or due to lowering of trap depth. Molecular motions also result in release of trapped carriers due to loss of trapping sites.

The electrical conductivity for samples doped at lower concentration remains low even beyond T_g. It seems that chain motion is not effective in mobilizing the traps formed by dopant molecules and charge carriers released from mobilized traps, are again trapped in traps provided by dopant molecular sites. Thin polymer films are known to be a mixture of amorphous and crystalline regions (Chopra *et al* 1971). The conductivity behaviour of such films may be dominated by the properties of the amorphous regions (Kosaki *et al* 1971). The presence of amorphous regions gives rise to localized states. Since there are many localized states, the release or excitation of the carriers in these states dominates the conduction process. Consequently, doping should not affect the conductivity too much (Marikhin *et al* 1965), unless the dopant is present in sufficient quantities to markedly affect the position of the Fermi level. Dopant molecules enter either the amorphous regions of the polymer or the defect regions like chain folds. If they are present in low concentrations, they will give rise to additional molecular sites for trapping of charge carriers (Jonscher 1967). Such localized sites can be defined in molecular terms using the difference in ionization potential as an indication of trap depth. As the dopant concentration is increased, the molecules start bridging the gap separating the two localized states and lowering the potential barrier between them thereby facilitating the transfer of charge carriers (Sinha and Srivastava 1979; Kulshrestha and Srivastava 1980).

The activation energies were calculated from the slopes of figure 4 and were plotted against the square root of the applied voltages. A straight line (figure 5) is obtained. The intercept of this straight line at zero field gives a value of $W_0 = 1.568 \times 10^{-19}$ J (0.98 eV). Its slope gives the value of $\nu = 5.976 \times 10^{-24}$ J m$^{1/2}$ V$^{-1/2}$, which is in agreement with its theoretical value of 6.214×10^{-24} J m$^{1/2}$ V$^{-1/2}$. Hence, our data fits fairly well in the modified P–F equation.

The activation energy values observed in the present case are fairly high. Therefore, the possibility of charge carrier species inside the polymer bulk ionic in nature cannot be completely ruled out. Ionic conduction in polymeric materials is a controversial subject. Adamec and Calderwood (1978) have reported the existence of free charge carriers in polymers. Lilly and McDowell (1968) have also reported ionic space charge conduction under high field conduction.

A comparison of currents of pure PVP and ferrocene-doped PVP reveals that an increase in current is observed with doping. Ferrocene is markedly aromatic in character and has three trap levels (Sauthgate 1976). The presence of trap levels may be due to morphological changes in structure. Addition of impurities like ferrocene, introduces charge carriers and trapping levels in PVP–ferrocene matrices (Khare *et al* 1997). The increase in current and decrease in activation energy in ferrocene-doped PVP films can be explained in terms of charge transfer complex formation as evidenced by the optical absorption spectra of pure ferrocene and ferrocene-doped PVP films.

The formation of charge-transfer complexes is characterized by the appearance of a new absorption band or
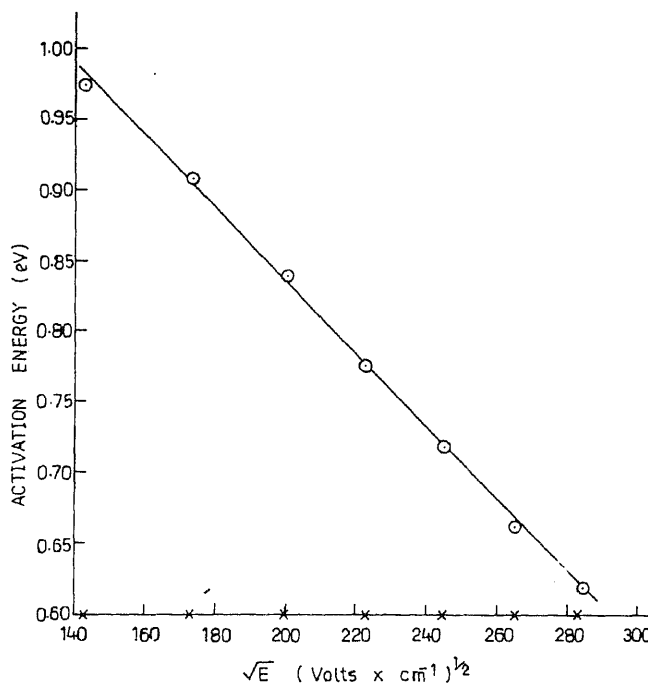

**Figure 5.** Activation energy vs square root of field for

ening in the absorption band in the UV-visible region of the spectrum (Rao 1967). The UV spectrum of ferrocene, undoped and ferrocene (50 mg)-doped PVP are shown in figures 6 and 7, respectively. A well-defined sharp band at 246 nm for PVP was observed. The UV spectrum for ferrocene consists of one ill-defined band, along with a sharp and a wide band at 252, 284 and 440 ± 20 nm, respectively. However, in the case of ferrocene (50 mg)-doped PVP, UV spectrum exhibits all the three bands (as in the case of pure ferrocene) at 252·5, 294 and 440 nm, respectively. The width and intensity of the bands have been found to increase with dopant incorporation.

The effect of dopant incorporation may also be interpreted on the basis of the microscopic structure of the polymer in thin film form. The polymer film, in general, consists of crystalline regions in which the molecular chains of the polymer are regularly folded or entangled. These crystalline regions are connected to amorphous regions in which the molecular chains of the polymer

are irregularly folded. The motion of carriers is impeded at these crystalline–amorphous interfaces. Dopants, which may be present either as molecules or as molecular aggregates, generally tend to diffuse preferentially into the amorphous regions of the polymer (Khare and Singh 1994). The presence of dopants in these regions causes a reduction of the crystalline–amorphous interface, which provides conductive pathways through the amorphous regions.

Table 2. Activation energy for ferrocene-doped polyvinyl pyrrolidone films at 373 K.

Field ($\times 10^4$ V/cm)	Activation energy (eV $\pm$ 1·5%)			
	Ferrocene content in polymer matrix			
	50 mg	100 mg	150 mg	200 mg
2·0	0·97	0·952	0·948	0·939
5·0	0·772	0·769	0·751	0·749
8·0	0·62	0·619	0·608	0·597
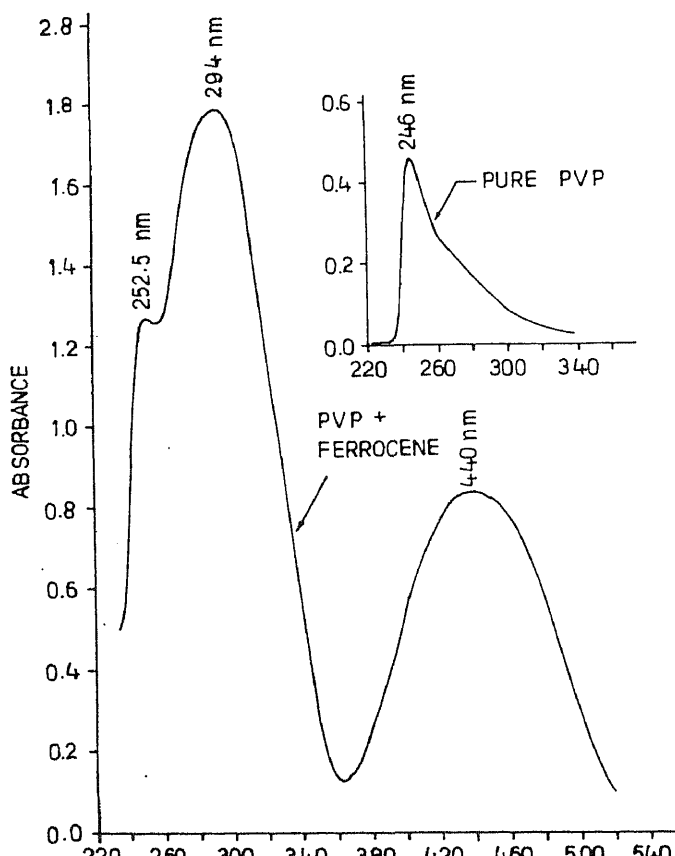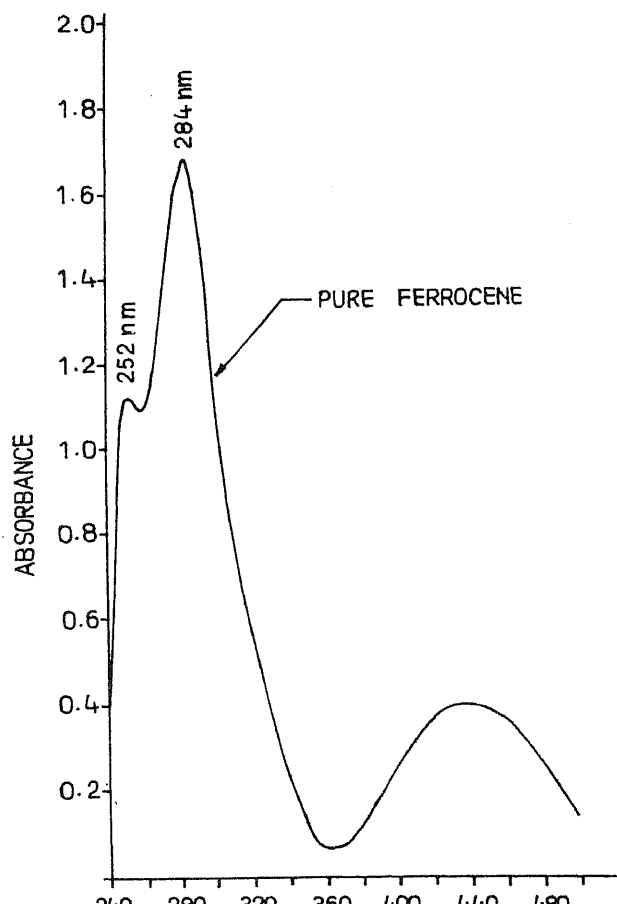
In polymers, surface states, chain folding, molecular disorders, crystalline–amorphous boundaries and chain ends may act as trapping sites. In addition polymer contains polar groups, where each dipole can act as an electron or hole trap (Seanor 1982). Polar groups may act as trapping sites and the chain folding also acts as traps. The charge carriers trapped at these trapping sites may be excited and contribute to the total conduction. PVP is a polar polymer. The polar side group moiety, pyrrolidone ring in PVP has carbonyl group of double bond. This group is attached to the main chain with an amide bond. The active groups of PVP are carbonyl groups and tertiary nitrogen atoms attached to the amide bond, which are in a reactive position at certain temperatures. The higher electronegativity of different atoms such as oxygen or nitrogen of PVP suggests the formation of CTC with ferrocene (Khare and Jain 1997). The side group of PVP (π electrons) may form CTC by donating the electrons to ferrocene or nitrogen atom may also be involved in CTC formation at certain higher temperatures after the side group rotation of PVP. Ferrocene is π-bonded nonpolar crystalline solid. Increase in ferrocene concentration in PVP increases the anisotropy (Khare and Chandok 1995a), which may be responsible for the creation of new tapping sites. Due to active π-bond it allows nuclear substitutional reaction which may result in the formation of charge transfer complexes. This agrees with the earlier findings (Khare and Srivastava 1992b; Khare *et al* 1993).

5. Conclusion

The current–voltage characteristics of ferrocene-doped PVP films show two regions corresponding to two different types of conduction. The conduction in low-field region is nearly ohmic while in moderate field region it is controlled by a Jonscher–Ansari modified P–F mechanism. The dependence of current and activation energy on the ferrocene concentration is attributed to charge transfer type of interaction.

References

Adamec V and Calderwood J M 1978 *J. Phys. D, Appl. Phys.* **11** 781
Carchano H and Vanentin M 1975 *Thin Solid Films* **30** 335
Cassiers P M 1960 *Photogr. Sci. Engg.* **4** 199
Chopra K L, Rastogi A C and Malhotra G L 1971 *Thin Solid Films* **24** 125
Emtage P R and Tantraporn W 1962 *Phys. Rev. Letts* **8** 267
Frenkel J G 1938 *Phys. Rev.* **54** 647
Jonscher A K 1967 *Thin Solid Films* **1** 213
Jonscher A K and Ansari A A 1971 *Philos. Mag.* **23** 205
Kasha M and Pullenan B P 1962 *Horizon in biochemistry* (Albert Szent Gyooryi Dedicatory Vol.) (New York: Academic) p. 364
Khare P K and Srivastava A P 1992a *Indian J. Pure & Appl. Phys.* **30** 131
Khare P K and Srivastava A P 1992b *Indian J. Pure & Appl. Phys.* **30** 326
Khare P K and Ranjeet Singh 1994 *Polym. Int.* **34** 403
Khare P K and Srivastava A P 1994 *Indian J. Pure & Appl. Phys.* **32** 14
Khare P K and Chandok R S 1995a *J. Polym. Mater.* **12** 23
Khare P K and Chandok R S 1995b *Indian J. Phys.* **A69** 545
Khare P K and Jain S K 1997 *Indian J. Pure & Appl. Phys.* (to be published)
Khare P K, Gaur M S, Alka Bajpai, Pandey R K and Srivastava A P 1993 *Indian J. Pure & Appl. Phys.* **31** 326
Khare P K, Alka Bajpai and Srivastava A P 1993 *Indian J. Pure & Appl. Phys.* **31** 405
Khare P K, Sandeep Shrivastava and Srivastava A P 1994a *Indian J. Phys.* **A68** 129
Khare P K, Keller J M, Gaur M S, Ranjeet Singh and Datt S C 1994b *Polym. Int.* **35** 337
Khare P K, Vishwakarma H L and Srivastava A P 1994c *Indian J. Phys.* **A68** 571
Khare P K, Chandok R S, Neeraj Dubey and Srivastava A P 1994d *Polym. Int.* **35** 153
Khare P K, Jain S K and Paliwal S K 1997 *Bull. Mater. Sci.* **20** 1001
Kosaki M, Yoda M and Ieda M 1971 *J. Phys. Soc. Jpn* **31** 1598
Kulshreshtha Y K and Srivastava A P 1980 *Thin Solid Films* **69** 269
Lamb D R 1967 *Electrical conduction mechanisms in thin insulating films* (London: Methuen and Co. Ltd)
Langyel G 1966 *J. Appl. Phys.* **37** 807
Lilly A C and McDowell J R 1968 *J. Appl. Phys.* **39** 141
Marikhin V A, Shitsker A I and Yastrebinskii A A 1965 *Sov. Phys. Solid State* **7** 352
Mark P and Hartmann T E 1967 *J. Appl. Phys.* **39** 2163
Mizutani T, Mitani K and Ieda M 1984 *J. Phys. D: Appl. Phys.* **17** 1477
Mohana Raju K, Reddi P M and Murthy N M 1990 *Indian J. Pure & Appl. Phys.* **28** 47
Mott N F and Gurney R W 1948 *Electronic processes in ionic crystals* (London: Oxford University Press) 2nd edn
Narsimha Rao V V R, Subba Rao T and Narsing Das N 1986 *J. Phys. Chem. Solids* **47** 35
Narsimha Rao V V R and Kalpalatha A 1987 *Polymer* **28** 648
Palaska E J (ed.) 1970 *Encyclopedia of chemical technology*

Rao C N R 1967 *Ultraviolet and visible spectroscopy* (London: Butterworth) p. 147

Rehnebaker W B 1969 *IBM J. Res. Dev.* **13** 686

Simmons J G 1967 *Phys. Rev.* **155** 657

Sauthgate P D 1976 *Appl. Phys. Letts* **28** 200

Seanor D A (ed.) 1982 *Electrical properties of polymer* (New York: Academic Press)

Sinha H C and Srivastava A P 1979 *Indian J. Pure & Appl. Phys.* **17** 726

Standen A and Scool A (eds) 1970 *Plasma extenders in kirk othmer*, in *Encyclopedia of chemical technology* (New York: Interscience) Ist ed., Vol. 10, p. 421

Tan Y Y and Challa G 1976 *Polymer* **17** 739

Van Turnhout J 1975 *Thermally stimulated discharge of polymer Electrets* (Amsterdam: Elsevier)

Vanderschuren J and Linkens A 1978 *J. Appl. Phys.* **49** 78

Vinod Dubey, Pavan Khare and Saraf K K 1990 *Indian J. Pure & Appl. Phys.* **28** 579

Woodward R B 1952 *J. Am. Chem. Soc.* **74** 3458

Yeargan Y and Taylor H L 1968 *J. Appl. Phys.* **39** 5600

Electrical and optical properties of rf-sputtered CdTe films

P C SARMAH[†] and A RAHMAN*

Department of Physics, Gauhati University, Guwahati 781 014, India
[†]Regional Research Laboratory, Jorhat 785 006, India

Abstract. In this paper some electrical and optical properties of n-type CdTe films prepared by rf sputtering at 180 W power have been reported. For doping the films a number of pellets of pure Cd placed on the CdTe target were simultaneously sputtered with the target material to get Cd-doped CdTe films. The films after doping were found n-type. Maximum doping concentration obtained this way was of the order of 10^{14} cm^{-3}. XRF spectra of target material and the rf-sputtered films were found to be more or less similar. All the films were found to have large number of defects indicated by profound aging effect in the initial stages of aging. The films became stable for measurements after about 8–10 days. Activation energy and band gap found from the temperature dependence of dark conductivity were 0·5 eV and 1·43 eV respectively. Photoconductivity of the films was studied and the photoconductive rise time, decay time and the decay constants were determined from the photoconductive rise and decay curves at 500 Lx and 1000 Lx of intensity of illumination.

Keywords. Rf-sputtered film; doping; ageing effect; activation energy; photoconductive decay.

1. Introduction

Studies of CdTe thin films have received much attention for their various probable applications. This zinc blende type semiconductor (Rose *et al* 1987) having a direct band gap (~ 1·46 eV), is thought to be a promising candidate for thin film solar cell and other electro-optical devices. This is the only semiconductor of II–VI groups showing both types of conductivity (Zanio *et al* 1978).

Different techniques to prepare CdTe films to study their characteristics have been adopted by different workers. Some of them are vacuum deposition (Uda *et al* 1978), closed-space vapour transport and closed-space sublimation (Mitchell *et al* 1985), electrodeposition (Basol 1988), sintered films (Matsumoto *et al* 1984), spray pyrolysis (Banerjee *et al* 1989), rf-sputtering (Das and Cook 1988) etc. The main advantage of rf-sputtering is that stoichiometry of the sputtered material is retained in the deposited film (Fisher and Weber 1952), making it a suitable technique for depositing intermetallic compounds.

Many workers studied structural, electrical and optical properties of CdTe films prepared by rf-sputtering. Some of the properties studied by us have already been published earlier (Sarmah and Rahman 1990). Some unpublished works such as XRF studies, temperature dependence of resistivity, aging effect on resistivity and photoconductive rise and decay characteristics are presented in this paper.

2. Experimental

CdTe films were prepared by rf-sputtering in an argon ion atmosphere as reported in our earlier paper (Sarmah and Rahman 1990). In order to prepare Cd rich films, pellets of cadmium were fixed on the target to sputter simultaneously along with the target material. The rf power was maintained at 180 W in preparing all the samples. Two types of samples: gap-type and sandwich type, were prepared for electrical measurements. In gap type samples, indium was vacuum deposited on the two ends of rectangular CdTe films for electrodes. Sandwich type samples were prepared by depositing indium film before and after the deposition of CdTe films. Indium was found to make ohmic contact with n-type CdTe film. The work function of indium has been reported to be 3·97 eV (Rhoderik 1978) and that of CdTe to be > 4 eV (Sheer and Laar 1961), which satisfy the condition for making ohmic contact between them. For compositional analysis of rf-sputtered CdTe films, XRF spectra were taken with the help of a Philips pw-1480 spectrometer. For studying different characteristics of the samples in dark and under illumination, experiments were carried out in a specially designed apparatus as shown in figure 1. The apparatus consisted of two coaxial cylinders, the inner one being supported by the outer one. The outer cylinder has a side tube fitted with an air tight window. The sample holder with the sample in it was vertically clamped to the outer surface of the inner cylinder so that the sample faced the glass window. Shielded wires from the pressure contacts to the vacuum

---

heater was placed inside the inner cylinder whose temperature was controlled by a temperature controller (Philips-LD 30). An X–Y recorder (Digital Electronics Ltd) was used for the purpose of measurements. For taking I–V curves the bias voltage was given from a variable ramp (Systronic, model 1014). For photoconductive rise and decay, a constant voltage was applied to the sample through a standard resistance and was connected to the X–Y/t recorder. The voltage applied to the sample was connected to the X-axis of the recorder and the potential drop across the standard resistance due to the current flowing through the sample was connected to the Y-axis of the recorder. The annular space between the two co-axial cylinders was evacuated to about 10^{-2} torr by a rotary pump before taking any measurement.

3. Results and discussion

We have reported XRD studies in an earlier paper (Sarmah and Rahman 1990) and showed that the CdTe films prepared at lower rf power were amorphous and those prepared at higher power polycrystalline in nature. We have also observed that when the film was doped with In or Cd during sputtering, the film became more disordered (though not amorphous) even at higher power, compared to intrinsic film prepared at the same rf power. XRF spectra of target material and the rf-sputtered films were also taken to know the compositions and quality of films. Three typical XRF spectra are shown in figure 2 for comparison.

These rf-sputtered films were always endowed with defects during deposition. With time some defects are likely to heal up due to ionic movements and as such film resistivity decreases showing aging effect. For the purpose of observing aging effect, resistivity of rf-sputtered Cd-doped films was measured at room temperature after different intervals of time. The resistivity was found to decrease rapidly in the initial stage of aging and then at slower rate approaching a saturation value after several days as shown in figure 3 for two typical samples. Such aging effect has also been reported by earlier workers (Gogoi and Barua 1982).

3.2 Activation energy and band gap

Temperature variation of conductivity of two typical Cd-doped CdTe films has been shown in figure 4. Both gap-type and sandwich-type samples exhibit similar behaviour except a slight shifting in conductivity value. This difference in conductivity of two types of samples may be attributed to the difference in thickness of the CdTe films. The thickness measured by interference method was taken for calculation of conductivity. But, obviously, in sandwich structure, the effective thickness was reduced due to penetration of counter electrode materials while in gap type samples thickness was not affected. However, the temperature dependence plots for both types of samples are parallel giving same activation energies.

The activation energy obtained from the slope at lower
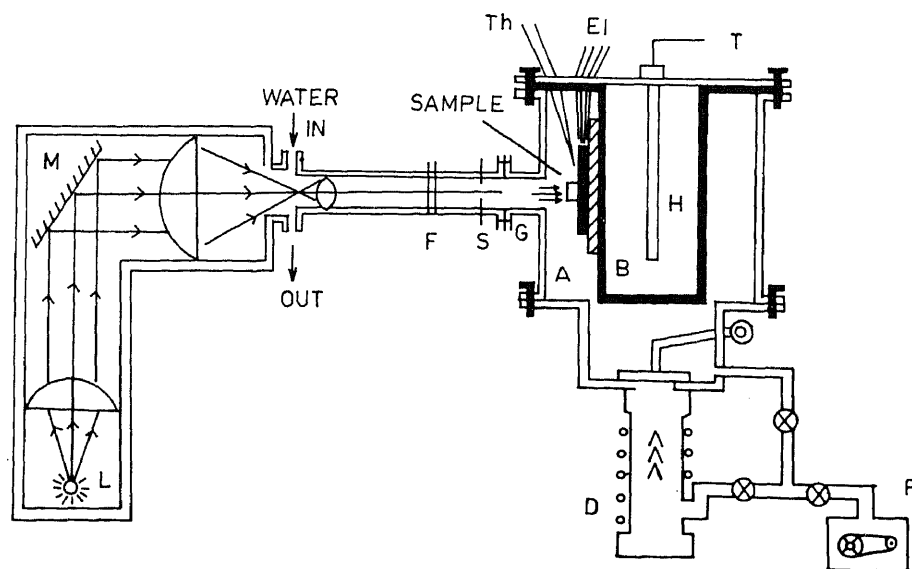
Figure 1. Experimental arrangement for different measurements (L, light source; M, mirror; A, outer cylinder; B, inner cylinder; G, glass window; S, shutter; F, arrangement for filters; Th, thermocouple; El, electrodes; H, heater; T, temperature controller; D, diffusion pump; P, rotary pump).
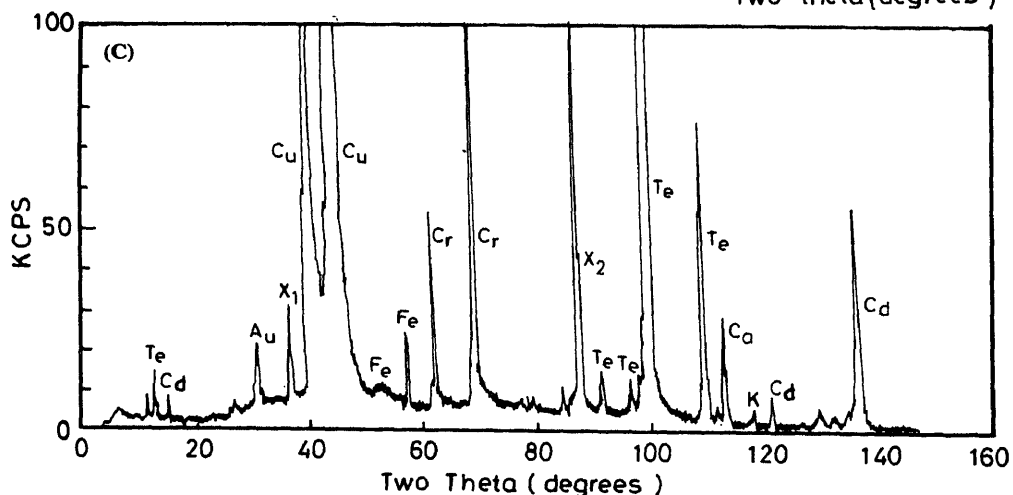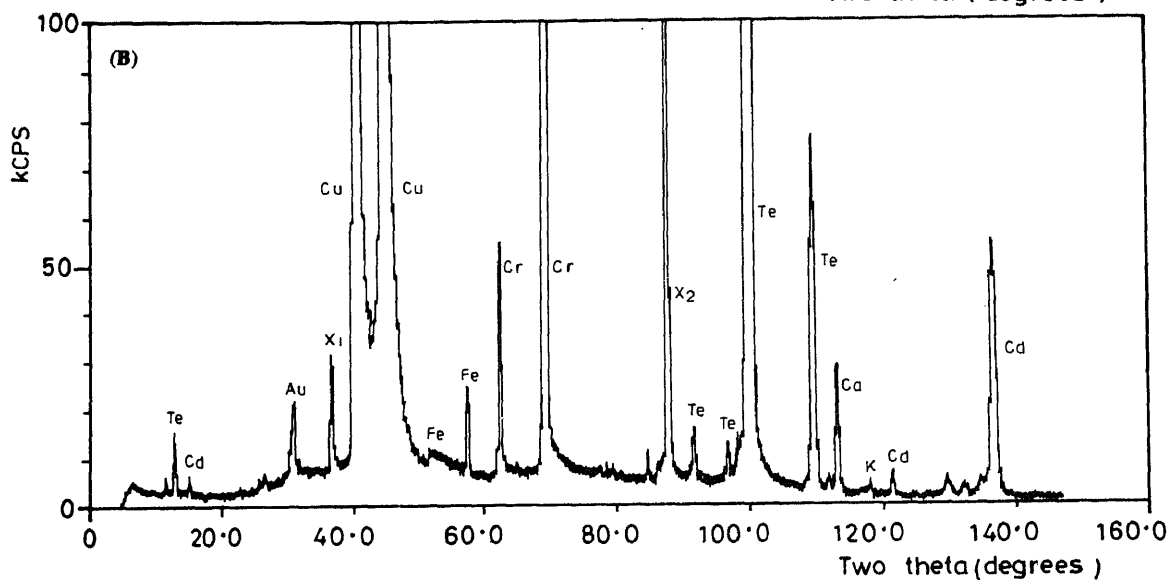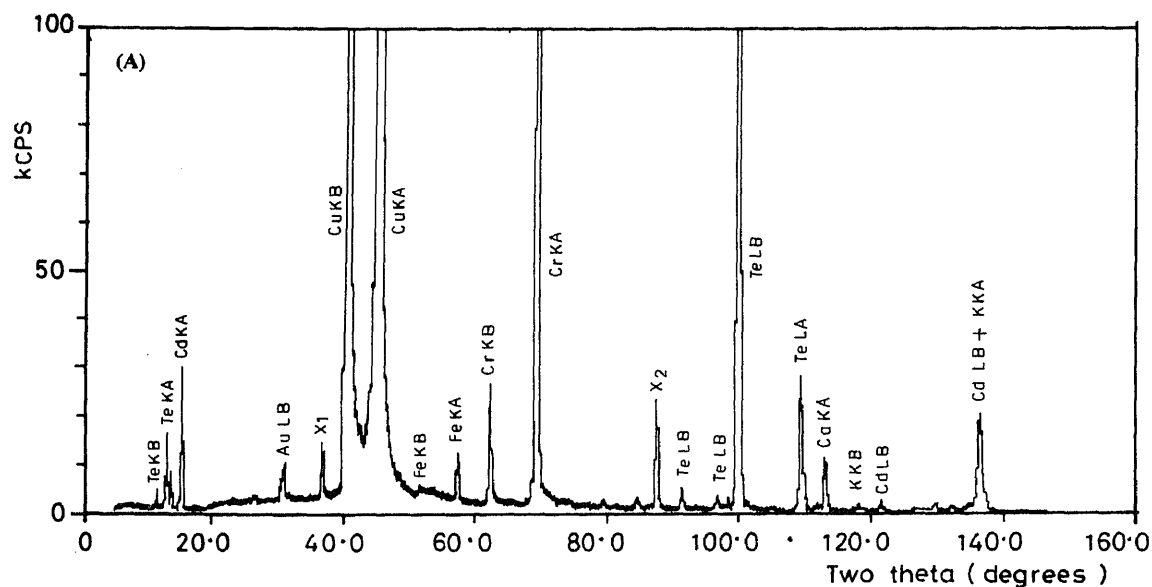
temperature region was about 0·5 eV. This corresponds
to impurity conduction due to excess cadmium. As the
temperature is raised, the impurity levels are exhausted
and the conduction becomes intrinsic in nature. The band
gap obtained from the slope at higher temperature region
was about 1·43 eV.

3.3 *Photoconductivity in CdTe films*

The variation of photocurrent with light intensity was
recorded at room temperature. Photocurrent was observed
to increase with light intensity showing saturation at
higher light intensity as shown in figure 5 for two
typical samples. The increase of photocurrent and decrease
of resistivity with light intensity is due to generation of
extra carriers upon illumination. At lower intensities the
concentration of available recombination centres is very
much larger than the concentration of free electrons,
most of the excited electrons have been trapped. Under
this condition, the photocurrent varies linearly with light
intensity. However, at higher illumination, generation of
carriers are controlled by the recombination processes
(Bube 1960).

The photoconductive rise and decay characteristics of
Cd-doped films at room temperature were recorded with
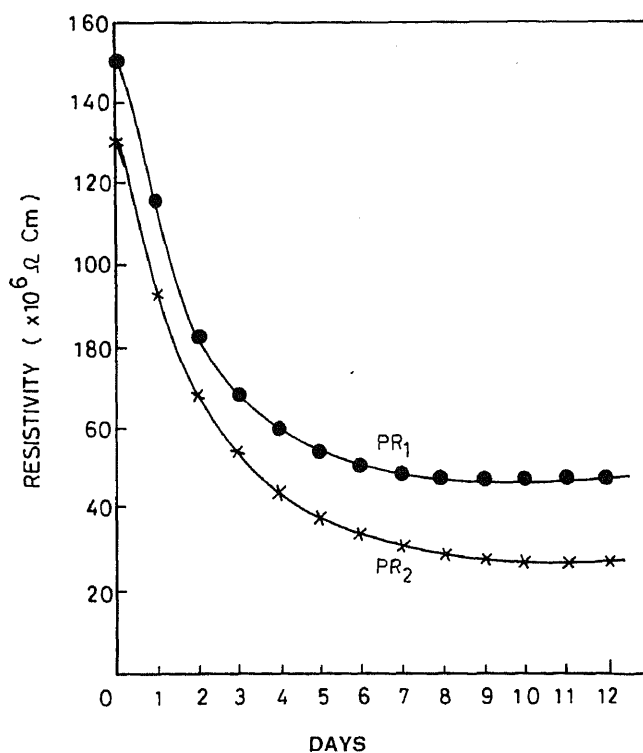an X–Y/t recorder. Figure 6 shows the rise and decay

Figure 4. In σ vs T^{-1} plots for two typical Cd-doped CdTe films prepared at 180 W. Sample PT1, gap type, doping conc. 6×10^{14} cm^{-3}; thickness 11,000 Å, gap area $7·8 \times 10^{-2}$ cm^2; sample PT2 sandwich type, doping conc. 3×10^{14} cm^{-3}; thickness 10,500 Å: electrode area $9·5 \times 10^{-2}$ cm^2.

Figure 3. Ageing effect on resistivity of two typical Cd-doped CdTe films prepared at 180 W, doping concentration 2·6 × 10^{14}
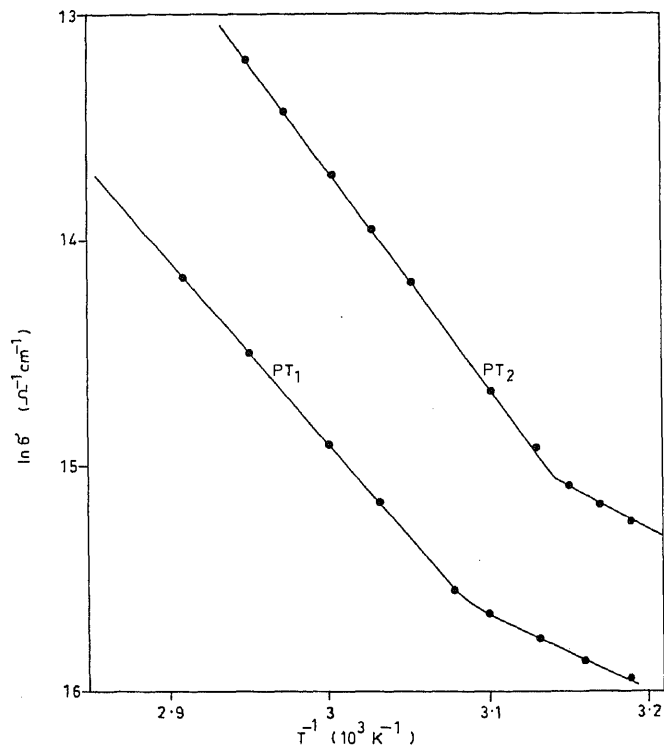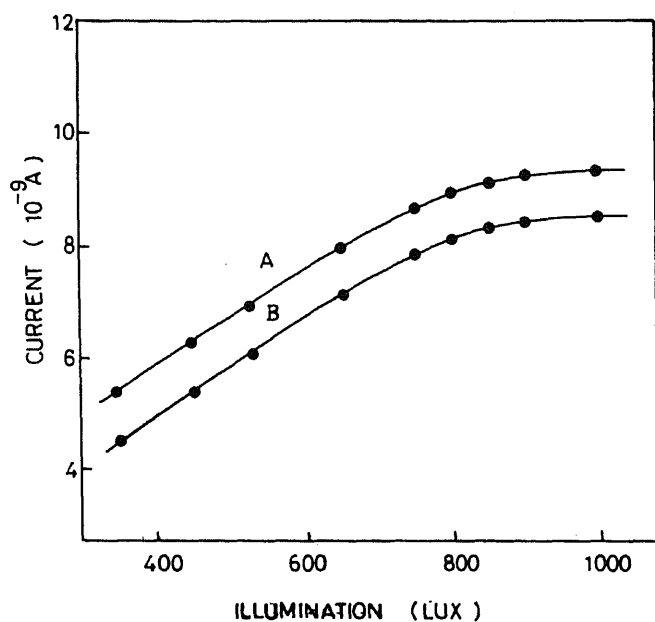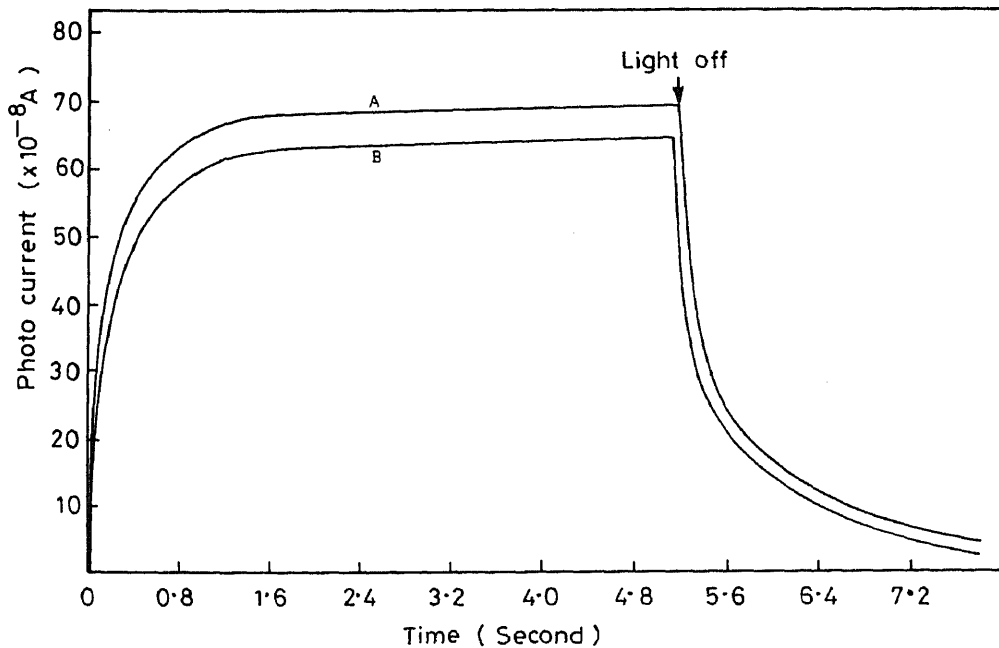

Figure 5. Variation of photocurrent with intensity of illumination for two typical films prepared at 180 W; sample A

Figure 6. Rise and decay of photocurrent with time at 300 K for a typical Cd-doped film. A, 500 Lx; B, 1000 Lx (rf power 180 W; doping conc. $2 \cdot 5 \times 10^{14}$ cm^{-3}; gap area $2 \cdot 5 \times 10^{-2}$ cm^2).
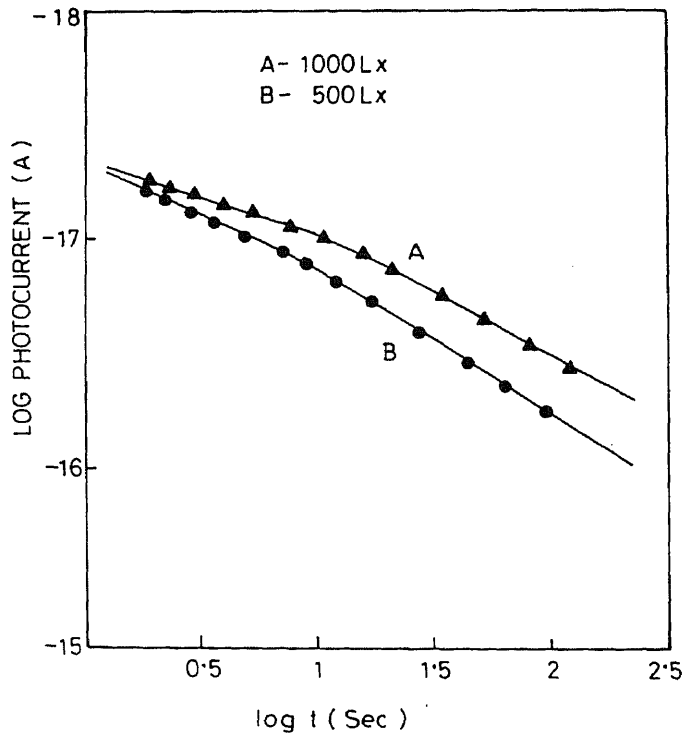
curves of a typical sample. The rise and decay processes are characterized by initial fast rise and slower decay. The rise and decay curves can be explained on the basis of release of electrons and holes under the influence of light accompanied by their recombination. The current reaches a steady value when the rate of recombination becomes equal to the rate of generation of new carriers and the concentration of carriers reach a steady value. When light is switched off, the initial rapid drop of photocurrent is controlled by recombination mechanism alone and depends on the life time of the majority carriers. However, at higher illumination the number of free carriers are higher than the trapped carriers and recombination takes place without involving trapping process (Bube 1960).

The photoconductive rise time t_r and decay time t_d were determined from the tangents to the rise and decay curves. The values have been observed to decrease with increase of illumination. The photoconductive decay curve has been found to fit the expression

$$I_{pt} = I_0 t^{-b},$$

where I_0 is the initial photocurrent at $t = 0$ and I_{pt} the photocurrent after time t and b the decay constant.

Two plots of log photocurrent vs log time of photo-

Figure 7. ln photocurrent vs ln time plots for photoconductive

Table 1. Values of photoconductive rise and decay times and decay constants of a Cd-doped sample at two intensities of illumination.

Intensity of illumination (Lx)	Rise time $t_r(s)$	Decay time $t_d(s)$	Decay constants	
			b_1	b_2
500	0·12	0·20	0·37	0·58
1000	0·08	0·16	0·56	0·68

Sample no. PO6, thickness 11,500 Å, rf power 180 W, gap area 2.5×10^{-2} cm^2, doping concentration 12×10^{14} cm^{-3}.

constants. They are observed to increase with illumination. The values of photoconductive rise time, decay time and the decay constants are given in table 1. The photoconductive response has been observed to be slightly lower in sandwich-type sample than in gap-type sample. This is possibly due to interception of illuminated light by indium electrode in sandwich-type sample.

4. Conclusions

Some properties of rf-sputtered Cd-doped CdTe films have been presented here. Doping of CdTe films by Cd from a number of pellets on the CdTe target during sputtering, can be achieved up to 10^{14} cm^{-3}. The films are found *n*-type and endowed with defects as indicated by the aging effect on resistivity. The resistivity of the films decreases very fast initially after the preparation of the samples and then slowly attaining a constant value after about 8 days. Temperature dependence of dark conductivity shows that conduction between room temperature to 338 K is mainly due to impurity levels, activation energy being about 0·5 eV. At higher temperature beyond 338 K the conduction becomes intrinsic showing

a band gap of about 1·43 eV. The photocurrent has been observed to increase rapidly with illumination at lower values and tends towards saturation at higher values. The photoconductive rise and decay curves have been found to decrease while decay constants increase with illumination.

References

Bube R H 1960 *Photoconductivity of solids* (New York: John Wiley and Sons, Inc.)
Banerjee A, Saha H and Guha R 1989 *Indian J. Phys.* **A63** 326
Basol B M 1988 *Solar Cells* **23** 69
Das S R and Cook J G 1988 *Thin Solid Films* **163** 409
Fisher T F and Weber C E 1952 *J. Appl. Phys.* **23** 181
Gogoi S and Barua K 1982 *Thin Solid Films* **92** 227
Matsumoto H, Kuribayashi K, Uda H, Komatsu Y, Nakano A and Ikegani S 1984 *Solar Cells* **11** 367
Mitchell K W, Eberspacher C, Cohen F, Avery J, Duram G and Bottenberg W 1985 *Proc 18th IEEE PVSC Las Vegas, NV* (New York: IEEE) p. 1359
Rhoderik E H 1978 *Metal–semiconductor contacts* (Oxford: Clarendon Press) p. 54
Rose M R, Lowrence A S and Wulf J 1987 *Electronic properties of matter* (New Delhi: Wiley Eastern Ltd.) p. 144
Sarmah P C and Rahman A 1990 *Indian J. Phys.* **A64** 21
Sheer J J and Van Laar J 1961 *Phillips Res. Rep.* **16** 323
Uda H, Taniguchi H, Yoshida M and Yamashita T 1978 *Jap. J. Appl. Phys.* **17** 585
Zanio K, Willardson R F and Beer A C (eds) 1978 *Semiconductors and semimetals* (New York: Academic Press) **13** 164

Hydrogen passivation studies in Pd/*n*-GaAs devices

U P SINGH*

Department of Physics, Banaras Hindu University, Varanasi 221 005, India
*Present Address: c/o Prof. C L Singh, Plot No. 1, L.B.S. Colony, Karaundi, Suswanhi, Varanasi 221 005, India

Abstract. The effect of hydrogen on the current (*I–V*) and capacitance (*C–V*, TSCAP) has been studied for Pd/*n*-GaAs diodes. Hydrogenation has been found to improve ideality factor of the diode. Reverse *C–V* characteristics show that the number of shallow and deep donors is reduced on hydrogenation. The TSCAP measurement shows the presence of two donor states at ~ 0·48 and 0·72 eV which is being partially passivated on hydrogenation. The likely origin of these states is discussed.

Keywords. Hydrogen passivation; Schottky diodes; TSCAP.

1. Introduction

Hydrogen passivation of shallow and deep levels in semiconductor has been an active area of research (Haller 1991; Pankove and Johnson 1991; Myers *et al* 1992; Pearton *et al* 1992), due to the high diffusivity and chemical activity at moderate temperature (~ 400°C). A controlled neutralization of dopants by hydrogen has resulted in improving the opto-electronic/electronic properties of a wide variety of semiconductors including the III–V compound semiconductor (Constant *et al* 1987; Jackson *et al* 1988). Common methods of intentional introduction of hydrogen into III–V compound are: hydrogen ion implantation and heating in hydrogen plasma. The latter leads to etching and damage in the near surface region while the former introduces a large number of compensating defects in bulk. In the present study, the passivation in *n*-GaAs has been attained through a supply of low energy hydrogen giving damage free injection. For this purpose Pd/*n*-GaAs diodes were fabricated and placed in a hydrogen atmosphere at room temperature. Palladium adsorbs the molecular hydrogen and stores it as atomic hydrogen. This, in turn, diffuses from palladium film to the Pd/GaAs interface towards the bulk semiconductor. We performed similar studies on silicon (Tripathi *et al* 1989, 1992) and GaAs (Srivastava *et al* 1991; Singh *et al* 1995), and shown that hydrogen diffuses to the interface and bulk, resulting in the passivation of the deep and shallow states.

In the present communication, we have fabricated the Pd/*n*-GaAs devices and hydrogenated them in an atmosphere of molecular hydrogen and studied the electrical (*I–V*, *C–V* and TSCAP) characteristics. It is observed

2. Experimental

The Pd/*n*-GaAs diodes were fabricated on Si doped (~ 10^{16} cm^{-3}), LEC grown *n*-GaAs. The wafers were back contacted with Ni–Ge–Au. The wafers were first ultrasonically cleaned in trichloroethylene followed by acetone and then etched in a solution of $NH_4OH : H_2O : H_2O_2$. Palladium metal films (~ 1000 Å) have been deposited on the top of wafers in a vacuum of ~ 10^{-6} mbar by resistive heating technique. A suitable mask was used to give the diode area of $1·77 \times 10^{-2}$ cm^{-2}. For hydrogenation, the diodes were kept in an evacuated chamber (~ 10^{-4} mbar) and then hydrogen gas was slowly passed into the chamber to achieve a pressure of 1 atm (termed as the adsorption cycle). The transient change in the diode capacitance (at zero bias) in the hydrogen ambient has been monitored at 1 MHz using a Boonton 72B capacitance meter. After the capacitance became constant in the hydrogen ambient, the diodes were exposed to air (termed as the desorption cycle) and the zero bias capacitance was recorded as a function of time. After the diode stabilized in air, the electrical measurements were carried out. The *C–V* measurements were carried out using a HP 4277A multifrequency LCZ meter.

3. Results and discussion

3.1 *Variation in capacitance during adsorption and subsequent desorption*

The variation of capacitance at 1 MHz as a function of time on Pd/*n*-GaAs diode during adsorption and

(region C). During desorption, the capacitance (region D) slowly increases and stabilizes (region E).

The initial increase of the diode capacitance in the hydrogen ambient (peak B) is understood in terms of changes in the work function of the palladium. The hydrogen gas is dissociated and adsorbed at the outer Pd surface. Hydrogen atoms then diffuse through Pd film and are adsorbed at the inner Pd surface. At this surface the adsorbed hydrogen atoms change the work function of this surface due to their dipole moments. The dipole is believed to result from the *S*-type adsorption of hydrogen atom inside the Pd film (Lundstrom *et al* 1975), which reduces the work function (Steele *et al* 1976). Consequently, the barrier height of the Pd/*n*-GaAs initially reduces, giving rise to an initial increase in the diode capacitance (regions A–B, figure 1).

The adsorbed hydrogen, having reached the interface, subsequently diffuses towards the GaAs bulk. The decrease in the diode capacitance after an initial increase is possibly due to the interaction of diffusing hydrogen with the interface and the bulk states. The diffusing hydrogen may induce the compensating interface states, which results in the reduction of diode capacitance. Some of the acceptor states have been identified previously in the hydrogenated devices from the *C–V* studies (Srivastava *et al* 1991).

It is observed that the capacitance becomes constant slowly with time which indicates attainment of a dynamic equilibrium by the device in the hydrogen ambient. The hydrogen diffusion in gallium arsenide may still continue but the changes produced in bulk (far from interface) cannot be monitored by zero bias capacitance measurement. The capacitance voltage measurements at reverse bias would give the information about the changes occurring deep inside the depletion layer towards the bulk of gallium arsenide.

To study the desorption behaviour (regions D–E, figure 1), the device was exposed to air. The adsorbed hydrogen in Pd starts desorbing from the external surface of the palladium. Consequently, hydrogen at the Pd-internal surface tries to diffuse out through its external surface because of concentration gradient of hydrogen (Petersson *et al* 1984). The desorption of hydrogen from Pd layer and from the internal Pd layer in contact with semiconductor would give rise to an increase in the capacitance. However, there is a possible diffusion of bulk hydrogen back to the interface. The hydrogen would stay in a particular region, i.e. interfacial or bulk, depending on the availability for the sites of hydrogen bonding. After few hours the diode capacitance stabilizes in air. The net decrease in the diode capacitance after a full cycle of hydrogenation (adsorption and desorption) from its initial value, A to the final value, E can be attributed to the modifications induced by hydrogen at the interface or the GaAs bulk. The present current–voltage (*I–V*), capacitance–voltage (*C–V*) and thermally stimulated capacitance (TSCAP) studies support this.

3.2 *Current–voltage studies*

The current, *I* flowing through the Pd/*n*-GaAs diodes as a function of voltage (*V*) across it is shown in figure 2, before and after hydrogenation. It is obvious from the figure that the reverse current decreases after
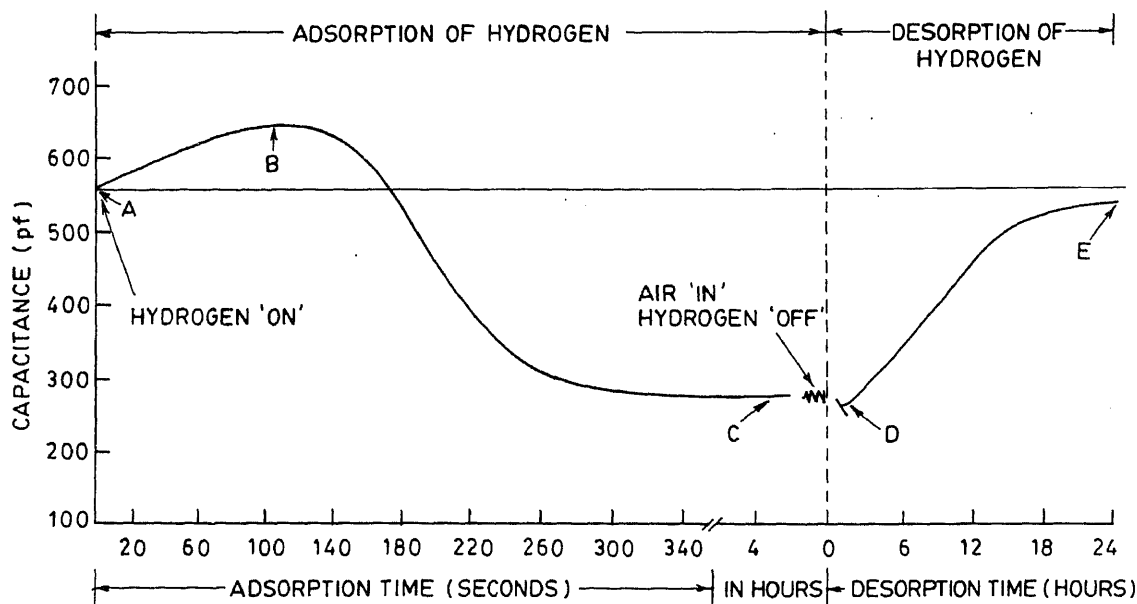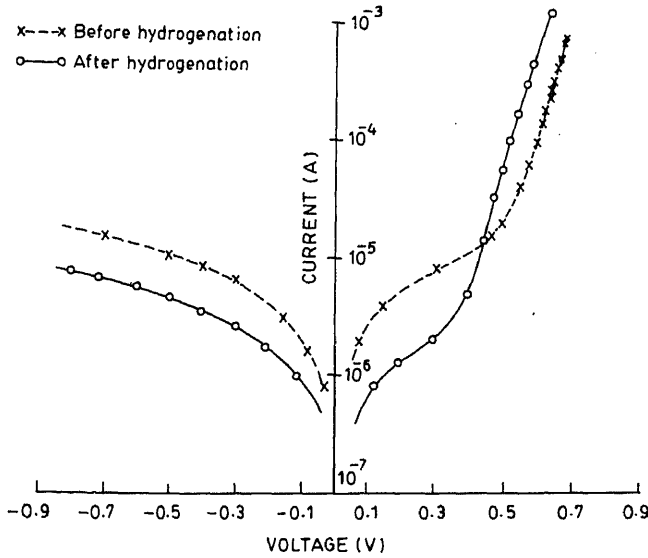
hydrogenation. Figure 2 represents the typical behaviour for the five diodes studied earlier. The ideality factor (η) and the barrier height (ϕ_b) for the devices have been estimated from the *I–V* characteristics (figure 2). For the estimation of ideality factor, the following relation (Sze 1981) has been used:

$$\eta = \frac{q}{kT} \frac{\partial V}{\partial (\ln J)}.$$ (1)

The values of ideality factor are 1·49 and 1·09 for the

Figure 2. *I–V* characteristics of the Pd/n-GaAs diode before and after the hydrogenation cycle.

control (unhydrogenated) and hydrogenated samples, respectively. The change in the ideality factor on hydrogenation shows an improvement of the device. The improvement is related to the passivation of the interfacial states.

The Schottky barrier height can be estimated from the *I–V* studies by using the following relation (Sze 1981):

$$\phi_b = \frac{kT}{q} \ln A^* T^2 / J_0,$$ (2)

where A^* is the effective Richardson constant ($8·6$ Am^{-2} K^{-2}) and J_0 the saturation current density. The image force lowering contribution is neglected. The estimated values of ϕ_b are 0·90 and 0·92 eV for the control (unhydrogenated) and hydrogenated devices, respectively. The increase in the barrier height is known to be related with a decrease in the carrier concentration (Chin-Vincent *et al* 1990).

3.3 *Capacitance–voltage studies*

The capacitance–voltage studies have been carried out at three different frequencies viz. 10 kHz, 100 kHz and 1 MHz. Figure 3 gives the *C–V* (reverse bias) characteristics at three different frequencies. The effective donor density (N_D) has been estimated for the devices using the relation (Sze 1981)

$$N_D = \frac{2}{q \varepsilon_s \varepsilon_0} \frac{dV}{A^2 d(1/C^2)},$$ (3)

where N_D is the donor concentration, ε_0 the permittivity in vacuum, ε_s the dielectric constant of GaAs
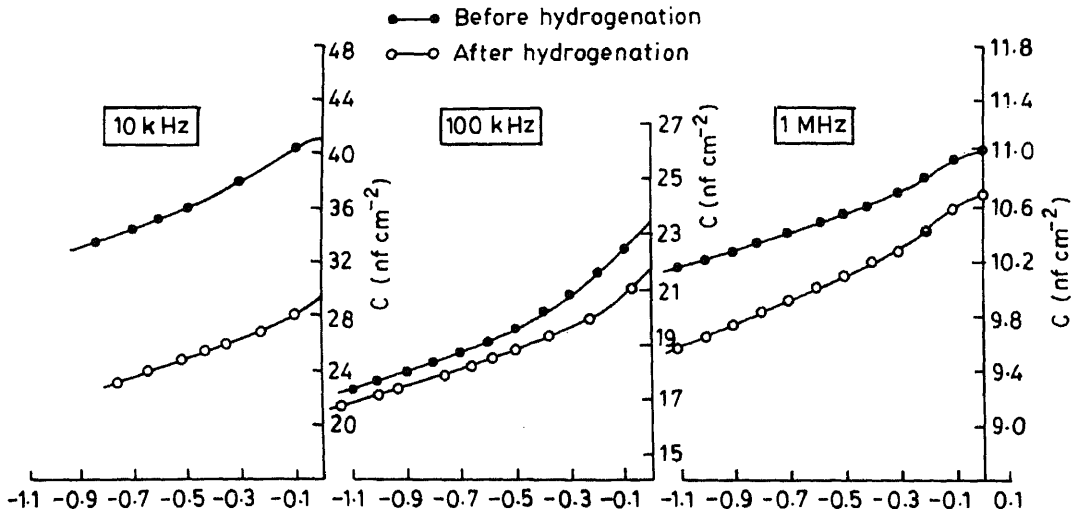
$(\varepsilon_s = 13 \cdot 13)$ and A the area of the diode. The calculated effective donor density (N_D) is given in table 1. Two general conclusions are obvious.

(I) Effective donor density reduces after the hydrogenation at all frequencies. The effective donor density given in table 1 is $N_D + N_{TD}$, where N_D corresponds to the ionized shallow donor density and N_{TD} the deep donor density (Milnes 1973). The reduction in the effective donor density $(N_D + N_{TD})$ after hydrogenation indicates a reduction in N_D or N_{TD} or both of them. The hydrogen passivation of shallow donors and acceptors in GaAs has already been shown by many workers and is reviewed by Pearton *et al* (1992) and Pajot (1988). Passivation of deep states by RF plasma hydrogenation (Jalil *et al* 1989) and low energy hydrogen ions (Bosacchi *et al* 1989) has also been shown.

(II) Measured effective donor density is less at higher frequencies. It is known that ionized deep states (N_{TD}) (Milnes 1973), contribute more at low frequencies. Therefore, the low frequency value of measured effective carrier concentration is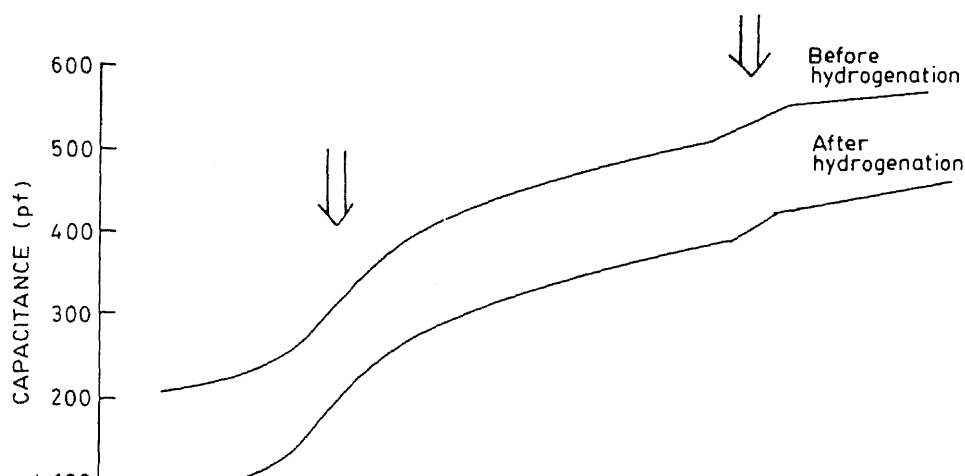 a sum of N_D and N_{TD}. However, N_{TD} does not contribute at high frequencies and it approximates more to N_D and hence will be lower than low frequency value. It can be found out that the value N_{TD} (deep donor density) can now be estimated by taking the difference of effective donor density at high frequency (1 MHz) and that at low frequency (10 kHz). The N_{TD} for the unhydrogenated devices is $2 \cdot 28 \times 10^{16}$ cm^{-3} and $5 \cdot 4 \times 10^{15}$ cm^{-3} for the hydrogenated devices. This shows that there is a density reduction of the deep donor states on hydrogenation which may be due to the hydrogen passivation of deep states. The involvement of such deep states in *n*-GaAs has also been seen by Lagowski *et al* (1982) and Pearton *et al* (1983).
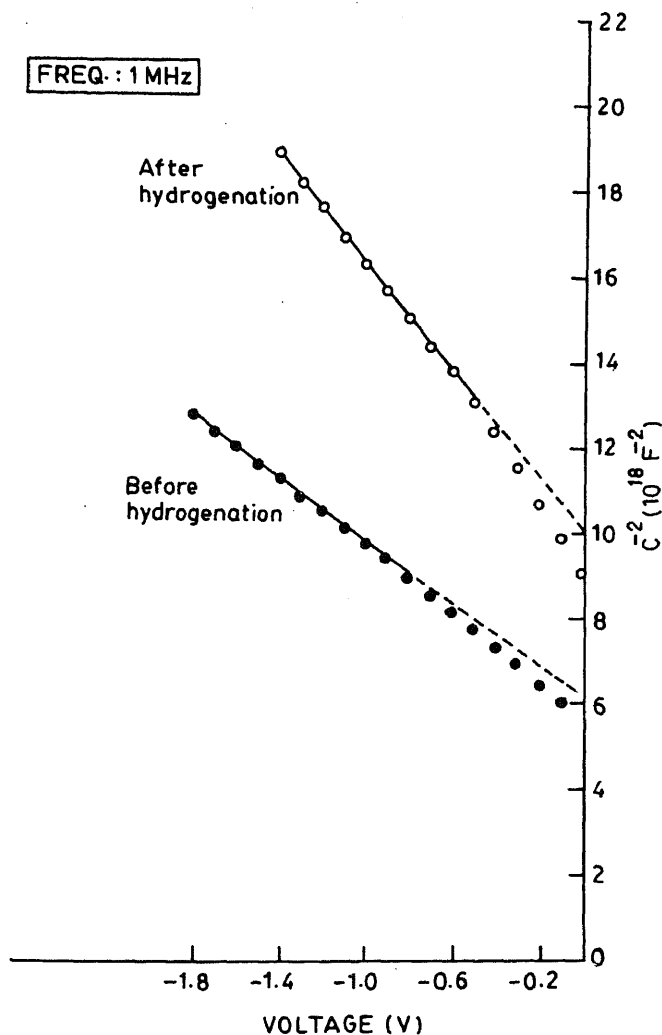
4. Thermally stimulated capacitance (TSCAP) studies

In the present studies, we first filled all the traps by cooling the sample junction to ~ 130 K. Then, a reverse bias (2 V) was applied and the sample was heated up to 360 K at a rate of $\sim 0 \cdot 56$ K/s. The capacitance as a function of temperature during heating cycle is shown in figure 4 for unhydrogenated and hydrogenated devices. The TSCAP curves of figure 4 show two steps in the temperature range as given below:

Table 1. Effective carrier concentration at different frequencies before and after hydrogenation of Pd/*n*-GaAs diodes.

Frequency	Effective carrier concentration (N_D') (cm^{-3})	
	Unhydrogenated	Hydrogenated
10 kHz	$3 \cdot 18 \times 10^{16}$	$1 \cdot 16 \times 10^{16}$
100 kHz	$1 \cdot 80 \times 10^{16}$	$9 \cdot 20 \times 10^{15}$
1 MHz	$8 \cdot 98 \times 10^{15}$	$6 \cdot 20 \times 10^{15}$

	1st step	2nd step
For unhydrogenated	174–228	278–302°K
For hydrogenated	177–225	286–293°K

Further, it is obvious from the above that the temperature range of the capacitance steps are narrower in

From the magnitude of the capacitance step, the trap concentration (N_t) can be calculated using the relation (Buehler and Phillips 1976)

$$N_t \approx 2N_D \left(\frac{C_f - C_i}{C_i} \right), \qquad (5)$$

knowing N_D, N_t can be calculated from the above equation.

To estimate the donor concentration (N_D), C–V measurement was done before and after hydrogenation and $1/C^2$ vs V curve was shown in figure 5. The values of N_D calculated are $4.6 \times 10^{16}\,\mathrm{cm^{-3}}$ and $2.7 \times 10^{16}\,\mathrm{cm^{-3}}$ for the unhydrogenated and hydrogenated devices, respectively. The trap concentrations estimated using above relation are: $4.4 \times 10^{16}\,\mathrm{cm^{-3}}$ and $9.1 \times 10^{15}\,\mathrm{cm^{-3}}$ for the trap energy 0.48 eV and 0.72 eV, respectively for the case of unhydrogenated device and for the hydrogenated device the trap concentration is $3.1 \times 10^{16}\,\mathrm{cm^{-3}}$ and $3.4 \times 10^{15}\,\mathrm{cm^{-3}}$ for the trap energy 0.48 eV and 0.72 eV, respectively.

The observed electron trap with energy 0.72 eV below the conduction band can be related to the well known EL2 defect (Martin *et al* 1977). The electron trap EL2 is a native defect of bulk GaAs crystals, where it occurs in large concentration (up to several $10^{16}\,\mathrm{cm^{-3}}$). Its formation is favoured in materials prepared under As-excess conditions as with LEC bulk crystals (used in the present study). It is ascribed to the As_{Ga} antisite defect, as suggested by many workers (Lagowski *et al* 1982; Schneider 1982; Henine *et al* 1986), but its microscopic nature is still controversial (Bourgoin *et al* 1988; Chang and Chadi 1988). The other electron trap EB6 or E3 $(E = 0.1\,\mathrm{eV})$ is observed by Martin *et al* (1977) and Lang and Kimmerling (1975). Mircea *et al* (1976) suggested that this level might be related to the point defects or point defects/impurity complexes.

It may be noted that the concentration of both the observed states (0.72 and 0.48 eV) is found to be reduced in concentration on hydrogenation showing the partial passivation of these states. Hydrogen passivation of EL2 defect states have also been reported by Lagowski *et al* (1982), Omel'yanovski *et al* (1987) and Kang *et al* (1993) in their study using hydrogen plasma passivation.

Figure 5. $1/C^2$ vs V plot of Pd/n-GaAs diode before and after hydrogenation of the diode for which TSCAP studies are reported.

the hydrogenated case and hence it can be inferred that the distribution of trap/defect states has become sharper after hydrogenation.

The activation energy can be calculated by using the following relation (Buehler and Phillips 1976)

$$E = kT_m \ \ln\left[\frac{\nu k T_m^2}{b(E + 2kT_m)} \right], \qquad (4)$$

5. Conclusions

Current–voltage, capacitance–voltage and TSCAP studies on Pd/n-GaAs diodes are reported before and after the

References

Bosacchi A *et al* 1989 *J. Vac. Sci. Technol.* **B7** 1103

Bourgoin J C, Von Bardeleben H J and Stievenard D 1988 *J. Appl. Phys.* **64** R65

Buehler M G and Phillips W E 1976 *Solid State Electron.* **19** 777

Chang K J and Chadi D J 1988 *Phys. Rev. Lett.* **60** 2187

Chin Vincent W L, Green M A and Storey J W V 1990 *J. Appl. Phys.* **68** 3470

Constant E, Caglio N, Chevallier J and Pesant J C 1987 *Electron. Lett.* **23** 841

Haller E E 1991 *Semicond. Sci. Technol.* **6** 73

Henine M, Tuck B and Paull C J 1986 *Solid State Electron.* **29** 483

Jackson G S, Hall D O, Guido L J, Plano W E, Pan N, Holonyak Jr N and Stillman G E 1988 *Appl. Phys. Lett.* **52** 691

Jalil A, Heurtel A, Marfaing Y and Chevallier J 1989 *J. Appl. Phys.* **66** 5854

Kang T W, Bai H L, Hong C Y, Chung C K and Kim T W 1993 *J. Mater. Sci.* **28** 3423

Lagowski J, Kamnska M, Parsey Jr J M, Gates H C and Lichtnsteiger 1982 *Appl. Phys. Lett.* **41** 1078

Lang D V and Kimmerling L C 1975 *Inst. Phys. Conf. Ser.* **23** 581

Lundstrom L G, Shivaraman M S and Svensson C M 1975 *J. Appl. Phys.* **46** 3876

Martin G M, Mitonneau A and Mircea A 1977 *Electron. Lett.* **13** 191

Milnes A G 1973 *Deep impurities in semiconductors* (New York: Wiley) p. 191

Mircea A, Mitonneau A, Hollan L and Briere A 1976 *J. Appl. Phys.* **11** 153

Myers S M *et al* 1992 *Rev. Mod. Phys.* **64** 559

Omel'yanovski E M, Pakhomov A V and Polyakov A Ya 1987 *Sov. Phys. Semicond.* **21** 514

Pajot B 1988 *Inst. Phys. Conf. Ser.* **95** Ch. 7

Pankove J I and Johnson N M 1991 *Hydrogen in semiconductor: Semiconductor and semimetals* (New York: Academic Press) **34**

Pearton S J, Haller E E and Elliot A G 1983 *Electron Lett.* **19** 1082

Pearton S J, Corbett J W and Stavola M 1992 *Hydrogen in crystalline semiconductor* (Berlin: Springer-Verlag)

Petersson L G, Dannetum H M and Lundstrom I 1984 *Phys. Rev. Lett.* **52** 1806

Schneider J 1982 *Semi-insulating III-V materials* (Evans)

Singh U P, Srivastava P C and Chandra S 1995 *Semicond. Sci. Technol.* **10** 1368

Srivastava P C, Chandra S and Singh U P 1991 *Semicond. Sci. Technol.* **6** 1126

Steele M C, Hile J W and MacIver B A 1976 *J. Appl. Phys.* **47** 2573

Sze S M 1981 *Physics of semiconductor devices* (New York: Wiley)

Tripathi D, Srivastava P C and Chandra S 1989 *Phys. Rev.* **B39** 13420

Tripathi D, Srivastava P C and Chandra S 1992 *Solid State Electron.* **35** 1185

Conducting polymer nanocomposites with extremely low percolation threshold*

B M MANDAL

Polymer Science Unit, Indian Association for the Cultivation of Science, Jadavpur, Calcutta 700 032, India

Abstract. **This article gives a brief review of our work on conducting polyaniline nanocomposites which exhibit extremely low percolation threshold, ca. ~ 0·03 vol.%. The nanocomposites are essentially blends of nanoparticles of HCl doped polyaniline (PANI) with conventional polymers. The nanoparticles (< 20 nm) were prepared by sonicating a suspension of sterically stabilized colloidal PANI particles in solutions of conventional polymers. The sonication process breaks down the stable colloid particles into nanoparticles. The latter are unstable and they aggregate fractally to yield nanocomposites with extremely low percolation threshold.**

Keywords. **Polyaniline; conducting polymers; blends; nanocomposites; nanoparticles; percolation threshold.**

1. Introduction

Conducting polymers (CP) are important emerging materials with the potential of varied applications e.g. in static charge dissipation, electromagnetic shielding, LED displays, gas sensors, biosensors, pressure sensors, corrosion protection of metals and semiconductors, transistors, light weight batteries, etc (Ellis 1986; Garnier 1989). However, many of the conducting polymers are difficult to process because of their insolubility and infusibility. Blending with commodity plastics provides a means of overcoming processing difficulties since the blend can be processed as the matrix polymer. Furthermore, blending reduces the cost of the materials. The cost of the neat materials may be prohibitively high. In this respect lower the CP loading, cheaper will be the blend. Also, blends with low CP loading can be transparent. This property is technologically attractive because it opens up the possibility of using the transparent conducting blends as electrode materials in liquid crystal display devices. They may also find application as hole injecting materials in flexible polymeric LEDs (Heeger et al 1992) and as antistatic coating on microelectronic components. However, blends constituted of randomly dispersed conducting polymer particles fillers in a non-conductive matrix can reach percolation threshold (f_p) at a composition of about 16 vol.% of CP according to the percolation theory (Zallen 1983). Below this critical concentration the blend is an insulator but the conductivity increases sharply at f_p due to the first development of connectivity between the particles in three-dimension

which provides the conducting pathway for the electrical charge carriers. With further increase in concentration of CP more such conducting paths are formed and the conductivity increases. However, the above mentioned concentration is high enough to make the blend non-transparent and cost-ineffective.

Recently, we have used nanoparticles of CPs as particulate fillers in conventional polymers and achieved percolation at extremely low CP concentration ca. 0·03 vol% (Banerjee and Mandal 1995a, b). The fractal aggregation of the unstable nanoparticles has made possible achieving this remarkable result. Our result for polyaniline nanoparticle blends will be presented here.

2. Experimental

Dispersions of polyaniline in water were prepared using the method of oxidative dispersion polymerization of aniline at ~ 0°C in acidic aqueous (1·2 M HCl) medium using ammonium persulfate (APS) initiator oxidant and poly(vinyl methyl ether) (PVME) as polymeric stabilizer (Banerjee et al 1994, 1995). The oblong shaped particles (250 × 190 nm) were isolated by centrifugation and purified by way of redispersion in aqueous HCl followed by centrifugation. For the preparation of the blends the PANI particles as prepared by the above mentioned method were suspended in solutions of conventional polymers in THF, acetone, water etc depending on the solubility of the polymers. The suspension was then placed in a sonicating bath for periods ranging from 1 to 2 h. The resultant dispersions were then cast into films which were formed on evaporation of the
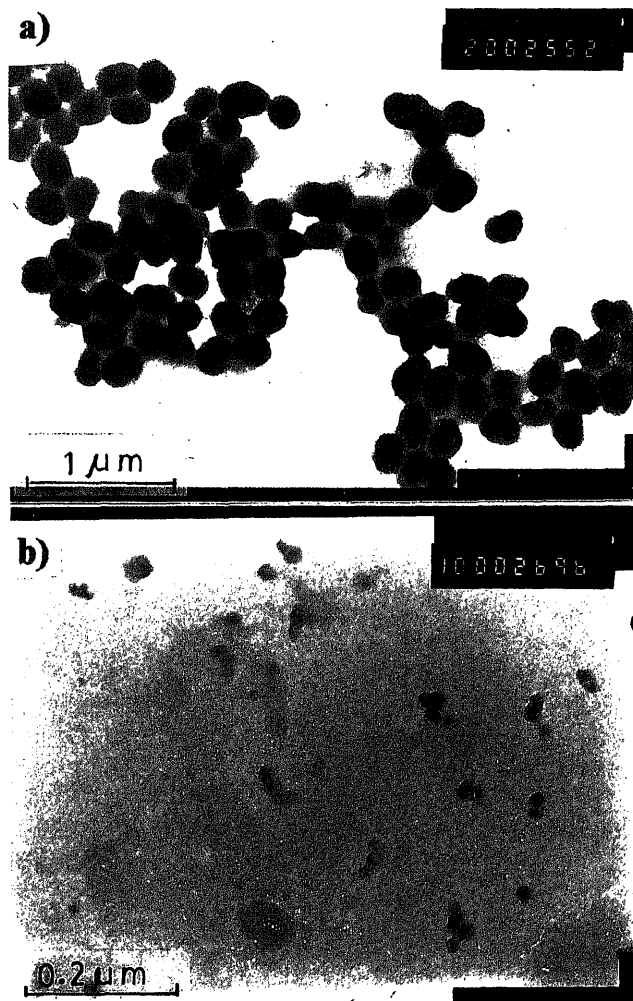
solvent. The blend films thus obtained were dried in vacuum at room temperature (Banerjee and Mandal 1995a, b).

The conductivity of the films was measured by the usual four-probe method. For transmission electron microscopy (TEM), the blend film was cast over carbon coated copper grids from suitably diluted dispersions and examined using a JEOL JEM 100CT electron microscope.

3. Nanoparticles of polyaniline

The polyaniline colloid particles prepared as mentioned above have one remarkable property in that they undergo disintegration when suspension of the particles is sonicated (figure 1). Figure 1a shows the original PANI particles (250×190 nm) and figure 1b shows that the

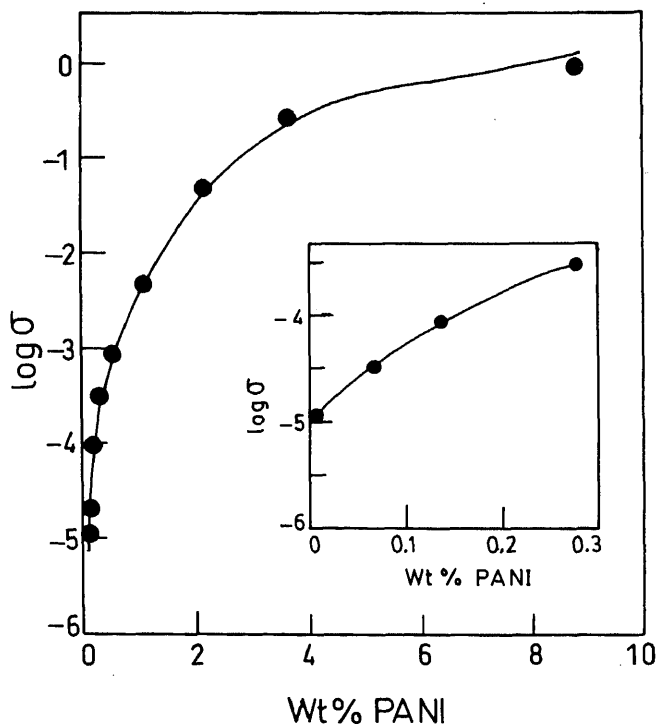particles have been reduced to sizes less than 20 nm following sonication.

4. Blends of polyaniline nanoparticles with conventional polymers

4.1 Electrical conductivity

The electrical conductivity of the blends of the nanoparticles of PANI with conventional polymers when plotted against PANI concentration does not exhibit any well defined percolation threshold as is shown in figure 2 for polyaniline-poly (vinyl alcohol) (PANI–PVA) blends. However, an estimate of the percolation threshold may be obtained by fitting the data used in figure 2 to the scaling law of percolation theory which is as follows (Zallen 1983)

$$\sigma = C\,(f - f_p)^t,$$

where C is a constant, t the critical exponent, f the volume fraction of the filler particles (here PANI), the subscript p signifying percolation threshold. The fitting is shown in figure 3 which yields a value of $3 \cdot 6 \times 10^{-4}$ for f_p and $1 \cdot 96$ for t. For blends using other polymer materials similar f_p and t values were obtained as shown

Figure 1. TEM images of PANI · HCl colloid particles: (a) prior to sonication and (b) 1·5 h after sonication (reprinted with permission from Banerjee and Mandal 1995a; © 1995 American Chemical Society).

Figure 2. Plot of log electrical conductivity vs PANI concentration in PANI–PVA blend films. The inset shows an enlarged view for the low PANI concentration region (reprinted with permission from Banerjee and Mandal 1995a; © 1995 American Chemical Society).

for percolation in three dimension of spherical conducting particles in an insulating matrix.

Previously, Reghu et al (1994) reported conducting polyaniline blends which also have very low f_p (ca. $f_p = 3 \times 10^{-3}$). In contrast to the present method those blends were prepared by the solution blending method. However, in order to make PANI soluble the dopant anion was changed from Cl^- to camphor sulphonate (CSA) (Yang et al 1993). The dispersed PANI·CSA phase in the blends were shown with the help of TEM to have a fractal structure. The latter was presumed to result from the self-assembly of PANI·CSA molecules during liquid–liquid phase separation which occurs on the evaporation of solvent from the solutions of the blends (Reghu et al 1993).

Table 1. f_p and t data for various blends of PANI·HCl with conventional polymers.*

Matrix	$10^4 f_p$	t
PVC	4·02	1·87
PS	4·19	1·91
PVAc	3·18	1·94
PMMA	2·14	1·89
PVA	3·60	1·96

*Reprinted with permission from Banerjee and Mandal 1995a; © 1995 American Chemical Society.
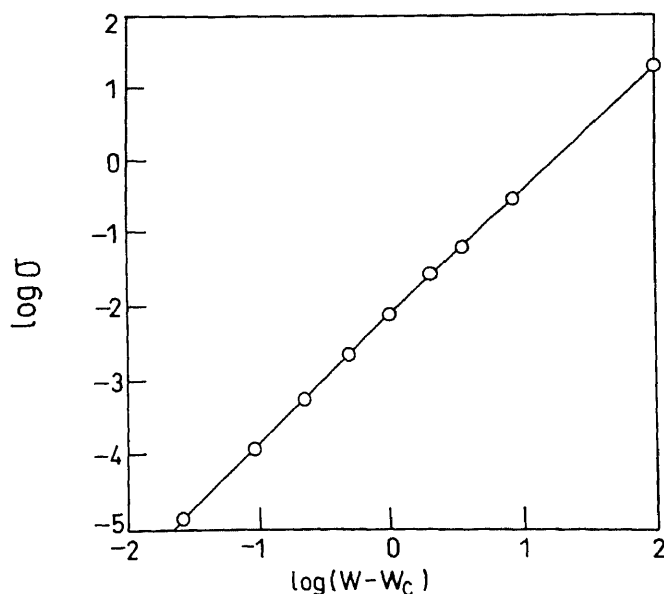
Figure 3. Plot of log conductivity vs log $(w - w_c)$ where w is the wt% of PANI in the blends and w_c that at percolation threshold (reprinted with permission from Banerjee and Mandal 1995a; © 1995 American Chemical Society).

In order to find out the origin of the low f_p in the present blends the morphology of the dispersed PANI phase was studied with the help of TEM. Figures 4a–d show the bright field images of the PANI–PVA blend films containing respectively 0·035, 0·045, 0·05, and 0·5 wt% of PANI. The images show a fibrillar morphology of the dispersed phase. At the lowest PANI loading of 0·035% the PANI nanoparticles are formed to exist in isolated clusters. On increasing the PANI concentration to 0·045% the clusters appear to be weakly interconnected (figure 4b) which indicates that the system is near percolation. The structure is stringy and tenuous at this stage which is the characteristics of percolation threshold. As the PANI concentration is increased further to 0·05% the network becomes more dense. These results thus show that the percolation threshold is somewhere around 0·045% which is in very good agreement with the f_p determined from conductivity studies (figures 2 and 3).

On increasing PANI concentration still further to 0·5% the system is found to undergo self ordering generating a particular pattern for the network which is in the process of formation in figure 4d and near completion in figure 4e. This self-ordering is characteristic of fractal growth (Mandelbrot 1983; Peitgen and Richter 1986). The fractal dimension of the structure shown in figure 4e has been determined to be 1·78 (Mandal 1998). The low percolation threshold is attributed to the fractal growth of the dispersed phase. A fractal object grows faster than an Euclidian object since not every point which is defined by the Euclidian space is occupied in a fractal object.

4.3 Mode of aggregation of nanoparticles

As regards the cause behind the aggregation of the nanoparticles it may be noted that the nanoparticles as produced by the disintegration of the bigger particles do not have enough stabilizer to cover their surface. They are therefore unstable and it is well known that unstable colloid particles undergo fractal aggregation (Forrest and Witten 1979; Weitz and Oliveria 1984; Lin et al 1990). For example, Weitz and Oliveria (1984) found that stabilized gold sols containing particles of ~ 14·5 nm dia. undergo fractal aggregation to form aggregates which have a fractal dimension of ~ 1·75. In the present case for the structure shown in figure 4e, we determined a fractal dimension of 1·78 (Mandal 1997).

5. Conclusion

This study shows that polyaniline nanoparticles can be produced through the disintegration of sterically stabilized
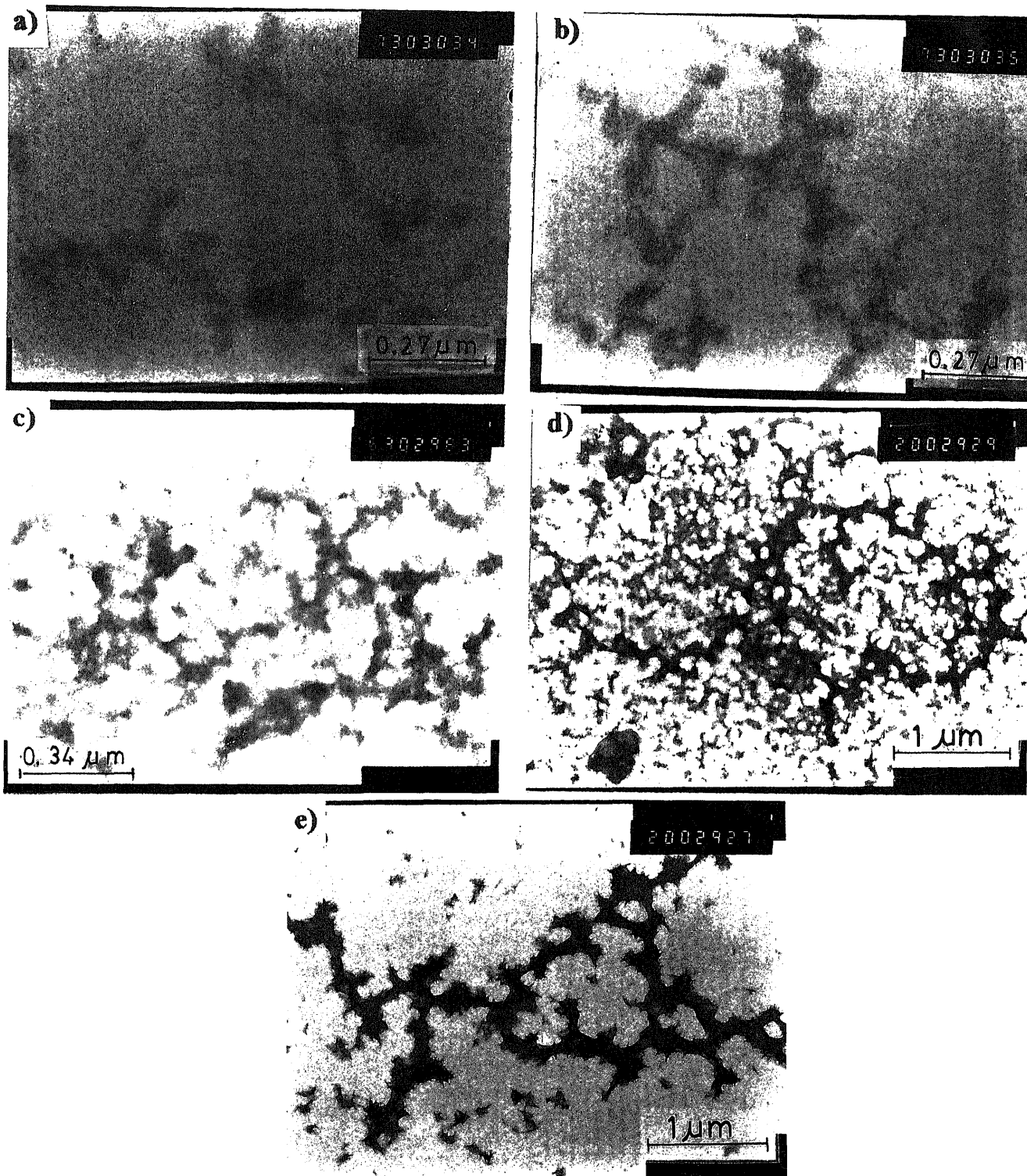
Figure 4. TEM images of PANI–PVA blend films containing different amounts of PANI (in wt%) (**a**) 0·035%, (**b**) 0·045%, (**c**) 0·05%, (**d**) 0·5% and (**e**) 0·5%, but from a different region of the same film as was used for part (**d**) (reprinted with permission from Banerjee and Mandal 1995a; © 1995 American Chemical Society).

polyaniline colloid particles with the help of ultrasound. Nanoparticles produced *in situ* in solutions of conventional polymers undergo fractal aggregation such that the blends exhibit extremely low percolation threshold ($\sim 3 \times 10^{-4}$ volume fraction).

References

Banerjee P and Mandal B M 1995a *Macromolecules* **28** 3940

Banerjee P and Mandal B M 1995b *Synth. Met.* **74** 257

Banerjee P, Digar M L, Bhattacharyya S N and Mandal B M 1994 *Eur. Polym. J.* **30** 499

Banerjee P, Bhattacharyya S N and Mandal B M 1995 *Langmuir* **11** 2414

Ellis J E 1986 *Handbook on conducting polymers* (ed.) T J Skotheim (New York: Marcel Dekker) vol. 1, pp. 489, 501

Forrest S R and Witten Jr T A 1979 *J. Phys.* **A12** L109

Garnier F 1989 *Angew. Chem. Int. Ed. Eng.* **28** 513

Heeger A J 1992 *J. Appl. Phys. Lett.* **60** 2711

Lin M Y, Lindsay H M, Weitz D A, Klein R, Ball R C and Meakin P 1990 *J. Phys. Cond. Matter* **2** 3093

Mandelbrot B B 1983 *The fractal geometry of nature* (New York: Freeman)

Mandal B M 1998 *J. Indian Chem. Soc.* **75**

Peitgen H O and Richter P H 1986 *The beauty of fractals* (Springer)

Reghu M, Yoon C O, Yang C Y, Moses D, Heeger A J and Cao Y 1993 *Macromolecules* **26** 7245

Reghu M, Yoon C O, Yang C Y, Moses D, Smith P, Cao Y and Heeger A J 1994 *Phys. Rev.* **B50** 13931

Weitz D A and Oliveria M 1984 *Phys. Rev. Lett.* **52** 1433

Yang C Y, Cao Y, Smith P and Heeger A J 1993 *Synth. Met.* **53** 293

Zallen R 1983 *The physics of amorphous solids* (New York: Wiley) ch. 4

Infrared and chemical durability studies of some binary PbO and ZnO phosphate glasses and their corresponding sodium metaphosphate derivatives

N ABD EL SHAFI* and S IBRAHIM

Glass Research Department, National Research Centre, Dokki, Cairo, Egypt

Abstract. Structural conclusions are obtained for glasses in the binary PbO and ZnO phosphate systems by IR spectroscopy. Alterations in bands, frequencies and intensities as a function of chemical composition are interpreted and these indicate various types of interlink between Pb^{2+} and Zn^{2+} cations and the host network, especially, when they are incorporated as NWF's. Moreover, the metaphosphate structure, theoretically possible to be achieved in the structure of glasses with equimolar compositions $50M(II)O \cdot 50P_2O_5$ (mol%) (where M is Zn or Pb), is not confirmed by their spectral patterns. However, this structure is confirmed to be achieved in the structure of glasses with $20Na_2O \cdot 30PbO \cdot 50P_2O_5$ and $40Na_2O \cdot 10ZnO \cdot 50P_2O_5$ (mol%). The dissolution rates of most of the studied glasses were measured as a function of pH and variation in chemical composition. The results are discussed in light of the conclusions obtained from the IR study, structural model of phosphate glasses (Van Wazer) and the previously suggested mechanisms for dissolution of phosphate glasses.

Keywords. Glass; phosphate; chemical durability; infrared.

1. Introduction

Among conventional oxide glasses, phosphate glasses are known to have comparatively low softening point but poor chemical durability. The durability of phosphate glasses containing zinc (Holliday 1977; Gray and Klein 1982) and lead (Ray *et al* 1973; Minami and Mackenzie 1977) has been studied in aqueous media. Of all the additions made to phosphate glasses to improve their durability, only PbO lowers the dissolution rate at the same time as it lowers the softening point (Tindyala and Ott 1978).

According to Kordes *et al* (1953) classification for the cations involved in binary phosphate glasses, Pb^{2+} is characterized as a normal cation, while Zn^{2+} is characterized as an anomalous cation. This classification has been made according to the evolution of properties versus the molar content of the cation in glasses. The normal cations lead to linear evolution of properties/composition curves (e.g. density, index of refraction, conductivity, viscosity, durability etc), whereas such curves are nonlinear for the anomalous cations. In the case of Zn^{2+}, the nonlinearity was attributed to a gradual change of the coordination of Zn^{2+}, although the characterization was not found to be an easy matter (Palavit *et al* 1995).

On the other hand, Okura *et al* (1988) built a structural model to explain such nonlinearity, in the case of MgO–P_2O_5 glasses, and attributed it to the coexistence of two structural models at Mg/P = 1 (four-membered rings of PO_4-tetrahedra together with a dimer of PO_4-tetrahedra) rather than coordination variation.

The present paper presents a new view to explain the difference in the way in which both Pb^{2+} and Zn^{2+} cations link themselves to the phosphate network and the reflection of such difference on the chemical durability values of the glasses in both systems.

2. Experimental

2.1 *Preparation of glasses*

Lead and zinc binary phosphate glasses were studied by preparing the glass compositions ranging from $40PbO$ (or ZnO)$\cdot 60P_2O_5$ to $57 \cdot 5PbO \cdot 42 \cdot 5P_2O_5$ and $60ZnO \cdot 40P_2O_5$ in $2 \cdot 5$ mol% stepwise increments. The materials used were reagent grade chemicals of $NH_4H_2PO_4$, Pb_3O_4 and ZnO. Na_2O used in the preparation of glasses in the $xNa_2O \cdot (50-x)PbO$ (or ZnO)$\cdot 50P_2O_5$ ternary systems was added in the form of Na_2CO_3.

Melting was carried out in 50 ml porcelain crucibles. The batches were first heated at 100°C and then at 500°C for several hours prior to melting, in order to

---

*Author for correspondence

167

the last trace of batch was observed to disappear, and annealed at 250–400°C. The variation in the melting and annealing temperatures was in accordance with the glass composition variation. The glasses were stored in desiccator to prevent uptake of moisture.

2.2 FTIR measurements

Dispersions of powdered glass with KBr (1·5%) led to transparent pellets by subjecting them to hydraulic press equal to 2000 kg/cm^2 under vacuum. Transmission spectra were recorded in the range 200–2000 cm^{-1} on a Jasco-300 E FTIR spectrophotometer.

2.3 Dissolution experiments

All samples were tested as powders. They were ground and passed through 45- and 60-mesh sieves. The grains were applied to a magnet to remove any contaminant of iron that may have been introduced during the crushing process. Thereafter, they were cleaned and washed with acetone, methanol and bidistilled water, respectively.

From density measurements it was possible to know the volume corresponding to 2 g of sample, and from the average diameter of grains (ca. 0·03 cm) was obtained their number and the whole surface of the sieved sample.

The effect of six buffer solutions, ranging from 4·3 to 9·0, was studied. To each of the samples was added 100 ml of the freshly-prepared buffer solution at 70°C for 1 h in a sealed polypropylene container. The pH values of the solutions were measured before insertion of the sample and after its removal and the change in the pH was less than 0·2.

After the soak time had elapsed, the grains were washed with acetone and dried in vacuum-tight oven at 120°C to eliminate the residual traces of superficial water. The dissolution rate was calculated from the amount of total weight consumed over the time frame of the experiment and expressed in moles of glass dissolved per cm^2 per min. Each data point on the present curves represent the average of three times experimental repetitions.

3. Results

3.1 IR measurements

For presenting our results and discussion, glasses will be referenced in this paper by their molar fraction ratios, x's, of PbO (or ZnO), in the case of binary systems, and Na$_2$O, in the case of ternary systems. Binary glasses with x values equal to 0·400 and 0·425 were not measured because of the expected difficulties which may arise from their highly hygroscopic nature. Moreover, all the spectra are normalized between 30 and 60 T% at 2000 cm^{-1}.

from 0·450 to 0·575, are displayed in figure 1. Further attempts to produce glasses with higher x values failed; this is consistent with the previous finding of Furdanowicz and Klein (1983).

The compositional range that was studied can be subdivided into two regions according to the intensity in the modification performed on the phosphate network and mirrored by the obtained IR spectra. The first region extends from $x = 0·450$ to $0·500$ and is characterized by subtle changes in the studied domain (200–2000 cm^{-1}) corresponding to stretching modes of PO$_n$ groups ($v > 900$ cm^{-1}), P–O–P bridges (600–1000 cm^{-1}) and bending modes of PO$_n$ (400–600 cm^{-1}) (Rousselot et al 1992). These changes can be summarized as follows: (i) the well-defined peak at 1300 cm^{-1} ($x = 0·450$) is converted to a shoulder in the spectra of the glasses with $x = 0·475$ and 0·500, this is accompanied with a downshift in its frequency value from 1300 to 1295 cm^{-1}; and (ii) the frequencies of the bands at 1185, 870 and 475 cm^{-1}
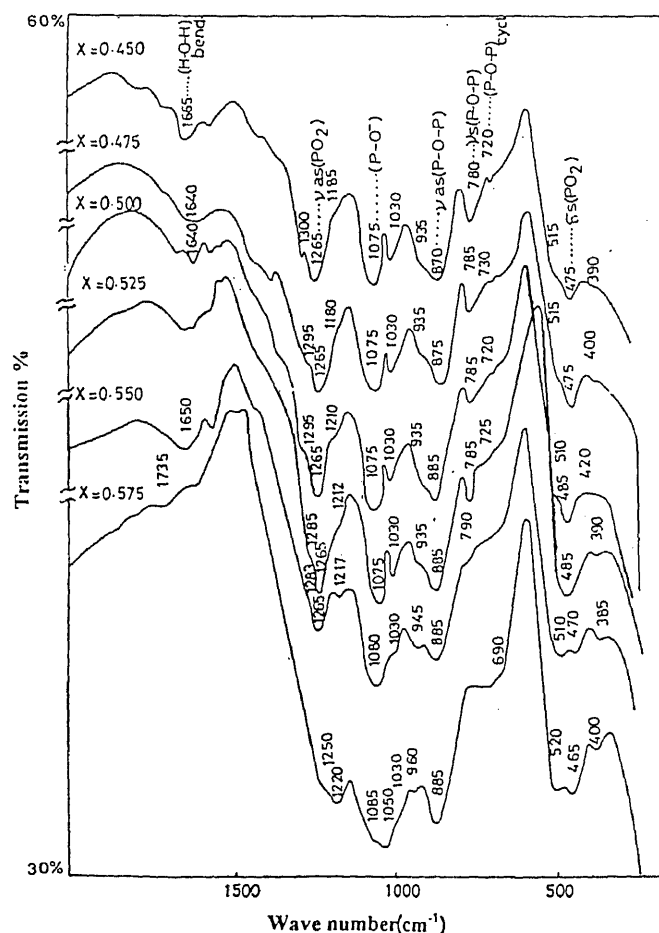
Figure 1. The IR spectra of the binary xPbO$(1 − x)$P$_2$O$_5$ glasses in the range 45–57·5 mol% PbO. (The curves are displaced vertically to avoid confusion).

($x = 0.450$) are upshifted to 1210, 885 and 485 cm^{-1} ($x = 0.500$), respectively.

On the other hand, the second compositional region which extends from $x > 0.500$ to $x = 0.575$ exhibits drastic changes on the IR spectral profiles of the glass samples upon increasing the value of x. The changes can be summarized as follows: (i) the 1300 cm^{-1} band ($x = 0.450$) continues its downshift till it eventually disappears at $x = 0.575$; (ii) the most intensive 1265 cm^{-1} band is weakened and is observed as a shoulder located at 1250 cm^{-1} ($x = 0.575$); and (iii) the appearance of three new bands at 1220, 1050 and 960 cm^{-1} (at $x = 0.550$ and/or 0.575).

3.1b *xZnO·(1 − x)P$_2$O$_5$ system*: The IR spectra of seven members belonging to this system, with x values extending from 0.450 to 0.600, are shown in figure 2. The experimental results shown in this figure can be summarized as follows: (i) the bands at 1275, 1150 and 1090 cm^{-1} show roughly similar intensity behaviours. They decrease and increase with the initial and second rise in x values, respectively, while they decrease with subsequent rises, (ii) the frequencies of the bands at 1340, 1275 and 915 cm^{-1} ($x = 0.450$) are downshifted to 1315, 1265 and 900 cm^{-1} at $x = 0.550$ while they are upshifted to the values of 1335, 1275 and 925 cm^{-1} at $x = 0.600$ and (iii) the intensity of the band at 760 cm^{-1} decreases with the increase in x value till it, eventually disappears at $x = 0.600$. On contrary, the intensity of the band at 725 cm^{-1} increases by the same measure.

3.1c *xNa$_2$O·(0.50 − x) PbO·0.50 P$_2$O$_5$ system*: Figure 3 shows the effect of replacing parts of PbO by Na$_2$O on the IR spectrum of 0.50 PbO·0.50 P$_2$O$_5$ (mol%) glass (i.e. the stoichiometric composition of lead metaphosphate). The observed changes can be summarized as follows: (i) the bands at 1265 and 485 cm^{-1} are intensified along the rise in x value. The intensification is more pronounced with the initial rise in x value, (ii) the disappearance of the shoulder at 1295 cm^{-1} ($x = 0$) in the spectrum of the glass with $x = 0.20$, (iii) the appearance of a new band at 1045 cm^{-1} in the spectra of the Na$_2$O containing glasses and (iv) the well-defined band at 1075 cm^{-1} at
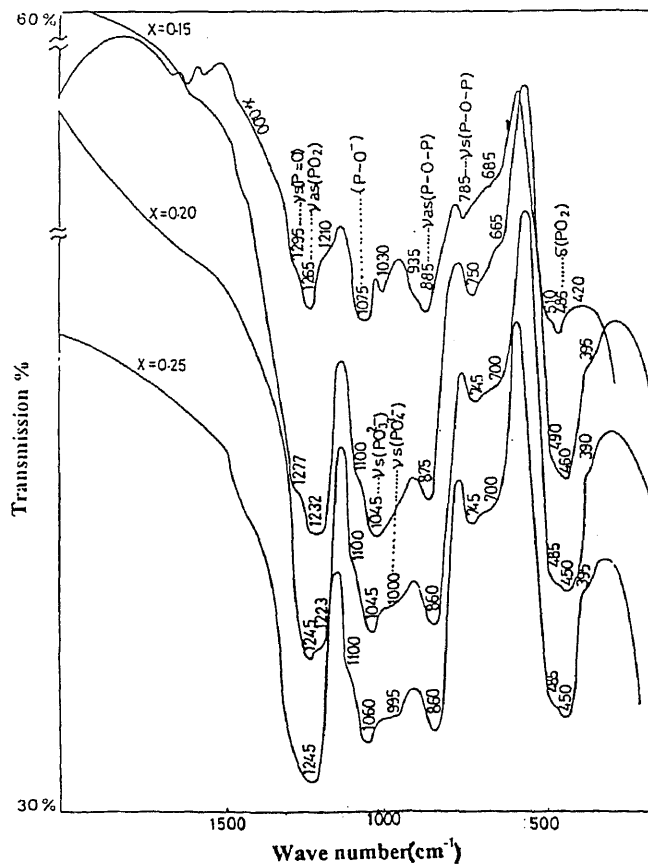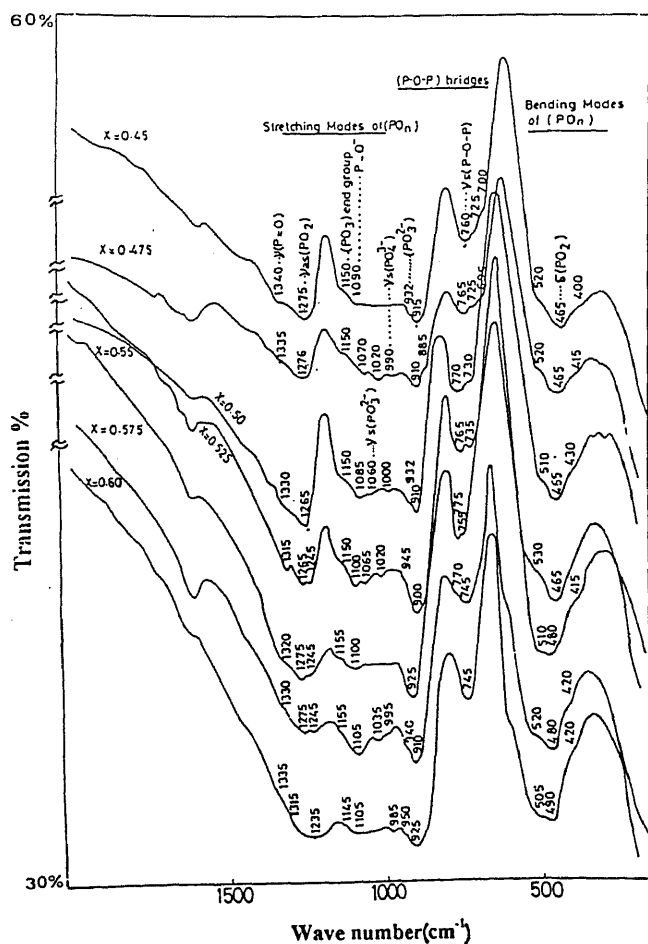
$x = 0$ is upshifted to 1100 cm^{-1} in the rest of the glasses spectra and is identified as a shoulder.

3.1d $xNa_2O \cdot (0.50 - x)ZnO \cdot 0.50 P_2O_5$ system:

The IR spectra of the glasses belonging to this system are shown in figure 4. The experimental observations are similar to those described for the PbO-ternary system except that the present system shows some differences which are summarized as follows: (i) the influence of the initial increase in x values on the spectral profile of Na$_2$O-free glass spectrum is less pronounced, (ii) the disappearance of the band at 1330 cm^{-1}, which is of the same origin as that observed at 1295 cm^{-1} in figure 3 (i.e due to ν (P=O)), is seen to occur at $x = 40$ mol% rather than 20 mol% as in the case of PbO-ternary glasses and (iii) the band which appears at 1045 cm^{-1} in the Na$_2$O-containing glasses of the PbO-ternary system does not appear in the present system.

3.2 Chemical durability

3.2a *Binary lead phosphate glasses*: Leach rates based on total weight loss expressed in (mol glass–cm^{-2}·min^{-1}),
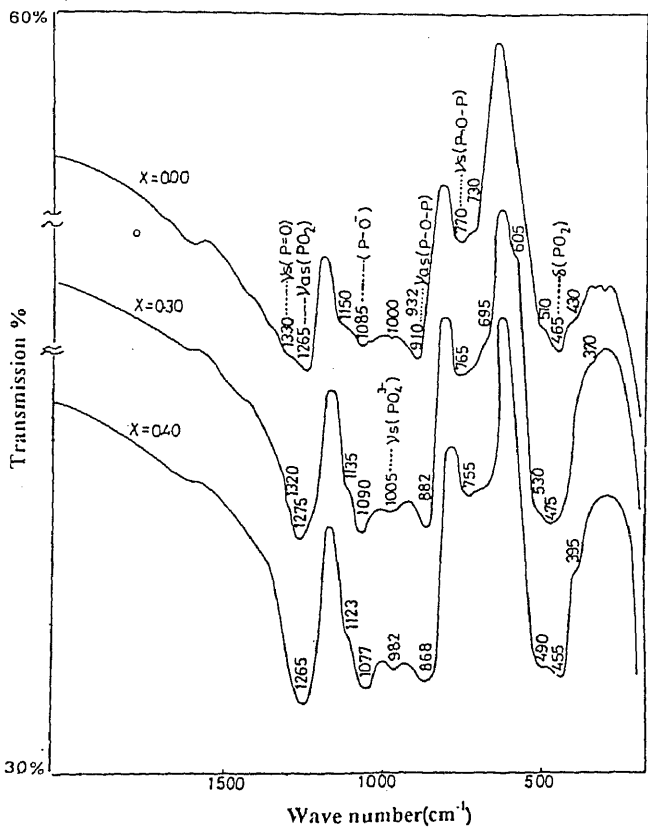
Figure 4. The IR spectra of different compositionally suggested metaphosphates in the system $xNa_2O \cdot (0.50 - x)ZnO \cdot 0.50P_2O_5$. (The curves are displaced vertically to avoid confusion).

are plotted as a function of glass composition variation at different pH values in figure 5. Strong compositional dependences are observed at all pH's except pH 7, where the rates seem to be unaffected by the variation in glass composition. More specifically, the rates show increasing tendencies by a factor of nearly 10, along the rise in P$_2$O$_5$ content from 42·5 to 50 mol%. However, marked decreases in the rates are observed to take place in the solutions with pH < 7 upon increasing the P$_2$O$_5$ content up to 52·5 mol%, followed by a steady increase with further increments in P$_2$O$_5$ content. Because the data obtained for glasses with 57·5 and 60 mol% P$_2$O$_5$ contents are not reliable they are plotted only as examples at certain pH's.

Figure 6 shows the behaviour exhibited by individual glasses when exposed to solutions over the pH range 3·4–9. The obtained results show roughly the same pH dependences for all the studied glasses except those with the lowest P$_2$O$_5$ content. Marked decrease in the chemical durability of the glasses is observed to take place as the pH value increases in the acidic regime, while the chemical durability decreases suddenly as the neutrality point is achieved, further decrease in chemical durability is observed as the pH value is raised to 9·0.

3.2b *Binary zinc phosphate glasses*: Figure 7 shows the effect of variation in the composition of glass on dissolution rates of the glasses included in this system. The leaching behaviour of these glasses follows the same general trends observed for the lead phosphate glasses. This is accompanied by two main differences: (i) the dissolution rates of ZnO-glasses is higher than their corresponding PbO-glasses by a factor of ~ 100 times; and (ii) the minimum which appears in the ultraphosphate compositional range is located at 55 mol% in case of ZnO-glasses rather than at 52·5 mol% in case of PbO-glasses.

Figure 8 shows the change in the dissolution rates of part of these glasses as a function of pH. In contrast to the results obtained for binary lead phosphate glasses, the rates decrease as the pH values of the attacking solutions were increased in the acidic regime, and the rates increase suddenly as the neutral point is achieved. This is followed by a decrease in the rates of the studied glasses as the pH value exceeds 7·0.

3.2c *Ternary $xNa_2O \cdot (0.50 - x) PbO \cdot 0.50 P_2O_5$ system*: The effect of variation in the glass composition on the dissolution rates of the glasses included in this system at three different pH values (pH 3·4, 7 and 9) are depicted in figure 9. The values were selected to explore the effect in the three conventional solutions media (acidic, neutral and basic). Although the dissolution rates of the studied glasses exhibit the same compositional

dependence for all the values of pH's that were studied, the behaviours varied according to the compositional range they are working in. The most characteristic features are: (i) sharp increase in the dissolution rate accompanied with the initial increase in x value (10 mol% Na_2O), and (ii) before the rate continues its steady increase it has been found to be retarded (or slightly decreased) as x approaches the value of 20 mol%.
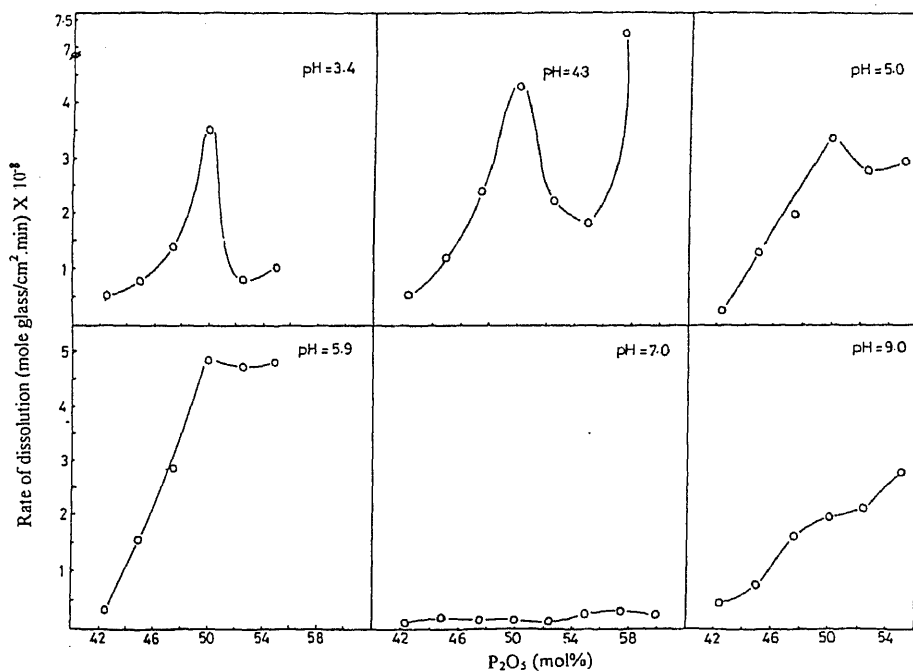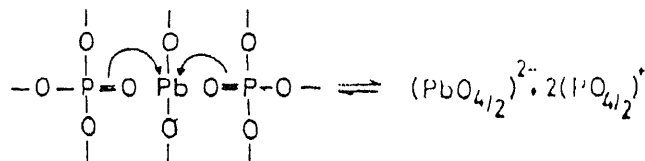

Figure 5. Rates of dissolution of binary $xPbO \cdot (100 - x)P_2O_5$ glasses in different buffer solutions as a function of P_2O_5 content (at 70°C).
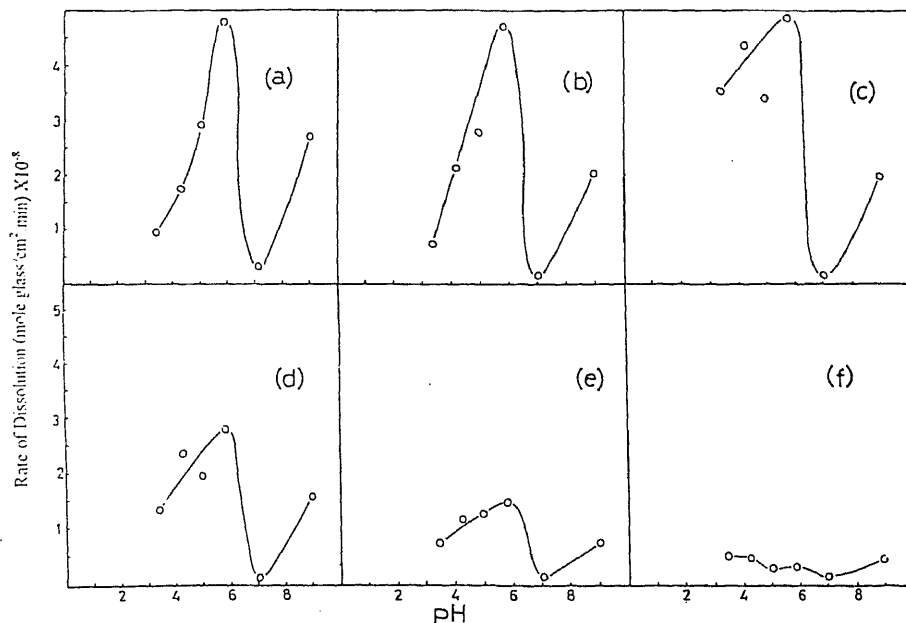
Figure 6. Rates of dissolution as a function of pH values at 70°C for binary lead phosphate glasses of the following P_2O_5 contents (mol%): (a) 55; (b) 52·5; (c) 50; (d) 47·5; (e) 45; (f) 42·5.

forming the so-called iso-silicate structure.

4.1a *xPbO·(1 − x)P$_2$O$_5$ system*: It is conventional to all glass researchers that both PbO and ZnO have the ability to reside in glassy structures either in network-forming or modifying positions. Their incorporations as NWF's is expected to reduce the number of PO$^-$ groups, while their incorporations as NWM's is believed to increase this number. Consequently, the IR bands correlated to such groups should decrease in the former case and increase in the latter. However, the apparent constancy in the intensity and frequency values of the band at 1075 cm^{-1} [v_s(PO$^-$)] in the first compositional range (0·450 ≤ x ≤ 0·500; figure 1) indicates that this group is not involved in the interaction between P$_2$O$_5$ and PbO, on the other hand the changes in the 1300 cm^{-1} band indicate that the P=O (phosphoryl) groups are involved. This may suggest the incorporation of PbO as

Moreover, the apparent constancy in the intensity and frequency values of the 1265 cm^{-1} band [v_{as}(PO$_2$)], as x goes from 0·450 to 0·500, provides an additional support to such conclusion.

Figure 7. Rates of dissolution of binary *x*ZnO·(100 − *x*)P$_2$O$_5$ glasses in different buffer solutions as a function of P$_2$O$_5$-content (at 70°C).
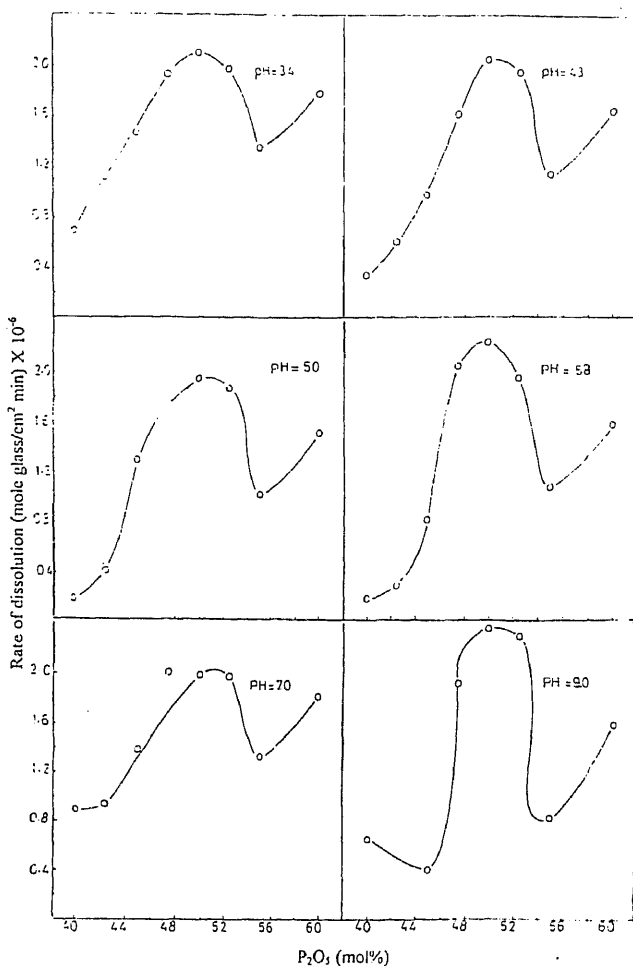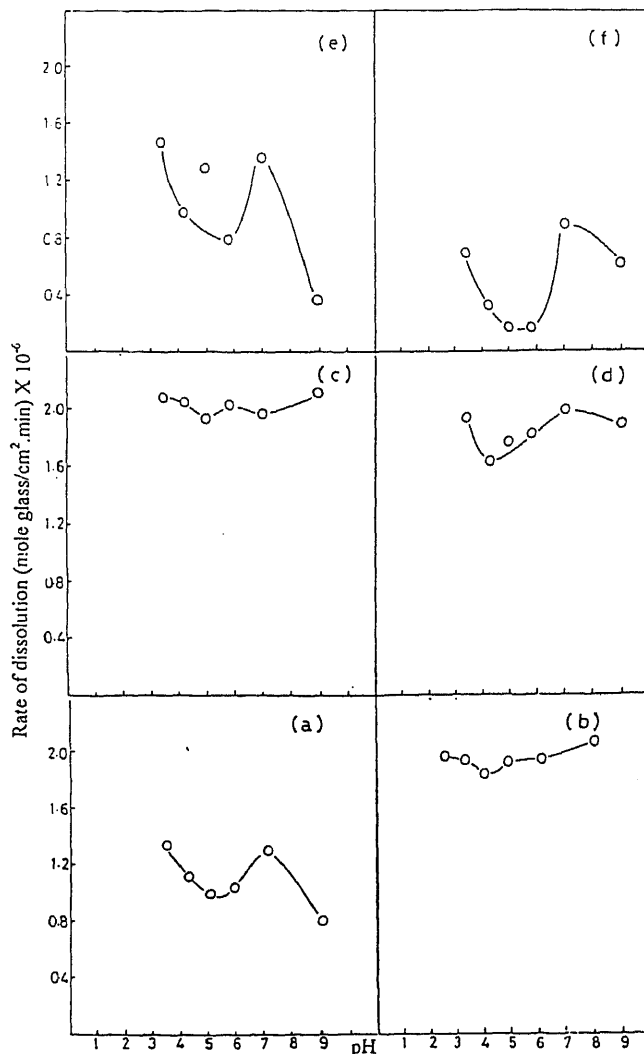
Figure 8. Rates of dissolution as a function of pH values at 70°C for binary zinc phosphate glasses of the following P$_2$O$_5$-contents (mol%) (a) 55; (b) 52·5; (c) 50; (d) 47·5; (e) 45; (f) 40.

The formation of the above structure would result in increasing the network order of polymerization (according to Grimmer and Wolf (1991) notation). This may explain the upshift of the ν_{as} (P–O–P) band from 870 ($x = 0.450$) to 885 cm^{-1} ($x = 0.500$), in an opposite manner to that suggested by Gray and Klein (1989). These authors suggested that this band should shift downward upon crossing the ultraphosphate range towards the metaphosphate composition, since the symmetry of PO$_4$ increases in this direction.

As x exceeds the value of 0.500 (figure 1), the number and intensities of the IR bands change significantly, suggesting, extensive chemical reaction between PbO and P$_2$O$_5$. More specifically, the weakening of the bands at 1265 cm^{-1} [ν_{as}(PO$_2$)] and 780 cm^{-1} [ν_{as}(P–O–P)] reflects the occurrence of continuous structural breakdown, and the 15 cm^{-1} shift of the former band is consistent with the results reported (Kang Sun and Risen 1986; Bruni et al 1994) about vibrational, IR and Raman spectra of phosphate glasses containing chains of variable lengths, with unique difference that occurs here as x goes from 0.550 to 0.575.

The replacement of the 1265 cm^{-1} strong band by new band at 1217–1220 cm^{-1}, reveals (Rousselot et al 1992) that there are, approximately, no more PO$_2$ groups but only PO$_3$ ones which give rise to the latter new line at $x = 0.550$ and 0.575. Furthermore, the presence of new small band at 960 cm^{-1} may be assigned to ν_sPO$_3$ mode of P$_2$O$_7^{4-}$ (Sammet and Brückner 1987). On the other hand, the 1300 cm^{-1} shoulder, which survives up to $x = 0.550$, disappears at $x = 0.575$ reflecting complete delocalization for the π-bonds of the phosphoryl groups in the structure of this glass.

Finally, the metaphosphate structure suggested by the stoichiometric composition of the glass with $x = 0.500$ is not confirmed. This may be attributed to the presence of 1295 cm^{-1} band [ν (P=O)] in the spectral pattern of this glass. In other words, the band should disappear if the metaphosphate structure was achieved (Brow et al 1994).

4.1b $xZnO\cdot(1-x)P_2O_5$ system: The structural changes which occur in these glasses, as the composition is altered can be deduced from the IR spectra shown in figure 2. The changes in the spectral profile accompanied with the rise in x value from 0.450 to 0.475, suggest that Zn^{2+} ions are incorporated mainly as NWF's in this compositional region. This may be manifested by decrease in the intensities of the bands at 1275 [ν_{as} (PO$_2$)], 1150 [ν (PO$_3$)] and 1090 cm^{-1} [ν_s (PO$^-$)] together with the downshift of the latter band to 1070 cm^{-1}. However, the decrease in the intensity ν_s (PO$^-$) band suggests that Zn^{2+} ions interlink themselves to the network through these groups rather than the π-bonds of the phosphoryl groups. The incapability of the Zn ions to make use of π-bonds can be understood on the basis of zinc being regarded as a nontransition element, since it cannot form a compound in which the d-shell is other than full. Thus the possibility of $d\pi$-bonding is very much lowered (Cotton and Wilkinson 1972). Accordingly the following interaction may be suggested:

Figure 2

Rate of dissolution (mole glass/cm^2.min) X 10^{-6}

Na$_2$O.(mol %)

pH=3.4   pH=7.0   pH=9.0
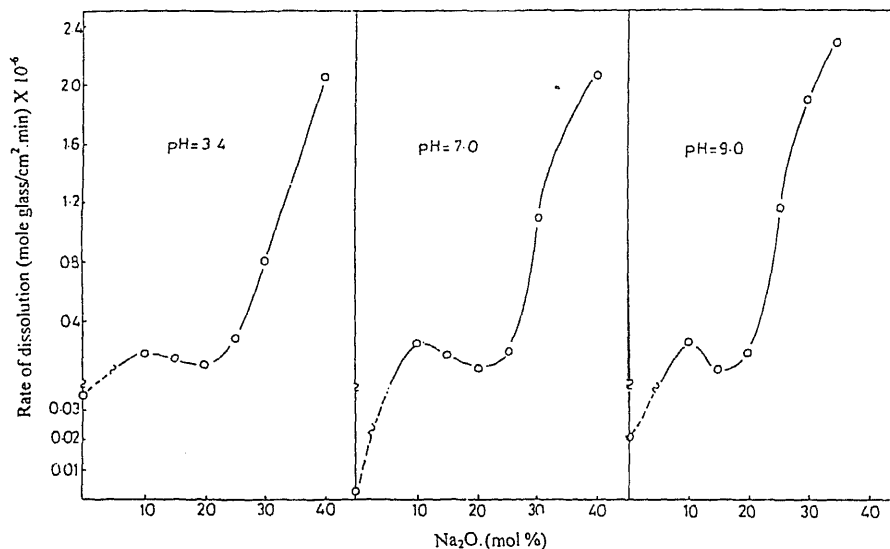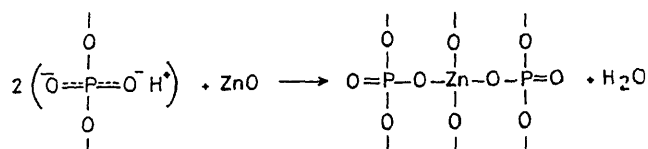
This reaction suggests an increase in the number of the P=O groups, and consequently the water content of the glass should increase. This can be concluded from the intensification of the band ~ 1650 cm^{-1}, attributed to the bending vibrations of H$_2$O molecules.
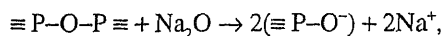
According to Bruni *et al* (1994), the intensity of the ν_{as}(PO$_2$) mode should decrease as we go apart from the metaphosphate composition, i.e. either in the direction of polyphosphates or ultraphosphates. Thus, the unexpected decrease in the intensity of this band (1275 cm^{-1}) as we go from $x = 0.450$ to 0.475 is indicative of the action of ZnO as NWF.

On the contrary, the significant increase in the band intensity at 1276 and 1070 cm^{-1} ($x = 0.475$) together with the upshift of the latter band as x goes from 0.475 to 0.500 is indicative of the action of ZnO as NWM. The depolymerization of the network results in the generation of increasing number of NBO's. The increase in such number per phosphate tetrahedra, increases the capability of phosphorous ions to compensate their high positive charges by performing closer coordination to their next nearest neighbour NBO's. This may be the cause of the observed 30 cm^{-1} shift of the ν(PO$^-$) band as x goes from 0.475 to 0.525.

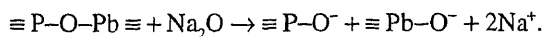Moreover, the increase in the band intensity at 745 cm^{-1} due to (P–O–P)$_{cycl.}$ is at the expense of that at 770 cm^{-1} due to ν_s(P–O–P) which marks the formation of increasing amounts of structures. The formation of such ring structures results in the polymerization of PO$^{(-)}$ groups, which increase the probability of localized double bond formation. This may account for the upshift of the P=O (1315–1335 cm^{-1}).

Finally, the metaphosphate structure which has not been confirmed in the case of PbO is neither confirmed in the present case due to the presence of the band at 1330 cm^{-1} [ν(P=O)] in the spectral pattern of the $x = 0.500$ glass.

4.1c $xNa_2O \cdot (0.50 - x)PbO \cdot 0.50P_2O_5$ *system*: The replacement of PbO by Na$_2$O is expected to increase the order of depolymerization of the network by creating increasing number of NBOs. Such creation can be manifested by the sharp increase in the intensities of the bands at 1265 [ν_{as}(PO$_2$)] and 480 cm^{-1} [δ_{as}(PO$_2$)], the upshift of the 1075 cm^{-1} band to 1100 cm^{-1} [ν_s(PO$^-$)], and the appearance of the new band at 1045 cm^{-1} [ν_s(PO$_3^{2-}$)] (see figure 3). The formation of the NBOs is assumed to occur according to the following two reactions:

$$\equiv P-O-P \equiv \; + \; Na_2O \rightarrow 2(\equiv P-O^-) + 2Na^+,$$

or

$$\equiv P-O-Pb \equiv \; + \; Na_2O \rightarrow \; \equiv P-O^- + \equiv Pb-O^- + 2Na^+.$$

The second reaction is believed to be more favoured

polarizable than those in the (P–O–P) units, and hence their bonds are more susceptible to be broken.

The disappearance of the 1295 cm^{-1} band [ν(P=O)] in the spectrum of the glass with $x = 0.20$ suggests the conversion of the three-dimensional network to one-dimensional network. In other words, the metaphosphate structure, which has not been confirmed by the structure of the 50PbO·50P$_2$O$_5$ (mol%) glass, is established (i.e. Q^2-moieties dominate). Moreover, the two bands which appear at 1045 and 1000 cm^{-1} reflect the formation of pyrophosphate and orthophosphate units (Tatsumisago *et al* 1988), respectively. The decrease in the intensities of these two bands, as x exceeds 0.15, seems to be parallel to the increase in the intensity of the shoulder at 700 cm^{-1}. This reveals that the increase in the amount of cyclic structures is mainly performed at the expense of the low-molecular-weight molecules (e.g. pyro- and orthophosphates).

4.1d $xNa_2O \cdot (0.50 - x)ZnO \cdot 0.50 P_2O_5$ *system*: Because of the similarity between the changes in the IR spectra of the PbO-ternary system (figure 3) and the present system (figure 4), the same discussion carried out previously can be reported here. However, the differences are presented as follows: (i) the metaphosphate structure (built up as infinite PO$_4$-tetrahedral chains) is established at $x = 0.40$ rather than at 0.20 in the previous system, (ii) the comparison between the area of ν_{as}(PO$_2$) band in both the systems suggest shorter metaphosphate chains in the present system. This can be attributed to the higher field strength of Zn^{2+} cations as compared to Pb^{2+} cations (Bartholomew 1972), and (iii) the pyrophosphate groups are not observed to exist in the present case.

4.2 *Chemical durability*

4.2a   *The effect of composition*: Chemical durability results can be discussed on the basis of the polymeric structural model of phosphate glasses suggested by Van Wazer (1951). Accordingly, the basic unit is the tetrahedral PO$_4$ group which can be bonded to a maximum of three neighbouring groups through bridging oxygens. The addition of modifier oxides disrupts the bridging (P–O–P) bonds and lowers the number of bridging PO$_4$ tetrahedra.

In polyphosphate region (P$_2$O$_5$ < 50 mol%), glasses are considered to be composed of unbranched polymer of variable chain lengths. The average length of the chains increases with increasing P$_2$O$_5$ content of the glasses. However, since the mechanism of hydrolysis comprises the rapid suspension of intact polymers in aqueous solutions, the shorter the chains the easier their dissolution (i.e. glass compositions with higher P$_2$O$_5$ contents, with longer chains, will have improved chemical durabilities

In contrast to the above point of view, Dickenson (1994) suggested, on the basis of the stability constant criterion, that glass compositions with lower P_2O_5 contents (i.e. shorter chains) will have improved chemical durabilities. This is built on the fact that the stability constants increase in the direction meta- < tetra- < tri- < pyro- < orthophosphates. However, the present results in both cases of PbO-binary glasses (figure 5) and ZnO-binary glasses (figure 7), in the region $P_2O_5 \leq 50$ mol%, are consistent with Dickenson's point of view. Fortunately, similar behaviour has been obtained previously (Furdanowicz and Klein 1983) upon subjecting binary lead phosphate glasses to the action of water at ambient temperature. The results were explained on the basis that PbO has a dramatic effect on the rate of dissolution of phosphate glasses as it apparently behaves as network-former with respect to the dissolution of the glass in solutions, cross-linking the relatively inert polyphosphate polymers into a very durable network.

As P_2O_5 contents exceed 50 mol%, branching tetrahedra are introduced, serving as steric hindrance to the diffusion of the attacking species into the glass and, consequently, lower the rates of dissolution (figures 5 and 7). However, as the fraction of branching PO_4 tetrahedra increases, good deal of strain is introduced into the network which encourages the hydrolytic cision of these branching units, leading to an increase in the rates of dissolution.

The minimum corresponding to the lowest dissolution rates in the ultraphosphate region was predicted (Bae and Weinberg 1994) to be, at approximately, 60 mol% P_2O_5. The ability of both Pb^{2+} and Zn^{2+} cations to act as NWFs increases the real value of Q^3/Q^2 over the theoretical one calculated from the following equation.

$$^fQ^3/Q^2 = \frac{1 - 2x}{x},$$

where x is the mole fraction of the modifying oxide in the ultraphosphate region of a binary glass.

This may be the reason which stands behind the appearance of such minimum at 52·5 and 55 mol% P_2O_5 in the cases of binary PbO glasses and ZnO glasses (figures 5 and 7), respectively.

4.2b *The effect of pH:* The dissolution of most phosphate glasses is governed by the 'hydration mechanism', which includes the protonation of the phosphate chains, in acidic solution, and disruption of the cross-links between them via the following chemical reaction:

$$\begin{array}{ccc} O & & O \\ | & & | \\ =O-P-OM + H^+ \rightarrow & =O-P-OH + M^+ \\ | & & | \\ O & & O \end{array}$$
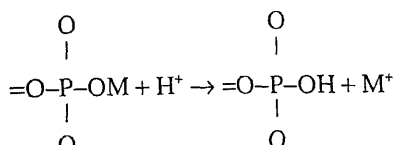
what is called 'uniform dissolution'. It is obvious that the rate of such dissolution is accelerated with the rise in (H^+).

Although this acceleration is confirmed by the results obtained in the case of ZnO-binary glasses (figure 8), in the acidic regime, it is not confirmed by those obtained in the case of PbO-binary glasses (figure 6). This does not conclusively suggest that the hydration mechanism is invoked. Repeatedly, such unusual behaviour may be attributed to the partial action of PbO as network-former. In this case, the P–O–Pb bond has some covalent characteristics. Thus, the ion exchange process, between H_3O^+ and the Pb^{2+} cations located between phosphate chains, is thermodynamically less favourable (Peng and Day 1991). This may indicate that the above hydration reaction is not the rate determining step governing the dissolution of the phosphate network.

On the other side, the increase in rates of the ZnO-binary glasses (figure 8) upon achieving the neutrality point represents another unusual behaviour. This may be attributed to the increase in the water content in the structure of the glasses as a consequence of the increase in the P=O groups upon the incorporation of the ZnO as NWF and the formation of cyclic structures as has been concluded from the IR study.

Although Zn^{2+} possesses higher field strength than Pb^{2+} and is assumed to express greater blocking effect to the glass structure, the obtained results reveal opposite trend. More specifically, the dissolution rates of the ZnO-binary glasses are higher than their corresponding PbO ones by ~ 100 times. This may be referred to the following two reasons.

First, the hydration mechanism is most likely controlled by two factors: (i) the bond strength of the cross-link between modifier cation and phosphate chain, and (ii) the affinity of the cation to water. According to the first factor, the hydration in the case of Pb^{2+} is expected to be easier than in the case of Zn^{2+} because of its lower field strength which leads to a weaker bond strength. However, in hydration reaction, ion–dipole (Pb^{2+}- or Zn^{2+}-H_2O) interaction plays an important role in determining how soluble an ionic compound will be in solution. Zn^{2+} cation has a greater electrostatic interaction with water than Pb^{2+} since it is smaller in size and its charge is more concentrated. Thus, Zn^{2+} cation possesses higher in-dipole interaction. The obtained results suggest more importance for second factor than the former one.

Secondly, the ability of Pb^{2+} cations to link themselves through the π-bonds of the phosphoryl groups, thus building a network which mimics that of silicate glasses, together with the incapability of Zn^{2+} cations to make such compact structure as has been seen from the dis-

equimolar PbO–P$_2$O$_5$ glass accompanied with the initial 10 mol%, replacement of Na$_2$O for PbO (figure 9) may be attributed to the relieving of the previously suggested silicate like structure. This suggests the preference of the second reason over the first one.

On the other hand, the above behaviour is followed by a slight decrease in the dissolution rates accompanied by the second replacement of Na$_2$O for PbO, exhibiting a minimum at $x = 0.20$. This composition (20Na$_2$O·30PbO·50P$_2$O$_5$) resembles that suggested from the IR study to achieve the ideal metaphosphate structure. This structure has supposedly improved chemical durability. Although further replacements of Na$^+$ (low field) for Pb^{2+} (high field strength) would result in increasing the lengths of the metaphosphate chains (Bartholomew 1972) no further decrease (or retardation) to the increase in rates are observed. This may indicate that such elongation in chain lengths cannot withstand the effect of replacing monovalent cations (Na$^+$) for divalent cations (Pb^{2+}) anymore.

5. Conclusion

The results show that the dissolution rates of the binary zinc phosphate glasses are higher than their corresponding lead glasses by about 100 times. Such difference in the dissolution rates of the glasses in both systems was destroyed by replacing 10 mol% Na$_2$O for PbO in the 50PbO·50P$_2$O$_5$ (mol%) glass composition. The results could not be correlated to the difference in the field strengths of the Pb^{2+} and Zn^{2+} ions. They were rather correlated, according to the IR results, to the difference in which both cations interlink themselves to the phosphate network when they are incorporated as NWFs. Moreover, Pb^{2+} cations exhibit the ability to form compact iso-silicate structure, while Zn^{2+} cations do not.

References

Bae B S and Weinberg M C 1994 *Glass Technol.* **35** 83
Bartholomew R F 1972 *J. Non-Cryst. Solids* **7** 221
Brow R K, Tallant D R, Hudgens J J, Martin S W and Irwin A D 1994 *J. Non-Cryst. Solids* **177** 221
Bruni S, Cariati F and Narducci D 1994 *Vibrat. Spectrosc.* **7** 169
Cotton F A and Wilkinson G 1972 in *Basic inorganic chemistry* (New York: Wiley Eastern Ltd.)
Dickinson J E 1994 *Chimica Chronica, New Series* **23** 355
Furdanowicz W and Klein L C 1983 *Glass Technol.* **24** 198
Gray P E and Klein L C 1982 *Glass Technol.* **23** 177
Gray P E and Klein L C 1983 *Glass Technol.* **24** 202
Gray P E and Klein L C 1989 *J. Non-Cryst. Solids* **68** 75
Grimmer A R and Wolf G U 1991 *Eur. J. Solid State Inorg. Chem.* **28** 221
Holliday L 1977 *J. Polym. Sci.* **15** 675
Kang Sun and Risen W M Jr 1986 *Solid State Commun.* **60** 697
Kordes E, Vogel W and Feterowsky R 1953 *Zeit. Elektrochemie* 282
Minami T and Mackenzie J D 1977 *J. Am. Ceram. Soc.* **60** 232
Okura T, Yamashita K and Kanazawa T 1988 *Phys. Chem. Glasses* **29** 13
Palavit G, Montagne L and Delaval R 1995 *Proc. XVII int. congress on glass, Beijing, PR China* (Beijing: Chinese Ceramic Society)
Peng Y P and Day D E 1991 *Glass Technol.* **32** 200
Ray N H *et al* 1973 *Glass Technol.* **14** 50
Rousselot C, El Rhess E, Malugani J P, Mercier R, Mercier M F and Kishioka A 1992 *Solid State Ionics* **58** 71
Sammet M and Brückner R 1987 *Glasstech. Ber.* **60** 55
Selvaraj U and Rao K J 1988 *J. Non-Cryst. Solids* **104** 300
Tatsumisago M, Kowada Y and Minami T 1988 *Phys. & Chem. Glasses* **29** 63
Tindyala M A and Ott W R 1978 *Am. Ceram. Soc. Bull.* **57** 432
Van Wazer J R 1951 in *The phosphorous and its compounds* (New York: Interscience)

Compaction behaviour of plaster of Paris dewatered- and air dried-Nigerian clay

C S NWOBODO

School of Engineering and Engineering Technology, Federal University of Technology, P.M.B. 1526, Owerri, Imo State, Nigeria

Abstract. The effects of compaction pressure on the green bulk density and porosity of Nigerian clay were examined over a range of pressure from 47·2 to 157·3 MPa. An exponential behaviour was found between pressed relative density and compaction pressure, the logarithm of relative density increasing with compaction pressure.

An exponential behaviour was also found between compaction pressure and true porosity, the latter decreasing as the logarithm of compaction pressure increased.

Finally, empirical equations relating to true porosity and compaction pressure and also the relationship between relative density and compaction pressure, are presented.

Keywords. Compaction behaviour; plaster of Paris; Nigerian clay.

1. Introduction

The compaction behaviour (Dynys and Halloran 1983) of ceramic powders is strongly influenced by the state of agglomeration of the powder. With increasing applied pressure the density of the powder column will increase, or its porosity will decrease. Several workers (Yu Balshin 1938; Seelig and Wulff 1946; Bockstiegel and Hewing 1965) have studied the relationship between applied pressure and the density or porosity of powder compact, and have attempted to establish mathematical relationships between pressure and average relative density. For dry compaction of nonplastic materials, the agglomerate state of primary industrial relevance involves nonaggregated powder agglomerated into powder free-flowing granules by spray-drying with a binder. Clay in itself has binding characteristics.

The object of this study is to investigate the effect of compaction pressure on the green bulk density and true porosity of Nigerian clay* suitable for refractory brick manufacture.

2. Experimental

The clay used in this study consisted basically of clay substance, vegetable matter and free silica. The as-received clay was wet-sieved to pass 200 mesh. The resulting slip was allowed to settle for 48 h and the supernatant liquid decanted. The slurry was then dewatered on a plaster of Paris bat and dried in air to a leather-hard condition. The resulting lumps were crushed to powder containing 2·3% moisture.

The clay powder was compacted using a 19 mm internal diameter steel die and punch set. The punch and die were lubricated with engine oil to lessen die-wall friction effects. Compaction was performed on a Buehler Ltd laboratory mounting press at pressures of 47·2, 62·9, 94·4, 110·1, 125·8, 141·5 and 157·3 MPa. Ten clay discs were compacted at each pressure.

The true specific gravity of the clay powder was determined by the evacuation method (Chesters 1974). Three concordant readings were obtained and an average value taken.

The green bulk density and apparent porosity of the clay compacts were determined by evacuation method with kerosene as the liquid medium. The bulk density, D was calculated using the relationship:

$$D = \frac{W_d}{W_s - W_p} \times D_s ,$$ (1)

where W_d is the dry mass, W_s the soaked mass, W_p the suspended mass and D_s is the density of the liquid medium.

The apparent porosity (AP), was calculated using the relationship:

$$AP = \frac{W_s - W_d}{W_s - W_p} .$$ (2)

The true porosity (TP), was also calculated using the relationship:

---

*Clay is from Afikpo in Abia State of Nigeria.

D the density of compact at pressure, P and D_0 the true density of the clay powder.

The D/D_0 and P values obtained in this study were highly correlated. A plot of $\ln D/D_0$ vs P could be fit by a straight line with a regression coefficient of 0·9862. Increasing the compaction pressure from 47·2 to 157·3 MPa increases the bulk density from 72 to 81% of the theoretical density.

Again, increasing the compaction pressure from 47·2 to 157·3 MPa decreases the true porosity, expressed as a volume fraction, from 0·278 to 0·190. This allows the bulk of the compaction data, from 0·278 to 0·190 true porosity, to be represented simply by the empirical equation:

Table 2. Effect of compaction pressure on green porosity.

Designation	Compaction pressure (MPa)	No. of specimens	Average green porosity (vol. fraction)	Standard deviation
P1	47·2	10	0·278	0·0049
P2	62·9	10	0·256	0·0039
P3	94·4	10	0·242	0·0021
P4	110·1	10	0·214	0·0025
P5	125·8	10	0·203	0·0020
P6	141·5	10	0·196	0·0044
P7	157·3	10	0·190	0·0033

$$P = P_0 \exp(-bp), \tag{5}$$

where P is the compaction pressure, P_0 the compaction pressure at zero porosity, b the empirical slope which is a constant for the material and p the volume fraction porosity. The straight line obtained from a semilogarithmic plot of pressure, P vs volume fraction porosity, P has a regression coefficient of 0·9831. This suggests that the pressure–porosity relationship is well correlated. This is anticipated by the Duckworth (1953) equation in the discussion of Ryshkewitch's paper.

However, it should be noted that the mechanics of dry powder compaction is complex in its details (Broese Van Groenau 1981), and unclear in its foundations (Onoda and Urban 1978), and therefore all equations must be considered empirical rather than based on the principles of mechanics. Nevertheless they are quite useful for the purpose of interpolating green densities and/or porosities as a function of compaction pressure.

The effect on green density and porosity of compaction pressures less than 47·2 MPa and greater than 157·3 MPa, was not investigated in this study. The extrapolated density is 1·79 g cm⁻³ as against the tap density 1·31 g cm⁻³. It is anticipated that the porosity will increase exponentially with a decrease in compaction pressure.

When semidry powders are pressed, there must be incomplete transmission of pressure because a proportion of the thrust is taken up in overcoming the friction the

grains exert on each other and on the sides of the die. Shaxby and Evans (1923) have shown that the pressure decreases with the distance from the surface layer at a rate directly proportional to the coefficient of friction of the particles on the walls of the die and to the externally-applied pressure but inversely proportional to the radius of the die (assumed cylindrical).

Consequent on this pressure gradient, the bulk density in the pressed compact must vary with the depth, in accordance with the logarithmic relationship already established.

The apparent porosity of sintered firebricks varies from 9% (very low) to 22·5% while the bulk density varies from 1·96 to 2·36 g cm^{-3}. From the compaction data, a suitable compaction pressure corresponding to a given green bulk density or porosity of refractory bricks made from the clay used in this study can be estimated. It should be noted that the porosity of the sintered material will decrease while the bulk density will increase. This means that within the range of compaction pressures used in this study, sintered refractory bricks having porosities between 1·96 and 2·36 g cm^{-3} can be produced from the Nigerian clay used.

4. Conclusion

The effect of compaction pressure on the bulk density and porosity of the Nigerian clay can be described by empirical expressions relating logarithm of relative density to compaction pressure and also relating logarithm of compaction pressure to true porosity before sintering.

The empirical equation describing the effect of compaction pressure on the porosity is similar to the Duckworth equation in the discussion of Ryshkewitch's paper.

The relationship between the bulk density, D and the compaction pressure, P can be represented by

$$D = D_0 \exp\left(1\cdot07 \times 10^{-3} P\right),$$

where D_0 is the true density.

The relationship between the compaction pressure, P and the volume fraction of porosity, p can be represented by

$$P = 1816 \exp\left(-12\cdot94\,p\right).$$

The compaction data for this clay sample has been used to produce refractory bricks by dry pressing prior to sintering.

Acknowledgement

References

Bockstiegel G and Hewing J 1965 *Critical review of the literature on the densification of powders in rigid dies* (Arch. Eisenhuttenwesen) Vol. 36, pp 751–767

Broese Van Groenau A 1981 *J. Powder Technol.* **28** 22

Chesters J H 1974 *Refractories for iron and steel making: Determination of true specific gravity* (The Metals Society) p. 428

Duckworth W 1953 *J. Am. Ceram. Soc.* **36** 68

Dynys F W and Halloran J W 1983 *J. Am. Ceram. Soc.* **66** 655

Onoda G Y and Urban F 1978 *Mechanics of stress and green density variation in ceramic powder compacts: A critical assessment*, in *Proc. of int. symp. on factors in the densification and sintering of oxide and non-oxide ceramics* (eds) S Somiya and S Saito (Tokyo: Tokyo Institute of Technology) pp 93–100

Seelig R P and Wulff J 1946 *Trans. AIME* **166** 492

Shaxby J H and Evans J C 1923 *Trans. Faraday Soc.* **19** 60

Yu Balshin M 1938 *Theory of compacting* (Vestnik Metalloprom) Vol. 18, pp 127–137

CCA leachability of slow dried three major bamboo species of Bangladesh

A K LAHIRY

Office of the Timber Products Specialist, Wood Testing and Research Laboratory, Rural Electrification Board (REB), REB HQ Building, Joarsahara, Khilkhet, Dhaka 1229, Bangladesh

Abstract. Chromated copper arsenate (CCA) leachability tests on full cell pressure impregnated (with 2–3% CCA solution) and slow dried (six months air-drying under cover) bamboo block of three major bamboo species of Bangladesh revealed initial insignificant leaching of CCA within first week and no leaching in next week. Use of low concentration of CCA, release of particle form of CCA due to exposure of bamboo blocks by cutting and presence of water soluble extractives in bamboo might be the causes for initial leaching of CCA.

Keywords. CCA leachability; slow dried bamboo; fixation.

1. Introduction

The bamboo is distributed world wide, especially in tropical areas. It is socioeconomically and environmentally important village and forest crop of Bangladesh (Lahiry 1995a). Besides ecological importance, bamboo is the main raw material for rural housing and also the principal source of withes for making basketry and matting (Banik 1998). From the environmental and economical point of views, the service life of bamboo and bamboo products have to be increased to control the present reserve. The untreated bamboo is perishable. The bamboo reserves can be increased two times (e.g. from 2–3 years to 5–6 years in ground contact) by any means (Lahiry 1995a). The CCA salt treated bamboo has been used in India as exterior claddings and as roofing support for over 33 years (Kumar and Dobriyal 1988). Such long service life has not been reported when used in ground and water (Lahiry 1995a). Effective CCA treatment of bamboo depends on penetratability, retainability, and leachability of CCA. Most of the research studies on preservation of bamboos have been conducted, in India by Purushotham (1963), Singh (1976), Singh and Tewari (1979, 1981), Liese (1980), Tewari (1981), Kumar and Dobriyal (1988), Choudhury (1993), and in Indonesia by Sultoni (1985, 1988). In Bangladesh the researches on preservative treatment of bamboos have been carried out by Salehuddin (1985), Latif et al (1987), Lahiry (1994, 1995a, b, c, 1996, 1997) and Lahiry et al (1996). The CCA treatability and grades of treatment by full cell pressure method at

during pressure treatment have been reported (Lahiry 1994, 1995a, b, 1996, 1997; Lahiry et al 1996). The CCA leachability of these bamboo species and others has not been reported earlier. The leachability of CCA treated green African mountain bamboo (*Arundinaria alpina*) have been reported (Slob et al 1989). The leaching tests carried out by them on CCA impregnated bamboo by Boucherie method, revealed that an average of 15% Cu, 17% Cr and 34% As could be removed by submerging 2 cm bamboo rings in water. A good fixation is possible when sufficiently high (5–10%) concentrations of CCA are used, fixation is mainly the result of formation of Cu–Cr–As complexes in the vascular bundles, in sawdust of bamboo the fixation takes place through the formation of CCA complexes with the bamboo constituents—cellulose and lignin, in this process, fixation of chromium onto cellulose and lignin is the key step (Slob et al 1989).

It is an attempt to study the leachability of CCA-C treated three major bamboo species of Bangladesh after slow air-drying the CCA-C treated bamboo for six months under cover for the environmental safety and effectiveness of CCA treated bamboo in ground and water contact use.

2. Materials and methods

The dry borak bamboo (*Bambusa balcooa* Roxb.), baija bamboo (*B. vulgaris* Schrad. ex Wendle.) and muli bamboo (*Melocanna baccifera* (Roxb.) Kurz.), full cell

facilities, the leachability test was carried out by the method developed by the author with partial modification of AWPA Standard (AWPA Standard E11 1987). About equal weight of treated bamboo blocks ($10 \, g \pm 0.75$ at 14–15% MC, table 1) from internode was taken and dipped in 100 ml of ordinary tap water for leaching of CCA-C. The leachate was analyzed each after 24 h, continuously for 7 days, and at the end of 15th day (table 1). Before each analysis, the block of bamboo was agitated in water for 15 min with the help of magnetic stirrer. Every assay/analysis of leachate was compared with control blank water to find out the actual leaching in same continuous 100 ml of water used from the beginning to end of all tests. Before and after leaching, the level of internodal retention (w/w% = wt. to wt.% and w/v) of bamboo was found out by analysis (table 1). The preleaching retention was determined from different bamboo blocks of original bamboo.

For weight measurement, an analytical optical balance (Mettler H35AR) was used. Moisture content (MC) of bamboos was measured with a calibrated resistance type digital moisture meter (Delmhorst). All the analyses (retention and concentration of leachate) were carried out spectroscopically with an X-ray ASOMA analyzer (model 8620) following standard method (AWPA Standard A9 1990). The chemical balance of individual component of CCA-C was determined from all analyses.

3. Results and discussion

The results of leaching of CCA-C from three bamboo species have been presented in table 1 and discussed as follows.

3.1 *Leaching time and causes*

The present method of leachability tests reveals that leaching of CCA-C only occurs in first week in all three bamboo species and shows no leaching in next week. It was observed that after completion of initial leaching of CCA-C from all types of bamboos, leachates (100 ml tap water with bamboo block) were straw in colour and gelatinous in nature. The same gelatinous nature was also observed in water dipped with untreated bamboo blocks which indicates that the initial leaching only occurs due to presence of nonfixative type of substances e.g. water soluble starches, extractives etc in bamboo, as reported possible in timber by Pizzi *et al* (1986). Use of low concentration of CCA-C and release of particle form of CCA-C due to exposure of bamboo blocks by cutting might be the secondary causes of leaching. Due to slow drying of full cell pressure treated

not be significant if CCA-C treated intact bamboo is used in ground or water, because in such conditions the most leaching areas of bamboo piece will not be exposed compared to the test sample. Several years will be required for the completion of initial leaching.

3.2 *Leaching amount and characteristics*

The leachability test from bamboo block permits leaching of CCA-C components preferably from surfaces rather than inner most or central portion where leaching may not occur at all. Moreover different anatomical structure of different bamboo species responsible to release differential amount of CCA-C e.g. the texture of *M. baccifera* is rather fine. Due to these phenomena of leaching, the different results reflected in leachate and post leaching retention. As such the leaching characteristics of individual component of CCA-C have been analyzed (discussed) separately as follows.

3.2a *From retention*: The chemical balances of CCA-C before and after leaching was found within the limit of CCA type (AWPA Standard P5 1991) in all bamboo species with the marginal insignificant exception in As_2O_5 in *B. balcooa* and *M. baccifera*, where the corresponding balances were found as 27·91% and 29·66% after leaching (30% is minimum normal). But the leachate showed different results.

3.2b *From leachate*: The obtained average chemical balance of leachate in three bamboo species were 64·95% CrO_3, 16·73% CuO and 18·32% As_2O_5 (equivalent to CCA type A) against expected normal CCA-C type of 44·5–50·5% CrO_3, 17–21% CuO and 30–38% As_2O_5 (AWPA Standard P5 1991). This imbalance in leachate is the indication of higher initial leaching of CrO_3 rather than CuO and As_2O_5. Since the leaching of CCA-C was stopped in second week, the necessary key step for fixation of chromium onto cellulose and lignin is not significant here as reported earlier in *A. alpina* by Slob *et al* (1989). Slob *et al* (1989) reported that good fixation is possible when sufficiently high (5–10%) concentration of CCA are used. In the present study, good fixation was obtained with low (2–3%) concentration of CCA, because the treated bamboo was dried slowly for six months.

3.3 *Fixation time*

Slow fixation of CCA treated bamboo was found effective but too long to follow. Accelerated fixation process of CCA treated bamboo by higher temperature, as reported for timbers (Cooper and Ung 1992; Artymko and Cooper

Table 1. Leaching of CCA from three major bamboo species of Bangladesh.

Bamboo species	EMC of CCA-C treated bamboo in July ($\frac{w/w\%}{kg/m^3}$)	Wt of bamboo block (CCA-C treated) at EMC (g)	CCA-C component →	24 h	48 h	72 h	96 h	120 h	144 h	168 h (7 d)	360 h (15 d) (balance %)	Preleaching internodal retention $\frac{w/w\%}{kg/m^3}$ (balance %)	After leaching internodal retention $\frac{w/w\%}{kg/m^3}$ (balance %)
Borack bamboo (*Bambusa balcooa* Roxb.)	15% ± 0·2%	10 ± 0·75	CrO_3 =	0·000%	0·000%	0·030%	0·030%	0·030%	0·030%	0·030%	0·030% (65·22%)	$\frac{1·33}{7·66}$ (50·00%)	$\frac{1·27}{7·32}$ (52...)
			CuO =	0·000%	0·002%	0·002%	0·004%	0·004%	0·005%	0·008%	0·008% (18·80%)	$\frac{0·50}{2·88}$ (18·80%)	$\frac{0·46}{2·65}$ (19...)
			As_2O_5 =	0·000%	0·000%	0·000%	0·000%	0·001%	0·003%	0·008%	0·008% (17·39%)	$\frac{0·83}{4·78}$ (31·20%)	$\frac{0·67}{3·86}$ (27...)
			Total =	0·000%	0·002%	0·032%	0·034%	0·035%	0·038%	0·046%	0·046% (100%)	$\frac{2·66}{15·32}$ (100%)	$\frac{2·40}{13·83}$ (1...)
Baija bamboo (*Bambusa vulgaris* Schrad ex. Wendl.)	15% ± 0·2%	10 ± 0·75	CrO_3 =	0·010%	0·007%	0·021%	0·021%	0·027%	0·028%	0·028%	0·028% (66·67%)	$\frac{1·21}{6·97}$ (50·22%)	$\frac{1·08}{6·22}$ (51...)
			CuO =	0·000%	0·002%	0·004%	0·004%	0·005%	0·005%	0·006%	0·006% (14·29%)	$\frac{0·42}{2·42}$ (17·44%)	$\frac{0·38}{2·19}$ (18...)
			As_2O_5 =	0·000%	0·002%	0·002%	0·002%	0·002%	0·003%	0·008%	0·008% (19·04%)	$\frac{0·78}{4·49}$ (32·34%)	$\frac{0·64}{3·69}$ (30...)
			Total =	0·010%	0·011%	0·027%	0·027%	0·034%	0·036%	0·042%	0·042% (100%)	$\frac{2·41}{13·88}$ (100%)	$\frac{2·10}{12·10}$ (1...)
Muli bamboo [*Melocanna baccifera* (Roxb.) Kerz]	14% ± 0·5%	10 ± 0·75	CrO_3 =	0·000%	0·000%	0·013%	0·015%	0·017%	0·017%	0·017%	0·017% (62·46%)	$\frac{1·09}{6·28}$ (52·91%)	$\frac{0·97}{5·59}$ (51...)
			CuO =	0·000%	0·001%	0·001%	0·004%	0·004%	0·004%	0·005%	0·005% (18·52%)	$\frac{0·35}{2·02}$ (17·02%)	$\frac{0·36}{2·07}$ (19...)
			As_2O_5 =	0·000%	0·001%	0·000%	0·000%	0·000%	0·000%	0·005%	0·005% (18·52%)	$\frac{0·62}{3·57}$ (30·07%)	$\frac{0·56}{3·23}$ (29...)
			Total =	0·000%	0·001%	0·014%	0·019%	0·021%	0·021%	0·027%	0·027% (100%)	$\frac{2·06}{11·87}$ (100%)	$\frac{1·89}{10·89}$ (1...)

Bamboo information

Analyses of leachate and bamboo

Analyses of leachate, dipped in 100 ml of water (continuous) concentration (%)

3.4 *Removal of extractives*

During post treatment weathering or immersion in water, the extractives may be removed enough as reported possible in sundri wood (*Heritiera fomes*) by Lahiry (1994). Leachability of CCA treated bamboo-treated at green vs at kiln-dried vs at weathered and air-dried conditions require to be found out, because presence of water soluble extractives in timber may enhance leaching as reported by Pizzi *et al* (1986).

4. Conclusion

The slow fixation of CCA-C treated three major bamboo species of Bangladesh at low concentration was found significantly effective for ground and water contact use compared to higher concentrations reported earlier for other species. CCA treated bamboo shall have to be dried slowly for proper fixation before outdoor use.

Acknowledgement

References

Artymko J and Cooper P A 1994 *Effects of fixation temperature and humidity on CCA leaching and effectiveness against brown rot fungi and eastern subterranean termites*, M Sc thesis, Toronto University, Toronto

AWPA Standard A9 1990 *Standard method for analysis of treated wood and treating solutions by X-ray spectroscopy* (Book of Standards Amer. Wood Preserver's Association) p. 4

AWPA Standard P5 1991 *Standards for waterborne preservatives* (Book of Standards Amer. Wood Preserver's Association) p. 4

AWPA Standard E11 1987 *Standard method for determining the leachability of wood preservatives* (Book of Standards Amer. Wood Preserver's Association) p. 2

Banik R L 1998 *Bono Biggyan Patrica* **18** 65

Boone R S, Winandy J E and Fuller J J 1994 *Enhanced preservative fixation by redrying CCA treated lumber* (USA: USDA For Ser. For Prod Lab)

Choudhury M Y 1993 *Physical and chemical treatments of bamboo for strength and durability, Chinese Acad. Forestry Int. Trop. Timb. Organiz., Yokohama, Japan*, in *Bamboo and its use, Int. symp. on industrial use of Bamboo, Beijing, China*, pp 155–157

Cooper P A and Ung Y T 1992 *Accelerated fixation of CCA treated poles* (Canada: Toronto University)

Kumar S and Dobriyal P B 1988 *Preservative treatment of bamboo for structural uses*, in *Bamboo Current Research, Proc. Int. Bamboo Workshop, Cochin, India* (KFRI, India) and (IDRC, Canada) pp 199–206

Lahiry A K 1994 *J. Timb. Dev. Assoc. (India)* **40** 20

Lahiry A K 1995a *J. Timb. Dev. Assoc. (India)* **41** 10

Lahiry A K 1995b *Wood preservation science (Bangali)* (Dhaka: Bangla Academy) 1 ed. vol. 1, p. 184

Lahiry A K 1995c *Wood preservation science (Bangali)* (Dhaka: Bangla Academy) 1 ed. vol. 2, p. 211

Lahiry A K 1996 *CCA treatability of 100 timbers of Bangladesh*; Internat. Res. Group on Wood Preserv. Document No. IRG/WP/40069, p. 17

Lahiry A K 1997 *J. Sci. & Ind. Res. (India)* **56** 39

Lahiry A K, Begum S, Ilias G N M, Matin Sheikh M A, Fakir M A B and Hossain M I 1996 *An effective preservative treatment of borak bamboo (Bambusa balcooa Roxb.)* Internat. Res. Group on Wood Preserv. Document No. IRG/WP/40070 p. 17

Latif M A, Dasgupta S R, De B C and Zaman Y U 1987 *Preservative treatment of bamboo and low cost housing, Bulletin 3 Wood Preservation Series* (Bangladesh: BFRI) p. 5

Liese W 1980 *Preservation bamboos*, in *Bamboo Research in Asia* (Canada: IDRC) pp. 165–172

Purushotham A 1963 *Timber Dryers' Preser. Assoc. (India)* **9** pp. 1–2

Pizzi A, Contradie W E and Bariska M 1986 *Polyflavonoid tannins from a cause of soft rot failure to the 'missing link' between lignin and micro-distribution theories*; Int. Res. Group on Wood Preserv. Document No. IRG Doc. No. IRG/WP/3359

Singh B 1976 *Studies on the diffusion of water soluble wood preserving chemicals in bamboo*, Ph D Thesis, Punjabi University, Patiala, India

Singh B and Tewari M C 1979 *J. Indian Acad. Wood Sci.* **10** 68

Singh B and Tewari M C 1981 *J. Timb. Dev. Assoc. (India)* **27** 68

Sultoni Achmad 1985 *Traditional preservation of bamboo in Java*, in *Recent Research on Bamboos* (Canada: IDRC) pp. 349–357

Sultoni Achmad 1988 *A simple and cheap method of bamboo preservation*, in *Bamboos Current Research, Proc. Int. Bamboo Workshop, Cochin (India)* (India: KFRI) and (Canada: IDRC) pp. 209–211

Salehuddin A B M 1985 *REB manual for preservative treatment of bamboo culms—improved sap displacement method* (Dhaka: REB) p. 4

Slob J W, Nangawe P F, de Leer E and Donker J 1989 *CCA impregnation of bamboo-leaching and fixation characteristics* (Netherlands: Delft University of Technology, Water Chemistry Group) pp. 321–335

Tewari M C 1981 *Recent studies on the protection of bamboo against deterioration*, in *Proc. Group 5 03 XVII TUFRO World Cong. Japan*

Bulletin of Materials Science

Notes on the preparation of papers

Authors may communicate their research work as papers and rapid communications to the Bulletin of Materials Science. They may also submit topical reviews. The papers may be sent to the Editor or to one of the International Advisory Board members.

All communications should be submitted in triplicate (original + two copies).

Authors are encouraged to send electronic files prepared using plain latex or MS Word (RTF), of final accepted version of their articles. This will help hasten the process of typesetting. Line drawings also may be submitted in electronic format in some standard graphic format—TIFF, .for example, and saved in EPS format. However, a hard copy with figures must also be submitted along with floppy (3.5") of electronic files.

Submission of a script will be held to imply that it has not been previously published and is not under consideration for publication elsewhere; and further that, if accepted, it will not be published elsewhere.

Typescript

Papers must be typed double spaced with ample margin on all sides on one side of white bond paper of quarto size (280 × 215 mm). This also applies to the abstract, tables, figure captions and the list of references which are to be typed on separate sheets.

Title page

1. The title of the paper must be brief but informative. Serial titles are to be avoided.
2. The names with initials of authors and the name and address of the institution where the work was done must be given.
3. An abbreviated running title of not more than 50 letters and spaces must also be given.
4. Authors are requested to provide e-mail and fax addresses while submitting the script.

Abstract

Papers must have a brief abstract of the significant results reported in the paper.

Keywords

Between 3 and 6 keywords must be provided for indexing and information retrieval.

The Text

The paper must be divided into sections starting preferably

Tables

All tables must be numbered consecutively in arabic numerals in the order of occurrence in the text; they should be self-contained and have a descriptive title.

Figures

All figures including photographs should be numbered consecutively in arabic numerals in the order of appearance in the text. Line drawings must be in Indian ink on good quality tracing paper or Bristol board of the same size as the text paper. Lines should be sufficiently thick (axes about 0.3 mm, curves about 0.6 mm).

Units

Units and associated symbols must invariably follow SI practice.

References

References should be cited in the text by author and year, not by number. If there are more than two authors, reference should be to the first author followed by et al in the text. References at the end of the paper should be listed alphabetically by author's names, followed by initials, year of publication, name of the journal (abbreviated according to the World List of Scientific Periodicals, Butterworths, London), volume number, and number of the first page. Reference to books should include: name(s) of author(s), initials, year of publication, title of the book, edition if not the first, initials and name(s) of editor(s) if any, preceded by ed(s), place of publication, publisher and chapter or pages referred to. References to thesis must include the year, the title of the thesis, the degree for which submitted and the University.

Footnotes

Footnotes must be avoided if possible but when necessary should be numbered consecutively, and typed on a separate sheet.

Proofs

Authors are requested to prepare the manuscript carefully before submitting it for publication to minimize corrections and alterations in the proof which increase publication costs. Page-proofs sent to author together with the reprint order form must be returned to the editorial office within two days of their receipt by SPEED POST/COURIER.

Editorial Office